Copyright

by

Xiaohui Lin

2013

The Dissertation Committee for Xiaohui Lin Certifies that this is the approved version of the following dissertation:

Novel Printing Technologies for Nanophotonic and Nanoelectronic Devices

Committee:

Ray T. Chen, Supervisor

Ananth Dodabalapur

S V Sreenivasan

Zhigang Pan

Nanshu Lu

Harish Subbaraman

Novel Printing Technologies for Nanophotonic and Nanoelectronic Devices

by

Xiaohui Lin, B.E.; B.E.; Ph.D.

Dissertation

Presented to the Faculty of the Graduate School of

The University of Texas at Austin

in Partial Fulfillment

of the Requirements

for the Degree of

Doctor of Philosophy

The University of Texas at Austin

August 2013

Dedication

To my family

Acknowledgements

I would like to express my sincere gratitude to my supervisor Dr. Ray T. Chen for his guidance and support of my Ph.D. studies. It is with his precious and insightful guidance that this work was completed. Besides, I would like to thank Dr. Swapnajit Chakravarty, Dr. Amir Hosseini, Dr. Harish Subbaraman and Dr. Alan X. Wang from Omega Optics Inc., for their helpful suggestions and valuable opinions.

I would also like to thank Dr. Ananth Dodabalapur, Dr. S V Sreenivasan, Dr. Zhigang Pan and Dr. Nanshu Lu for their valuable time in serving on my dissertation committee and giving valuable suggestions.

I would like to thank Dr. Tao Ling and Dr. L. Jay Guo at University of Michigan for their excellent work performed on the imprinting. It is a valuable experience to collaborate with them.

I would also like to thank Mrs. Jackie L. Srnensky and other staff members in the Microelectronics Research Center at The University of Texas at Austin for providing me with such an excellent research and development environment to conduct my research.

I would like to express my thanks to all my friends in the optical interconnect group: Kwangsub Byun, John Covey, Xinyuan Dou, Andreas Hsieh, David Kwong, Wei-Cheng Lai, Beom-Suk Lee, Che-Yun Lin, Daniel T Pham, Lei Wang, Xiaochuan Xu, Xingyu Zhang, Yang Zhang, Liang Zhu and Yi Zou for their help and friendship, making my Ph.D. life more meaningful and colorful. Wish all of you a bright future!

Finally, I will thank my family especially my wife Yi Wang. She is always the most unselfish love to support and encourage me all these years. And my son Charley W. Lin, you are always our proud.

Novel Printing Technologies for
Nanophotonic and Nanoelectronic Devices

Xiaohui Lin, Ph.D.
The University of Texas at Austin, 2013

Supervisor: Ray T. Chen

As optical interconnects make their paces to replace traditional electrical interconnects, implementing low cost optical components and hybrid optic-electronic systems are of great interest. In the research work described in this dissertation, we are making our efforts to develop several practical optical components using novel printing technologies including imprinting, ink-jet printing and a combination of both. Imprinting process using low cost electroplating mold is investigated and applied to the waveguide molding process, and it greatly reduces the surface roughness and thus the optical propagation loss. The imprinting process can be applied to photonic components from multi-mode waveguides with 50μm critical dimension down to photonic crystal structures with 500nm hole diameter. Compared to traditional lithography process, imprinting process is featured by its great repeatability and high yield to define patterns on existing layers. Furthermore we still need an approach to deposit layers and that is the reason we integrate the ink-jet printing technology, another low-cost, low material consumption, environmental friendly process. Ink-jet printing process is capable of depositing a wide range of materials, including conductive layer, dielectric layer or other functional layers with defined patterns. Together with molding technology, we demonstrate three applications: proximity coupler, thermo-optic (TO) switch and electro-optic (EO)

polymer modulator. The proximity coupler uses imprinted 50μm waveguide with embedded mirrors and ink-jet printed micro-lenses to improve the board-to-board optical interconnects quality. The TO switch and EO modulator both utilize imprinting technology to define a core pattern in the cladding layer. Ink-jet printing is used to deposit the core layer for TO switch and the electrode layers for EO modulator. The fabricated TO switch operates at 1 kHz with less than 0.5ms switching time and the EO modulator shows V_{π}•L=5.68V•cm. To the best of our knowledge, these are the first demonstrations of functional optical switches and modulators using printing method. To further enable the high rate fabrication of ink-jet printed photonic and electronic devices with multiple layers on flexible substrate, we develop a roll-to-roll ink-jet printing system, from hardware integration to software implementation. Machine vision aided real time automatic registration is achieved when printing multiple layers.

Table of Contents

List of Tables x

List of Figures xi

Chapter 1: Introduction 1

1.1 Overview of nanophotonic and nanoelectronic devices. 1

1.2 Introduction of the molding method 3

1.3 Introduction of printed electronics and ink-jet printing method 5

1.4 roll-to-roll compatible imprinting and ink-jet printing 10

1.5 Dissertation organization 12

Chapter 2: Polymer Based Photonic Device with Imprinting Method 15

2.1 Comparison of mold fabrication method 15

2.2 Photonic waveguide fabricated by imprinting mold 17

2.3 Quality evaluation 19

2.4 Electroforming for nanoscale photonic device structure 21

2.5 Chapter conclusion...24

Chapter 3: Intra- and Inter- Board Optical Interconnects 25

3.1 Concept of board to board optical interconnect 25

3.2 Fabrication of polymer based waveguide structure 27

3.3 Fabrication of ink-jet printed micro-lenses 29

3.4 Optical evaluation of board to board interconnects 31

3.5 Chapter conclusion...34

Chapter 4: Printable Total Internal Reflection (TIR) Based Thermo-Optic (TO) Switch 36

4.1 Concept of optical switch...36

4.2 Fabrication process 39

4.3 Device characterization..44

4.4 Chapter conclusion...45

Chapter 5: Printable Electro-Optic (EO) Polymer Modulator 47
5.1 Designing printable electro-optic polymer based M-Z modulator 47
5.2 Fabrication process 50
5.3 Device characterization...54
5.4 Chapter conclusion..59
Chapter 6: Roll-To-Roll (R2R) Printing System Integration................................60
6.1 Introduction, opportunity and innovation for R2R printing....................60
6.2 System components for single-layer and multi-layer printing................61
6.3 System integration 72
6.4 Module testing and comprehensive testing..81
6.5 Towards building dual-stage ink-jet printing system.............................88
6.6 Chapter conclusion..90
Chapter 7: Summary 91
Appendix A: Xenon Fast Curing System..93
Appendix B: LabVIEW Code for Printer Control 98
Appendix C: Publication List...99
Bibliography 102
Vita 113

List of Tables

Table 1-1 Feature, Advantages and Benefits (FAB) table for ink-jet printing technology 8

Table 5-1 modulation depth at different frequencies 57

Table 6-1 specifications for KM1024MH printhead from Konica Minolta (source: http://www.industrialij.com/pages/KM1024.html) 68

Table 6-2 curing results under various conditions 70

Table 6-3 limiting factors for registration error 87

List of Figures

Figure 1-1 bandwidth by distance applications requirements for short and long distance communication links[4] 2

Figure 1-2 (a) cross section for channel waveguide, (b) cross section for rib waveguide 3

Figure 1-3 (a) ion etching method for forming a ridge waveguide; (b) photolithography process for forming channel waveguide & rib waveguide; (c) molding method for forming a ridge waveguide. 4

Figure 1-4 Dimatix Materials Printer (DMP-2800) and the cartridge. The working principle basically includes four phases to ink-jet a single droplet of material (source: http://www.fujifilmusa.com)..................................9

Figure 1-5 printed PAA and all the layers contained in the Carbon nanotube thin-film transistors [51] 10

Figure 1-6 (a) a 4 in. wide x 12 in. long (~0.03 square meters) 700 nm period epoxysilicone pattern on flexible PET substrate by R2RNIL process [52] (b) SEM image of the patterned grating structure[52], (c) SEM image of a 70nm line width, 100nm pitch grating structure [23] 11

Figure 1-7 schematic of high rate, large area roll-to-roll (R2R) manufacturing of integrated photonic devices using a combination of nanoimprint lithography (NIL) and ink-jet printing processes on a flexible substrate. NIL forms sub-100nm patterns on polymer film. Ink-Jet enables precise placement of materials to form full optoelectronic device. 12

Figure 2-1 (a) quartz mold fabrication process[58], which represents a material removal method. (b) Electroplating method for fabricating Ni metal mold. (c) E-beam evaporation method fabricating Silicon Dioxide mold 17

Figure 2-2 (a) comparison of different 5μm waveguide fabrication methods. (left): ion etched waveguide. (middle): molded waveguide with electroplated Ni mold. (right): molded waveguide with evaporated SiO_2 mold; (b) surface roughness evaluation with AFM scanning and SEM inspection, for imprinted sample and ion-etched sample..20

Figure 2-3 nanoscale pillar array with 500nm in diameter, with a pillar zoomed in. (b) cross sectional view of the electroplated Ni pillar array 22

Figure 2-4 photonic crystal pattern and electroplated Ni mold. (a) overview of the device template; (b) zoomed in hexagonal array of photonic crystal structure template (rotate by 90°), scale bar: 200nm; (c) light input/output coupling area, scale bar: 1μm......................................23

Figure 2-5 photonic crystal waveguide: (a) electroplated Ni mold. (b) imprinted polymer profile using Obducat NIL machine 23

Figure 3-1 inter- and intra-board optical interconnects with polymer waveguides and 45° couplers with ink-jet printed micro-lenses. 26

Figure 3-2 fabrication process for molded channel waveguide with 45° embedded mirror coupler. The scale bar represents 50μm length. 28

Figure 3-3 (a) top view of embedded mirror before printing micro-lens (b) top view of embedded mirror after printing micro-lens with d=70μm. (c) the lens profile taken by contact angle goniometer.......................................30

Figure 3-4 board-to-board experimental setup showing (a) one waveguide with two 45° mirrors (b) two waveguides with four 45° mirrors. Visible spots show the output after 2 mirrors and 4 mirrors. Optical loss evaluation31

Figure 3-5 (a) total insertion loss with the separation between two boards, when 2 mirrors, 2 mirrors w/lens and 4 mirrors are included; (b) transmission loss in free space when using 45° coupler with/without lens and proximity coupler with lens from [67]..33

Figure 3-6 (a) Q factors with different data rate, at different separations. Two mirror couplers are included in optical path. (b) Bit Error Rate (BER) distribution with data rate at different separations with/without ink-jet printed lens...34

Figure 3-7 eye diagrams at selected data rate (2Gbps, 6Gbps and 10Gbps): (a) 1 mm separation with 2 mirrors; (b) 1 mm separation with 2 mirrors and 1 lens; (c) 2 mm separation with 2 mirrors and 1 lens. 35

Figure 4-1 (a) schematic showing the top view of the 2×2 thermo-optic switch layout. A horn structure, with a half branch angle of 4o is used. Gold heating electrode is 8 μm wide over the center region of the horn. (b) The cross-section view and the simulated mode profile at the input side of the 2×2 TO switch. The mode is well confined in the waveguide. Core layer is composed of 1.8 μm thick slab and 0.5 μm (height) × 5 μm (width) strip. (c) Simulation results of the power outputs from the bar (blue) and the cross (green) ports when the junction is in switching condition.......38

Figure 4-2 process flow for fabricating a 2x2 thermo-optic polymer switch using imprinting and ink-jet printing method...40

Figure 4-3 (a) silicon master mold fabrication process (b) soft mold replication from master mold..41
Figure 4-4 SEM images of (a) silicon mold (b) SSQ soft mold (c) imprinted UV 15LV at the junction area of the TO switch. The inset in (a) shows the cross-section views of the silicon mold, with 500nm step height. The upper left insets in (b) and (c) show the zoom-in views of the merging points of two waveguides. The lower right insets in (b) and (c) shows the tilted view of mold and imprinted trench in the 5 μm wide input/output regions..42
Figure 4-5 SEM cross-section view of printed layers in the device, (a) with ink-jet printed UV15LV as top cladding (b) with coated UFC-170A as top cladding...43
Figure 4-6 (a) testing setup: auto-aligner and probe station with TO switch sample mounted (b) microscopic picture showing the top view of a fabricated 2x2 thermo-optic polymer switch. (c) normalized optical output power versus electrical power consumption from both bar port and cross port. 45
Figure 4-7 optical response with square wave function applied across the heating electrode, at selected frequencies of (a) 100Hz, (b) 300Hz, (c) 500Hz, and (d) 1 kHz. The device can operate at 1 kHz with decent performance. 45
Figure 5-1 (a) schematic top view showing the modulator structure, (b) schematic cross section showing the different materials comprising the EO polymer modulator...49

Figure 5-2 main process flow for fabricating an EO polymer modulator using imprinting and ink-jet printing method. (a) silicon and SSQ mold, (b) bottom electrode deposition, (c) bottom cladding layer deposition, (d) imprinting, (e) core layer and top cladding layer deposition, (f) top electrode deposition 50

Figure 5-3 (a) ink-jet printed silver layer as bottom electrode, on silicon substrate (b) ink-jet printed silver layer as bottom electrode, on Kapton film 51

Figure 5-4 (a) EO polymer modulator with ink-jet printed electrode. (b) zoom-in view of the silver electrode showing smooth surface 52

Figure 5-5 schematic illustration of thermally assisted electric field poling process53

Figure 5-6 (a) poling setup (b) poling profile showing leakage current with poling time. The peak is reached when the temperature reaches 140 ^{o}C.....54

Figure 5-7 cross-section view of printed EO modulator......................................55

Figure 5-8 (a) EO modulator sample testing on auto-aligner (b) other equipment for signal generation and collection..56

Figure 5-9 (a-b) 100 kHz triangle wave input and corresponding modulator output signal; (c-d) 15 MHz sinusoidal wave input and corresponding modulator output..57

Figure 5-10 modulation depth at different bias voltages at 10MHz 58

Figure 6-1 schematic drawing of the main components in the roll-to-roll printing system with active alignment function. The main modules are 1) substrate moving module; 2) pattern detection module; 3) material ink-jet printing module; 4) fast curing module and 5) system controlling module. Modules (2) (3) and (4) form a standalone single stage for aligned-printing and can be configured in series to realized multi-stage printing. 62
Figure 6-2 (a) schematic of Arpeco web tracker tool (from product's manual); (b) TR1 wheel encoder 64
Figure 6-3 field of view (FOV) of the line-scan camera showing 2048 by 200 pixels; calibration pattern of 6mm is used. 66
Figure 6-4 alignment mark detection using line-scan camera and Print/Go mark detection using photoelectric sensor. 67
Figure 6-5 Sinteron 2000-S flash lamp sintering system (a) LH-910 lamp house with spiral lamp; (b) electronics rack (source: http://www.xenoncorp.com) 70
Figure 6-6 edge detection for Y direction alignment 73
Figure 6-7 mapping offset value in pixel to corresponding image id 75
Figure 6-8 the connection part fixes the relative position of camera and printhead76
Figure 6-9 alignment strategy in X direction indicating the positioning requirement of the printhead, camera and Print/Go sensor 78
Figure 6-10 multi-layer printing using a single stage. A dummy run is needed to ensure the pattern's polarity. 79
Figure 6-11 pseudo code and flow chart for the controlling software 81

Figure 6-12 (a) screenshot of the software showing position of alignment mark; (2) a sample of 20 consecutive alignment marks position indicating the web sideway wander of around 1.5-2mm for this pass 82

Figure 6-13 continuous pattern are printed and cured in-line. 83

Figure 6-14 (a) test pattern for aligned printing; (b) printed results showing registration of two layers with off-alignment less than 100μm in both X and Y directions. 84

Figure 6-15 continuous printing showing satisfying online registration of 2nd layer patterns with ΔX<100μm and ΔY<200μm for all copies. The scale bar is 10mm (also shown in the central picture). 85

Figure 6-16 a complete stage for one layer ink-jet printing makes a building block for multi-stage system 88

Figure 6-17 (a) schematic of two-stage ink-jet printing process; (b) actual setup showing dual printing stages (without curing station) 89

Figure A-1 a normalized melting curve for gold as a function of nanoparticle diameter. The bulk melting temperature and melting temperature of the particle are denoted TMB and TM respectively. Experimental melting curves for near spherical metal nanoparticles exhibit a similarly shaped curve. 94

Figure A-2 spectra of Xenon flash lamp and image below shows how high energy can be delivered using short pulses 96

Figure B-1 block diagram (a) and front panel (b) of the LabVIEW VI developed for controlling the ink-jet printing system 98

Chapter 1: Introduction

1.1 OVERVIEW OF NANOPHOTONIC AND NANOELECTRONIC DEVICES.

Multimedia information is penetrating into almost every aspect of our daily life. From high speed internet to 3G, 4G LTE network, from internet TV to cloud storage, people are raising higher demands for audio/video streaming than traditional radio or broadcasting services, and it raises increasingly stringent requirements for latency and power consumption per bit [1]. Traditional copper interconnect technology is facing great challenges when high bandwidth is required. Alternatively, optical interconnects have been drawing researchers' attention due to its intrinsic advantages such as immunity to electromagnetic interference, high speed operation, low power consumption [2], etc. Chen etc. [3] have compared the optical interconnects in detail with traditional copper interconnects in many aspects including delay uncertainty, latency, power, and bandwidth density etc. However, currently, it is still impossible to use optical interconnects to completely replace traditional copper interconnects. Currently, as illustrated in Figure 1-1[4], we are still in transition edge of the copper interconnect. It is reasonable to integrate the optical channels into the current electrical components to achieve high speed data transmission in the "bottle neck" of an application. To realize this, widespread deployment of photonic devices such as wavelength-division multiplexing (WDM), optical switch, splitter, modulator, coupler, etc. to maximize the system's capacity is required, while shrinking the total cost.

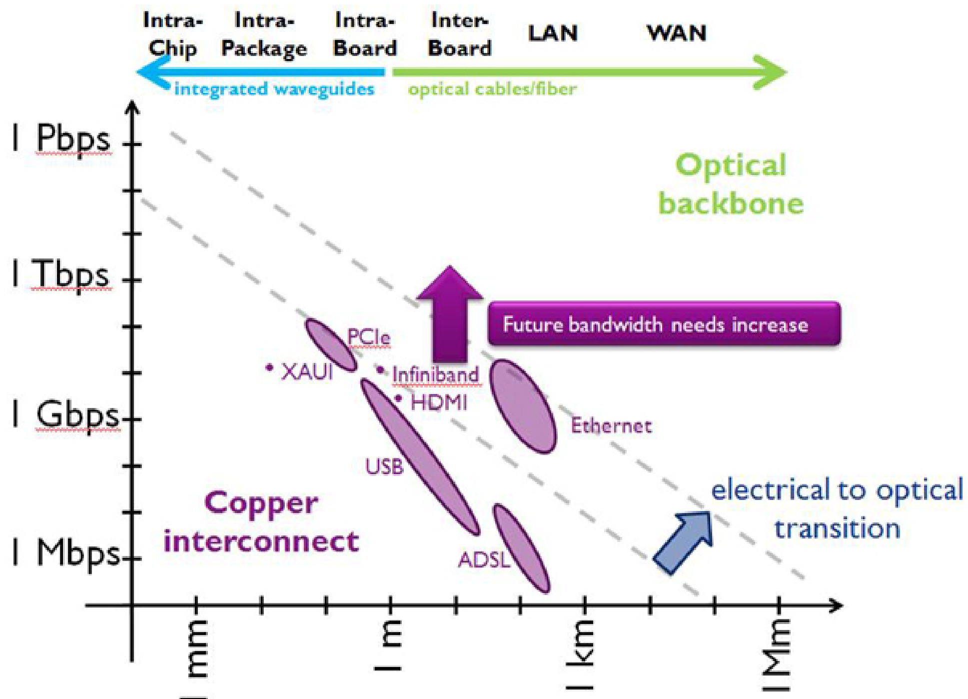

Figure 1-1 bandwidth by distance applications requirements for short and long distance communication links[4]

Polymer photonics is an important branch in modern integrated optics. For example, the EO polymer is featured by its significant advantages over other EO materials, such as lithium niobate, in terms of high electro-optic efficiency[5], ultra-wide bandwidth[6], and small device size[7]. Besides, the processability of polymer is an advantage which provides a good platform for integrating various active and passive devices, including polymer DBF lasers [8], optical bus waveguides [9], optical switches [10, 11], optical modulators [12-14], etc. For most polymer photonic components, availability of a good waveguide is essential in building up a functional device. A typical polymer waveguide consists of a core layer with higher refractive index than its surrounding cladding layers. The waveguide, depending on its structure and dimensions, can accommodate multiple optical modes (multimode waveguide), or only support the

fundamental mode (single mode waveguide). Figure 1-2 shows the cross section of (a) a basic ridge/channel waveguide and (b) a rib waveguide.

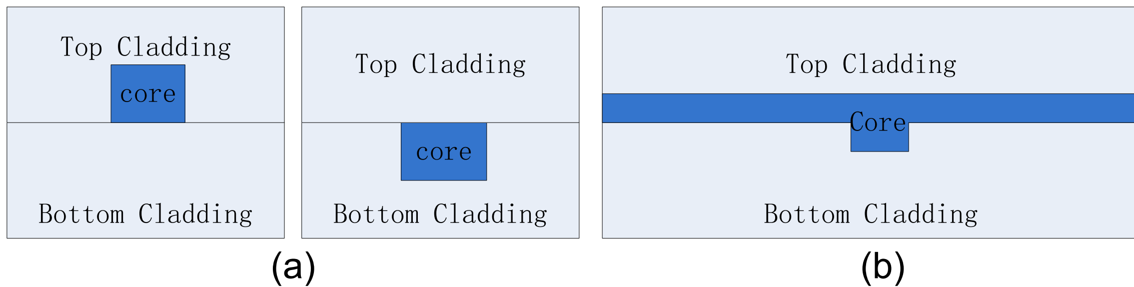

Figure 1-2 (a) cross section for channel waveguide, (b) cross section for rib waveguide

1.2 INTRODUCTION OF THE MOLDING METHOD

The most common method for polymer optical device fabrication includes using high energy reactive ion-beam (RIE) to define the pattern into a resist, and further transferring the pattern to the optical polymer via etching[15], as illustrated in Figure 1-3(a). This method is straightforward, but not a cost-effective way due to complicated fabrication process and low throughput. Another method is to directly pattern a low loss UV-curable polymer using lithography [16]. However, this method is limited due to poor dimension and profile control resulting from the effects of wave diffraction, interface and substrate scattering [17]. Therefore, recently, there has been escalating progress in using various lithography-free fabrication methods for defining nano-scale structures with high precision on a wide variety of materials, such as micro-contact printing (or soft lithography[18]), nano-imprint lithography (NIL)[19], laser direct wiring[20], scanning-probe-based techniques (e.g., atomic force microscope lithography[21]), and dip-pen lithography[22].

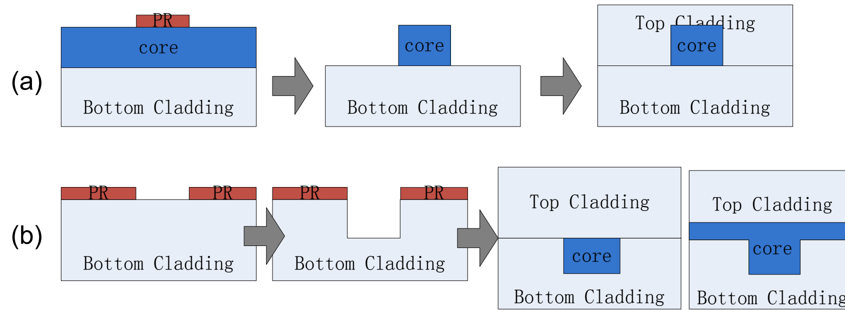

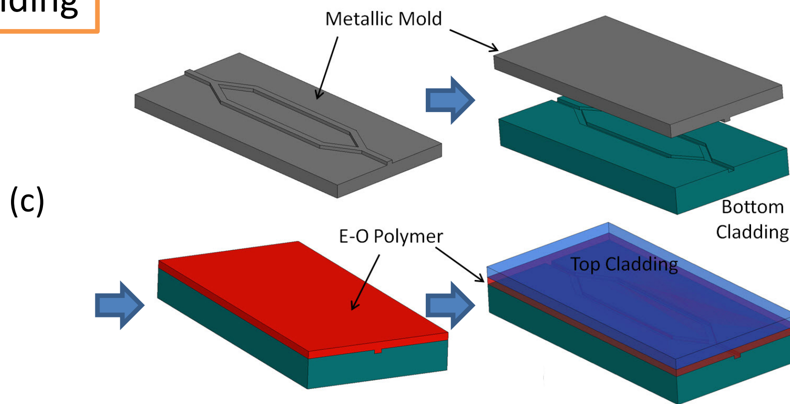

Figure 1-3 (a) ion etching method for forming a ridge waveguide; (b) photolithography process for forming channel waveguide & rib waveguide; (c) molding method for forming a ridge waveguide.

Among these, molding/imprinting method is a preferred candidate that can effectively overcome the shortcomings of the RIE method, and can potentially provide roll-to-roll (R2R) patterning capabilities at both the micro- and nano-scales, thus providing a viable solution for the high-rate development of low cost polymer photonic devices [23]. Imprinting method is a process that creates patterns by mechanically deforming an imprint resist as shown in Figure 1-3 (c). The imprint resist is typically a monomer or a polymer formulation that can be cured by heat or UV light during imprinting. To ensure successful release, a releasing agent is employed to modify the

surface properties of the mold/substrate. Extensive research has been conducted on using various kinds of molds to pattern basic optical components such as micro-lens array [24, 25], polymer gratings [23, 26, 27], optical waveguides with different dimensions [28-32], micro-ring resonators [33, 34] and other complete functional devices using imprinting method [17, 35-37].

1.3 INTRODUCTION OF PRINTED ELECTRONICS AND INK-JET PRINTING METHOD

As mentioned above, molding method provides a feasible way to define patterns with great repeatability. To complete devices with multi-layer stacking structure, a layer deposition technique is still required and this leads to another important technique: material ink-jet printing.

(1) Printed electronics

Since 2001, printed electronics has seen a significant growth in the market, from less than $500 million in 2001 to ~ $3.5 billion in 2010 [Source: IDTechEx], owing much to the low cost fabrication alternatives available compared to conventional semiconductor processing techniques. Printed electronic circuits are being widely considered for both military and civilian applications. The main applications and estimated market value by 2018 are 1) logic/memory ($7 billion), 2) OLED display ($48 billion), 3) OLED lighting ($7 billion), 4) battery ($2 billion), 5) photovoltaic ($8 billion), 6) sensors ($3 billion), 7) printed and thin-film electronics ($55 billion), 8) RFID ($8 billion)and 9) printed and thin film transistor circuits ($8 billion) [Source: IDTechEx]. The values provided in the parentheses show the estimated market value by 2018.

Conventional electronic systems are bulky, heavy, and traditionally the more the technologies needed to perform complex tasks, such as data terminal, batteries, displays, GPS, the heavier they become. It is desirable to achieve such varied functionalities in an

extremely light weight alternative form, for example, on a light weight flexible substrate that can be integrated along with any platform, such as clothing, aircraft surface, and other structures). Such a light weight and conformal circuits will tremendously benefit applications where light weight electronics are required.

Through functional integration of inorganic, organic and bio-inspired materials on a single light weight flexible substrate, several unique flexible electronic components such as RFIDs [38, 39], Sensors[40], displays[41, 42], Solar Cells[43, 44], Antennae[45], Switches[46], etc., can all be fabricated on a single low-cost, light weight flexible substrate, using an affordable high-rate roll-to-roll manufacturing process.

(2) Ink-jet printing method

Ink-jet printing represents a non-contact printing technology in which droplets of a various selection of materials can be jetted at the desired position continuously, thus creating an image on a substrate.

Compared to conventional printing techniques such as Offset Lithography, Gravure Printing, Flexography and Screen printing[47], Ink-Jet printing provides an alternative simpler way to deposit material only on the desired region with simplified process. It is an ideal solution for low cost, high speed printed electronics due to low material consumption; low equipment and setup costs; and possibility for mass customization[48]. It is also a non-contact printing technique which does not require any template preparation [49, 50]. Therefore, rapid printing is possible because once the circuit is designed, it can be printed immediately without time lag involved in producing templates which are mandatory in other printing processes, thus also reducing the number of steps and extra costs involved in the process. The digital non-contact ink-jet printing technique also allows integration of a multitude of materials to form a full functional light

weight, conformal system, since all the materials are printed only at the intended locations without the use of any templates or other contact printing procedures. That will be extremely difficult to achieve using other conventional methods. Due to their small footprint and relatively inexpensive machine and setup costs (less than one million dollars compared to several million dollars for conventional printing types), ink-jet printers are easy to integrate with existing production lines. The uniformity of the thickness of films deposited is much better with ink-jet printing than other printing techniques because surface topography is not a factor in influencing film thickness. Another advantage of ink-jet printing from the point of view of circuit performance is the ability to vary the film thickness for different parts of the circuit. This leads to an additional degree of freedom because the thickness of the film is not a design variable in conventional screen printing circuits. Since ink-jet printing can be completely computer controlled, a higher degree of automation is possible with potential savings in cost and improved throughput compared to conventional technologies. The advantages and benefits can be summarized in Table 1-1.

Table 1-1 Feature, Advantages and Benefits (FAB) table for ink-jet printing technology

Feature	Advantages	Benefits
Non-contact printing	Avoids material contact	• Helps prevent contamination • Eliminates risk of defect on a template • Drop on demand printing
Digital image printing	No template required	• Saves time and effort • Tremendous cost savings
Substrate independent process	Manufacturing on any kind of rigid, flexible or curved surface	Integration with any platform is possible such as aircraft wing, car windshield, helmet etc.
Smaller machines	Easy to integrate with existing production lines	• Small footprint • Low equipment and setup costs
Customization	Printing of a variety of patterns is possible	• No additional templates are required • Cost savings • Saves time
Low material wastage	Reduces material cost	Overall cost savings
Additive manufacturing process	No etching process involved	Can be performed outside clean room environment
Film layer uniformity	Can achieve better printed layers	Good and uniform device performance

The printer employed in this research is a Fujifilm Dimatix Materials Printer (DMP-2800) shown in Figure 1-4. It utilizes a piezoelectric cartridge to jet material onto a desired area on the substrate. The working principle of the material printer is also shown in Figure 1-4. The material choice is wide as long as its viscosity is between 10-12 cPs (1.0×10^{-2} - 1.2×10^{-2} Pa·s), and surface tension is between 28 and 33 dynes/cm (0.028 - 0.033 N/m) at operating temperature. With the aid of a fiducial camera, the printing region can be defined within a positional error of 25 µm.

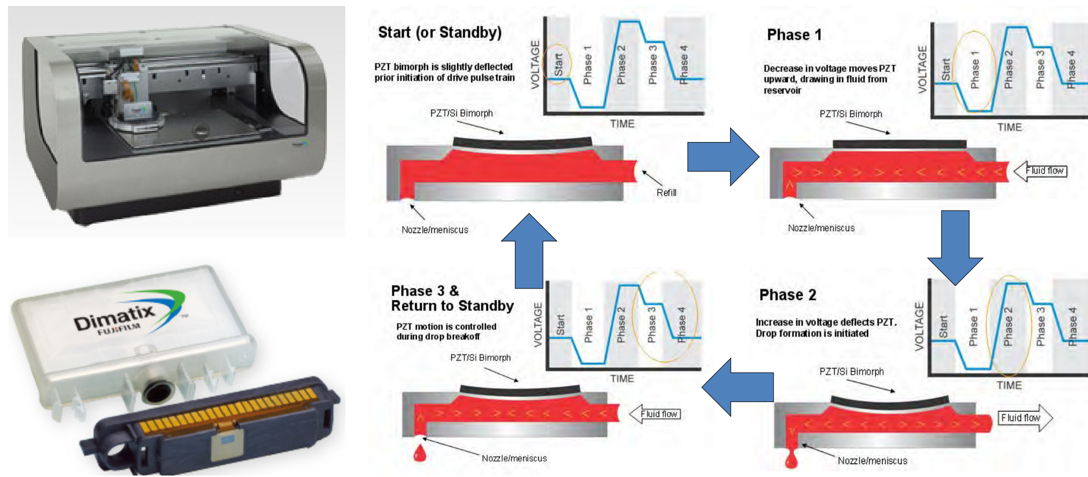

Figure 1-4 Dimatix Materials Printer (DMP-2800) and the cartridge. The working principle basically includes four phases to ink-jet a single droplet of material (source: http://www.fujifilmusa.com)

Some preliminary research has been performed to characterize and optimize several material inks to be compatible with a Dimatix DMP 2800 ink-jet printer. Using the characterized materials, we printed and tested thin film based field-effect transistors (FETs) utilizing carbon nanotubes (CNTs) as active material. A Phased Array Antenna (PAA) system was developed using the ink-jet printer by combining microstrip transmission lines and antenna elements. Beam steering of 3GHz signal from 0 to 13.6^{o}s was demonstrated. The PAA and FET switch printing process is demonstrated in Figure 1-5[51]. The carbon nanotube thin-film transistors (CNT-FETs) contain gates contacts, dielectric, source/drain contact and active layers. It can perform as a switch to change the signal path, thus changing the phase of the RF signal.

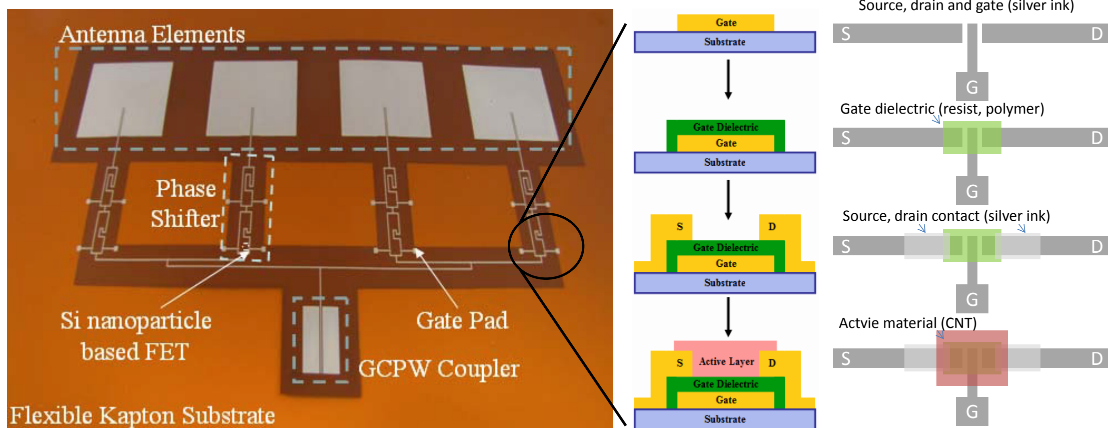

Figure 1-5 printed PAA and all the layers contained in the Carbon nanotube thin-film transistors [51]

1.4 ROLL-TO-ROLL COMPATIBLE IMPRINTING AND INK-JET PRINTING

A significant advantage for both imprinting and ink-jet printing technology is the compatibility of extending to roll-to-roll fabrication.

Dr. L. Jay Guo's group at the University of Michigan – Ann Arbor, has developed a high-speed roll-to-roll nanoimprint lithography (R2RNIL) process that is capable of producing patterns continuously, with roll speeds up to 1meter/min[52]. Using this R2RNIL technique, large area printing of 4inch wide × 12inch long (~0.03 m^2) 700nm period grating pattern on a flexible polyethylene teraphthalate (PET) substrate using a UV curable low viscosity liquid epoxysilicone as the imprint resist material, as shown in Figure 1-6 (a), has been demonstrated[52]. An SEM image of the patterned grating structure is shown in Figure 1-6 (b). The process has also been optimized to form 100nm pitch, 70nm line width gratings, as shown in Figure 1-6 (c) [23], thus demonstrating the capability of R2R process for developing sub 100nm features. Such structures can be used to form efficient grating couplers for waveguides on flexible substrates.

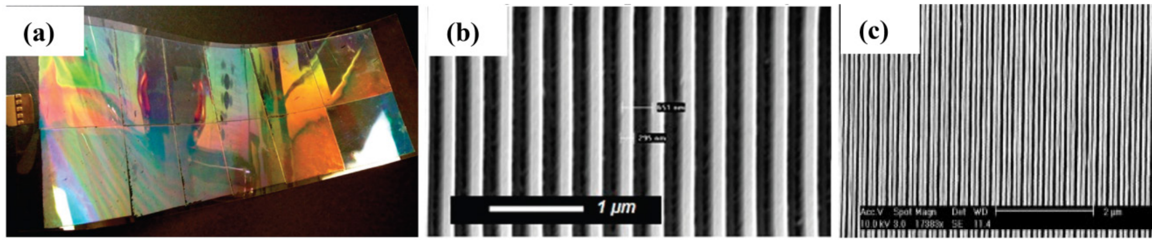

Figure 1-6 (a) a 4 in. wide x 12 in. long (~0.03 square meters) 700 nm period epoxysilicone pattern on flexible PET substrate by R2RNIL process [52] (b) SEM image of the patterned grating structure[52], (c) SEM image of a 70nm line width, 100nm pitch grating structure [23]

Although R2RNIL has shown tremendous promise for developing ultra-small nanoscale optical structures with high throughput and at a fraction of the cost of conventional lithography tools on a large area substrate, it does not provide the capability of controlled placement of materials at desired locations on the substrate, which is a crucial requirement for developing integrated photonic components. Ink-jet printing, used in conjunction with R2RNIL manufacturing system, can provide excellent flexibility in terms of precise material placement, low material wastage, and full automation capability. Another advantage is that several flexible electronic components such as RFID tags, sensors, batteries, displays, photovoltaic cells, RF amplifiers, switches, antenna elements, driving electronics etc., can also be fully printed along with R2RNIL developed photonic nanostructures for developing fully printed, multifunctional conformal optoelectronic systems that can easily be attached to any surface.

Thus, a marriage between R2R nanoimprint lithography and R2R ink-jet printing forms a very strong manufacturing option for developing printed integrated photonic components on a flexible/conformal and light weight platform in a roll-to-roll fabrication process. It can tremendously improve the performance and provide new capabilities for several military and commercial applications including radar, communication, sensors,

EM wave detectors etc. A schematic drawing of a complete system concept describing the combination of imprinting and ink-jet printing is shown in Figure 1-7. A combination of patterning and layer deposition is capable of dealing with different critical dimensions and various materials.

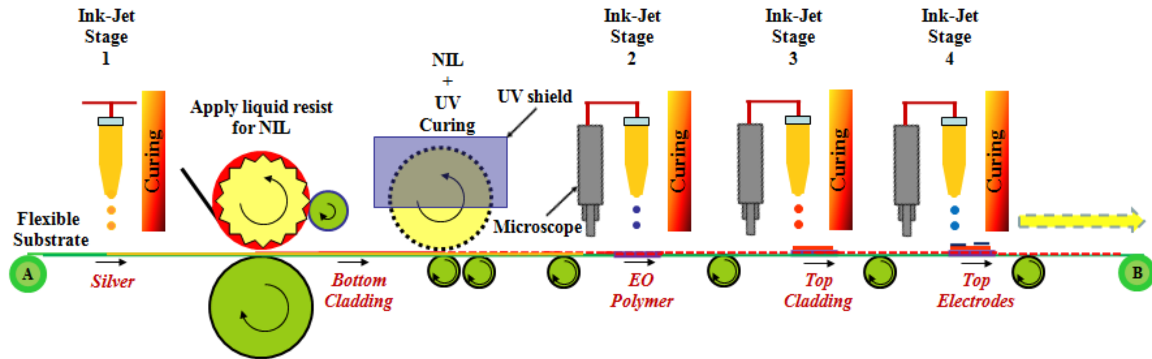

Figure 1-7 schematic of high rate, large area roll-to-roll (R2R) manufacturing of integrated photonic devices using a combination of nanoimprint lithography (NIL) and ink-jet printing processes on a flexible substrate. NIL forms sub-100nm patterns on polymer film. Ink-Jet enables precise placement of materials to form full optoelectronic device.

1.5 Dissertation organization

My dissertation will first focus on investigating the application of imprinting technology for optical components, including waveguides, optical couplers, etc. Then, by combining with novel ink-jet printing technology with imprinting, we demonstrate the optical board-to-board coupler, thermo-optic switch and electro-optic modulator. For high rate production, we customized a R2R ink-jet printing system.

In Chapter 1, we review different methods for fabricating optical waveguides and point out the advantages of using imprinting method. Besides, we also introduce the current applications of ink-jet printing technology and point out the advantages of combining imprinting and ink-jet printing technologies for various applications.

In Chapter 2, the focus is on molding optical waveguides. We first compare the different mold fabrication methods, and choose a low cost electroplated metal mold to pattern our waveguide. Experimental results reveal that the optical loss is reduced due to improved surface condition. Also, we extended this technology for making nano scale mold and patterns with good quality.

In Chapter 3, we start to use the electroplating mold and ink-jet printing method to demonstrate intra- and inter- board optical interconnects with 45° mirror and micro-lens as proximity couplers. The optical loss and high speed data transmission up to 10Gbps are evaluated with different board-to-board separations. It is proven that ink-jet printed micro-lenses greatly reduce the insertion loss and increase the quality of optical interconnects.

In Chapter 4, we utilize the total internal reflection effect to demonstrate a 2×2 optical switch. We optimize the device material system and structure to make it possible to be fabricated utilizing the combination of imprinting and ink-jet printing. The fabricated device shows less than 0.5ms switching time at 1 kHz.

In Chapter 5, we continue to demonstrate electro-optic polymer based Mach-Zehnder (MZ) modulator fabricated using imprinting and ink-jet printing. It is a complicated device that needs good registration of the electrode and waveguide patterns. We maximize the advantages of ink-jet printing method by depositing silver electrode right on top of modulator arm. The fabricated device shows decent performance with V_{π}•L=5.68V•cm.

In Chapter 6, with the technologies accumulated, we tried to design and fabricate a complicated electro-mechanical system, a roll-to-roll ink-jet printer, aiming at realizing auto registration when stacking multiple layers at high speed. The machine vision system

is established to realize active alignment on both X and Y directions. Customized software is developed using NI LabVIEW and two-layer registration is demonstrated.

In Chapter 7, the dissertation is summarized.

Chapter 2: Polymer Based Photonic Device with Imprinting Method

In this chapter, a comparison between molding methods and traditional ion etching method, in terms of fabricating polymer based photonic devices, especially waveguides, is presented. Admittedly, there is no single universal technology that fits all device dimensions or suitable for all applications. Thus, we will compare and discuss the pros and cons of each method in detail including their suitable applicable regimes.

2.1 COMPARISON OF MOLD FABRICATION METHOD

Generally speaking, based on the mechanical properties of the molds, they can be categorized into soft mold and hard mold.

Soft mold: PDMS mold is a kind of commonly used soft mold. PDMS has several excellent properties, such as its bio-compatibility, high chemical resistance, optical transparency, non-toxic, non-flammable and so on[53, 54]. For certain applications the elastic deformation of PDMS may have a fundamental limitation in resolution[55]. Thus, a more rigid PDMS which has relatively shorter cross-linkers is applied to serve as high modulus material to imprint finer features. Commercially available soft PDMS Sylgard 184 from Dow Corning can handle down to 500nm features[56], while h-PDMS can extend the capability of soft lithography down to the 50–100 nm regime[57]. Other than PDMS, PET based mold is featured by its flexibility, and can serve as soft mold for fine features.

Hard mold: Metal, glass or quartz molds[58] will deform less during imprinting process thus they are referred to as hard mold. The most widely used hard molds are silicon mold and quartz mold fabricated using “top down” material removal method. In our research, we investigated a different type of “bottom up” material build-up method for fabricating nickel hard mold using electroplating method, and a silicon dioxide mold

using e-beam evaporation method. The main process differences for material removal and material build-up methods are shown in Figure 2-1.

For the material removal method shown in Figure 2-1 (a), since silicon and SiO_2 etching equipment and recipes are relatively mature, it can always provide good uniformity across the mold. However, since the etching process is done by high energy ions, the surface roughness is high and this roughness will be carried down to the final device, which will increase the scattering loss for optical components. However, due to the maturity of the process, it is still the mainstream process for making imprinting master mold.

For the material build-up method as shown in Figure 2-1 (b), the mold top surface is naturally formed and the sidewall is also very smooth due to the fact that it is grown conformally to the photoresist sidewall. The electroplated Ni mold method is similar to LIGA and pseudo LIGA processes (German acronym for Lithographie/Lithography, Galvanoformung/Electroplating, Abformung/Molding) which comprise of pattern exposure, development, electroforming, resist stripping and replication steps, with the purpose of fabricating various structure in micron scale[59-62]. As of the thickness that can be electroplated, less than 100μm would be a good estimation. A typical application of using electroplating mold in our research is to mold a 50μm by 50μm multimode waveguide, which will be discussed in Chapter 3.

The e-beam evaporation method for fabricating mold as shown in Figure 2-1 (c) is actually a lift-off process. Compared to the electroplating method， the evaporation method avoids the resist exposure to other chemical solution and ensures the highest uniformity. However, only thin deposition can be achieved with low deposition rates (10-30 times slower than electroplating method.) Therefore, when coming to the application which requires thin and uniform film less than 500nm, for example, single mode rib

waveguide, this method would be the most suitable choice, since it also avoids high energy ion bombardment thus provides better surface smoothness compare to RIE etched mold.

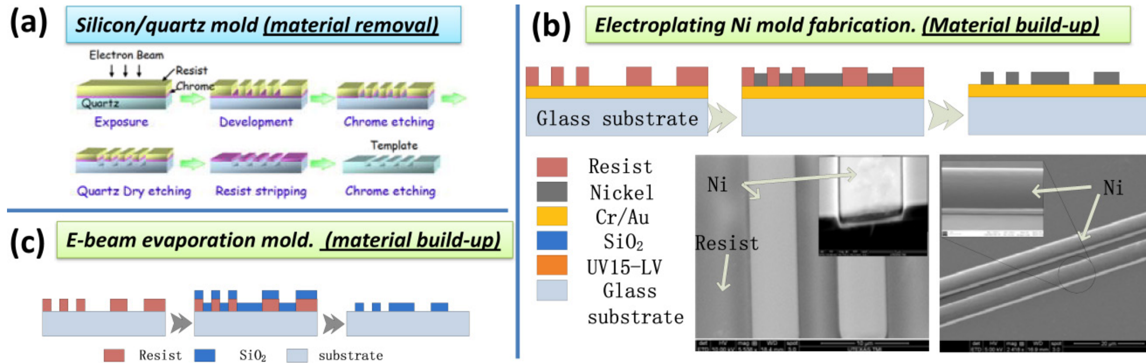

Figure 2-1 (a) quartz mold fabrication process[58], which represents a material removal method. (b) Electroplating method for fabricating Ni metal mold. (c) E-beam evaporation method fabricating Silicon Dioxide mold

To better illustrate the advantage of using imprinting method over e-beam method in photonic devices fabrication, polymer waveguides are fabricated using both methods and the surface quality and optical performance are compared.

2.2 Photonic waveguide fabricated by imprinting mold

In this section, we will describe in detail the fabricate process of a hard mold and a rib waveguide using both electroplating and e-beam evaporation methods, as shown in Figure 2-1 (b) and (c). The trenches formed by the imprinting process are shown and compared with the trench fabricated by reactive ion-etching method.

The process starts with mold fabrication. In the electroplating method shown in Figure 2-1 (b), 1mm thick glass slides are used as substrate and are coated with Cr/Au (10nm/50nm) as the seed layer for the electroplating process. Then, 5μm wide waveguide trenches are patterned using 1.45μm thick photo resist. Next, the samples are exposed to

two minutes oxygen cleaning using an Oxford Reactive Ion Etch (RIE) system so that the developed regions are left residue free. The samples are then transferred into an electroplating bath and connected to the cathode. Nickel is electroplated inside the developed region with sidewall conformal to the resist pattern. The resist is removed after the electroplating process. In the e-beam evaporation method shown in Figure 2-1 (c), it is not necessary to evaporate the seed layer and the photo resist is directly patterned on the glass slides. After resist residue removal, lift-off process is performed by evaporating 550nm of silicon dioxide and removal of the bottom resist.

The second step is the molding process which is a key step. Before molding, the mold is rendered hydrophobic by treating it with 1H,1H,2H,2H-Perfluorodecyltrichlorosilane 96% ($CF_3(CF_2)_7(CH_2)_2SiCl_3$) monolayer precursor solution. Waveguides are fabricated on the glass substrate that is pre-treated with the TranSpin adhesive promoter. The UV15LV polymer (from MasterBond, n=1.5@1550nm) is then coated as the bottom cladding layer in the waveguide system. The molding process is performed by bringing together the mold and the sample with proper pressure maintained for 20min, allowing the polymer to fully fill into the mold structure. Another 20min of UV exposure is performed to completely cure the surface. After curing, the mold and device substrate can be detached easily due to the low surface energy of hydrophobic treated mold surface. Finally, after acetone rinse, the mold can be re-used to imprint the next device substrate.

The third fabrication step includes filling the molded bottom layer with the waveguide core material (EO Polymer AJ-CKL1/APC from Soluxra, LLC, n=1.63@1550nm) and covering the core layer with the top cladding (UFC-170A from URAY Co., Korea, n=1.4956@1550nm) by spin coating and thermal curing. After facet dicing, the polymer waveguide is fabricated.

2.3 Quality evaluation

(1) Imprint quality evaluation.

The imprinted channel qualities using different kinds of methods are evaluated. The results are shown in Figure 2-2 (a). As can be seen roughly, the ion-etching method will cause surface damage while the molding methods using either the electroplating mold or the evaporation mold gives better surface quality. In order to further verify this conclusion, a zoom-in the SEM picture is also included which shows the clear texture of the sidewall. Atomic Force Microscope (AFM) is also employed to examine the surface roughness of the ion-etched channel and the imprinted channel (using e-beam evaporation mold), as shown in Figure 2-2 (b). From the AFM scan, it can be seen that a much smoother bottom surface is obtained from the molding method (Ra=4.92nm) than from the RIE etched method (Ra=9.71nm). In the RIE method, high energy ions bombard the surface not covered by the photo resist, thus relatively rougher surfaces are achieved. In the molding method, the mold fabrication employs "bottom-up" methods (electroplating and evaporation), in which the structure material accumulates conformally to the smooth sidewall of the resist. The pattern on the mold is finally transferred onto the polymer to get low surface roughness of the molded trench.

(2) The optical loss evaluation

The optical loss is evaluated after the completion of all waveguide layers. For the testing device, the bottom cladding layer is UV15LV with a refractive index of 1.51@1550nm; the core layer is EO-Polymer with a refractive index of 1.63@1550nm; and the top cladding layer is UFC-170A with a refractive index of 1.496@1550nm. The samples are cleaved to have same waveguide length and the same input/output facet condition. With the aid of auto-aligner, the optical loss of imprinted rib waveguide is

characterized. A 0.32dB improvement at 1560nm wavelength for 10mm propagation length is achieved from the molded waveguide, compared to the waveguide fabricated with ion-etching.

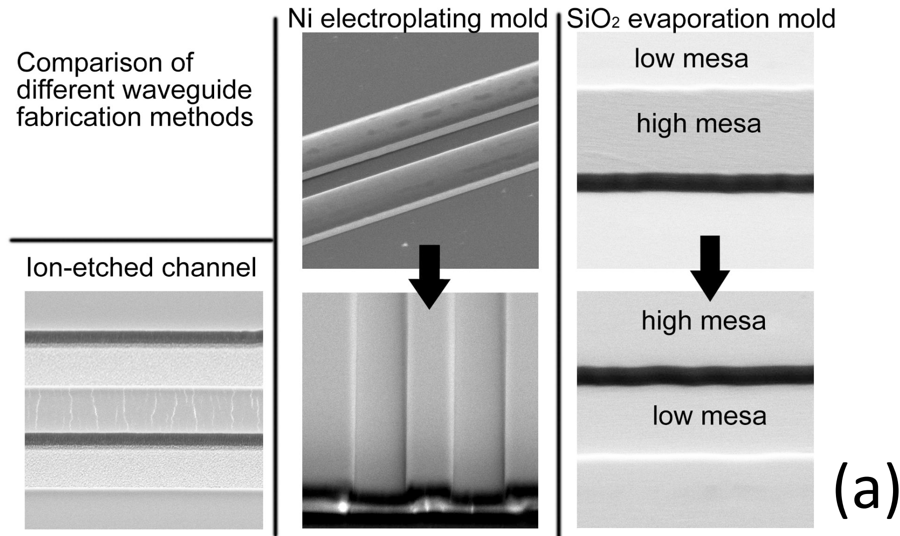

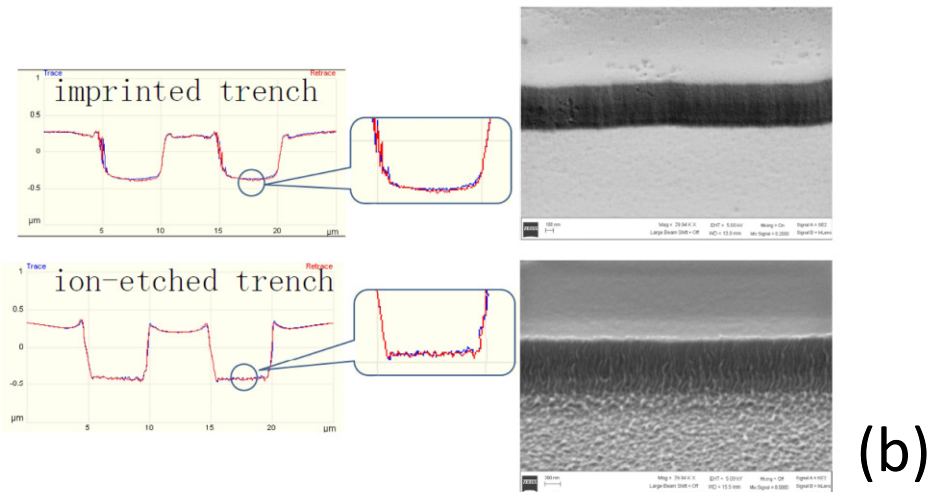

Figure 2-2 (a) comparison of different 5μm waveguide fabrication methods. (left): ion etched waveguide. (middle): molded waveguide with electroplated Ni mold. (right): molded waveguide with evaporated SiO_2 mold; (b) surface roughness evaluation with AFM scanning and SEM inspection, for imprinted sample and ion-etched sample

2.4 ELECTROFORMING FOR NANOSCALE PHOTONIC DEVICE STRUCTURE

When the required feature dimension is in the sub-micron level, with reasonable aspect ratio or reasonable depth of the feature, electroplating method for mold fabrication is feasible. A typical structure representing this dimension is a photonic crystal waveguide structure which comprises of a periodic array of holes/pillars. Although the pure polymer system cannot be used directly as the functional device due to its low index contrast with air, the patterned polymer can be used as an etch mask for the underlying substrate, such as a Silicon on Insulator (SOI) wafer. Employing the imprinting method will greatly reduce the cost by eliminating e-beam lithography step. Traditional mold for NIL purpose is very expensive, and if low cost electroplating process is used, the cost would be reduced significantly.

We started from fabricating pillar array to test the feasibility of electroplating nickel in sub-micron and nanometer scale regimes. With optimized parameters, nickel electroplating was executed on the photonic crystal arrays with 500nm hole diameter (1000nm period). Figure 2-3 (a) shows the results of electroplating with current density of 0.1mA/mm^2 for 60min. A uniform nickel cylinder array was successfully fabricated across the entire electroplated area. The inset picture in Figure 2-3 (a) shows the detailed zoomed in view of a single pillar. The cross-sectional image of the 500nm pillar array is shown in Figure 2-3 (b), demonstrating the height of electroplated nickel to be 400nm, which is identical to the thickness of the spin coated e-beam resist. Electroplating conditions are carefully controlled to prevent the nickel over-electroplating.

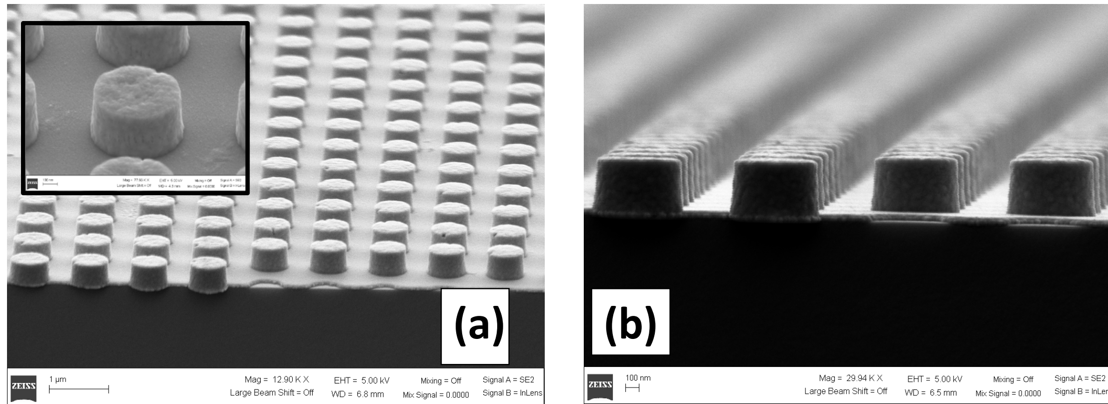

Figure 2-3 nanoscale pillar array with 500nm in diameter, with a pillar zoomed in.
(b) cross sectional view of the electroplated Ni pillar array

With success in the 500nm diameter pillar fabrication, we continued to try smaller sizes integrated with practical photonic crystal designs. Figure 2-4 shows a mold for hexagonal array of photonic crystal structures with a line defect, electroplated on a Ni coated glass substrate. Figure 2-4 (a) shows an overview of the entire photonic crystal Ni template area under SEM after developing and removal of the e-beam resist. The length of the photonic crystal area is 58.03µm. Figure 2-4 (b) shows the topography of the area where light is coupled in/out of the photonic crystal area. Figure 2-4 (c) shows the 90° rotated view of hexagonal array of the nickel pillars inside the photonic crystal area. The device design includes two straight waveguide areas with a photonic crystal area in-between. The lithography patterns are successfully transferred into a nickel mold with remarkable uniformity. The electroplating condition is optimized to $0.07mA/mm^2$ at 45^oC accordingly. The air holes have been designed to have diameters of 212nm and a period of 465nm to operate in the wavelength range of 1515nm to 1565nm. The mold is used to mold the polymer using Obducat nanoimprinting machine (located at Huazhong University of Science and Technology, Wuhan, China), and the result is shown in Figure 2-5. We are able to fabricate Ni mold with pillar diameter down to 90nm. The smallest

dimension is limited by the proximity effect with the current e-beam lithography system available to us, which makes the definition of smaller round features challenging. We believe it is possible to electroplate finer features with a more advanced e-beam system.

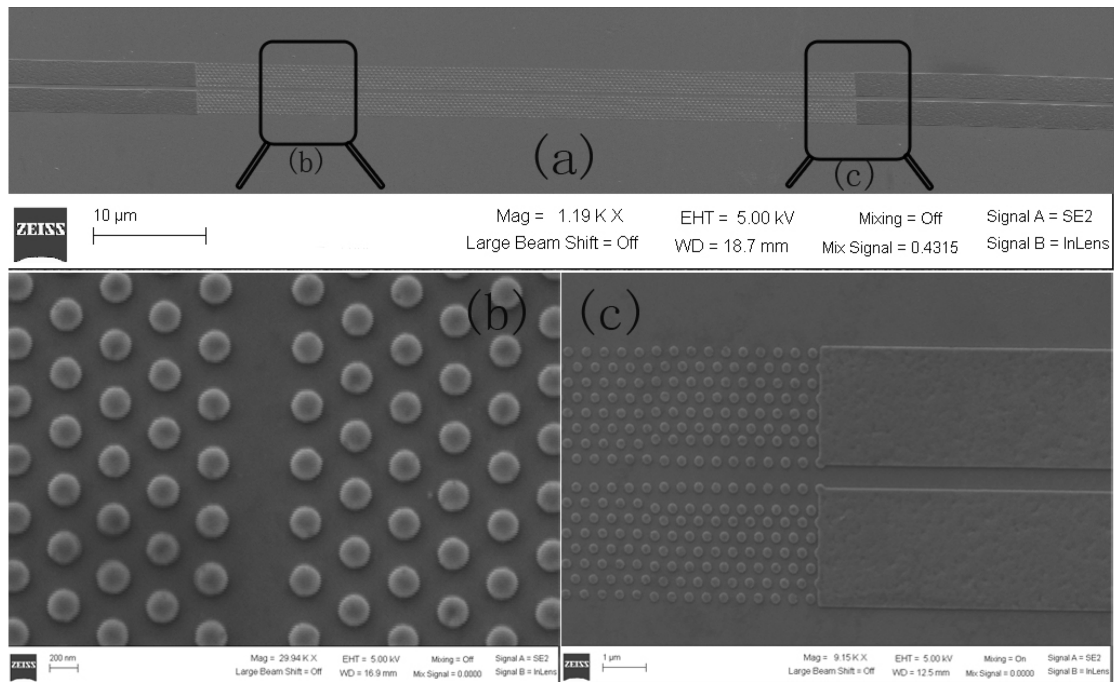

Figure 2-4 photonic crystal pattern and electroplated Ni mold. (a) overview of the device template; (b) zoomed in hexagonal array of photonic crystal structure template (rotate by 90°), scale bar: 200nm; (c) light input/output coupling area, scale bar: 1μm

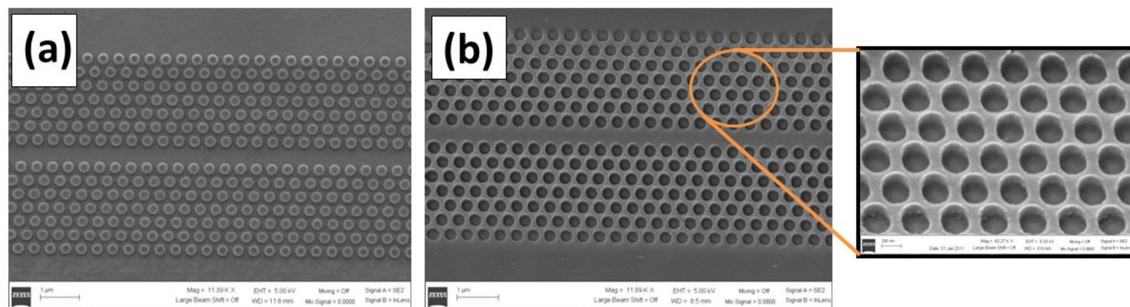

Figure 2-5 photonic crystal waveguide: (a) electroplated Ni mold. (b) imprinted polymer profile using Obducat NIL machine

2.5 CHAPTER CONCLUSION

In this chapter, we focused on using electroplating method and e-beam evaporation methods to fabricate mold for photonic components such as waveguides and photonic crystal structures. The imprinting method is shown to yield better surface smoothness, and thus, provide better optical performance over those waveguides fabricated by direct ion-etching method. When dealing with different feature sizes and step heights, different mold fabrication methods should be considered. Generally speaking, etched silicon mold is suitable for large area with less than 2µm step height. Electroplating mold is suitable for depositing larger features, for example 50µm step height. E-beam evaporation method is suitable when small step (less than 0.5µm) and high uniformity are required.

Chapter 3: Intra- and Inter- Board Optical Interconnects

In this chapter, we will demonstrate intra- and inter-board level optical interconnects using polymer waveguides and waveguide couplers consisting of both 45° total internal reflection (TIR) mirrors and ink-jet printed micro-lenses. Surface normal couplers consisting of 50 μm×50 μm waveguides with embedded 45° mirrors are fabricated using imprinting with a nickel mold. Micro-lenses, 70 μm in diameter, are ink-jet printed on top of the mirrors. We characterize the optical transmission between waveguides located on different boards in terms of insertion loss, mirror coupling loss, and free space propagation loss as a function of interconnection distance in free space. Each mirror contributes ~1.88 dB loss to the system, corresponding to 65 % efficiency. The printed micro-lenses improve the transmission by 2-4 dB (per coupler). Data transmission at 10 Gbps reveals that inter-board interconnects has a bit error rate (BER) of 1.1×10^{-10} and 6.2×10^{-13} without and with the micro-lenses, respectively.

3.1 CONCEPT OF BOARD TO BOARD OPTICAL INTERCONNECT

Optical communication systems are emerging as alternative interconnects at several levels including chip-to-chip [63, 64], intra-board [65, 66], board-to-board [67, 68], card-to-backplane [69, 70] and rack-to-rack interconnects [71, 72]. Optical interconnects consisting of arrays of Vertical Cavity Surface-Emitting Lasers (VCSELs) and Photo-detectors (PDs) have been shown to be superior to copper based electrical interconnects in terms of cost, power, and bandwidth [73, 74].

Parallel data transmission through optical means between boards has been demonstrated with complex packaging involving discrete micro and macro lenses and stage-alignment tools [75, 76]. Free-space optical interconnects between VCSELs and PDs placed on separate boards have been demonstrated in which, fixed integrated micro-

lens arrays [77, 78] or MEMS controlled lens arrays were used to lower optical loss by reducing the beam divergence [79-83]. In this chapter, intra-board and inter-board optical interconnects are demonstrated. Intra-board interconnects are realized using 50 µm×50 µm polymer waveguides. Inter-board coupling scheme is realized by 45° mirrors and integrated ink-jet printed micro-lenses. It provides free-space optical interconnects between waveguides located on different boards. The 45° mirrors, which are fabricated through a 3D molding technique, enable vertical coupling of guided-wave with high efficiency. Ink-jet printed micro-lenses are shown to significantly decrease the divergence and increase the quality of collimation of the vertical beam.

45° mirror couplers were previously used for integrating VCSELs and PDs in one of PCB board layers by Choi [84], Liu[85] and Wang [86]. 6 dB (0.5 mm transmission line) and 6.4 dB (80 mm waveguide) coupling losses, including two 45° mirrors, respectively were reported by Chen [87] and Van Hoe [88]. More recently, Jiang [89] and Inoue [90] reported 1.74 dB and 2.3 dB coupling loss, respectively for one 45° mirror. The lowest loss was reported in ref. [91], where a mechanical saw with a 90° V-shaped diamond blade was used to make 45° mirror with 0.5 dB loss.

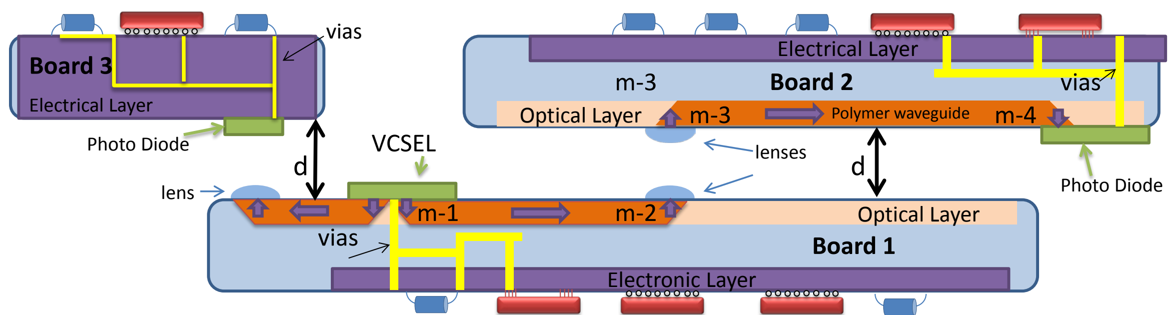

Figure 3-1 inter- and intra-board optical interconnects with polymer waveguides and 45° couplers with ink-jet printed micro-lenses.

In this work, we fabricate embedded total internal reflection (TIR) mirrors in a single-step molding process using Nickel mold. Similar process has been reported by Wang[92] but using silicon mold. The embedded mirrors together with the ink-jet printed micro-lenses on top serve as proximity couplers for board-to-board free-space optical interconnects between two molded waveguides on separate boards. A schematic of the presented board-to-board optical communication scheme is shown in Figure 3-1. The VCSEL and PD can be controlled by signals transmitted through vias from the electric layer to the other side of the board. The boards are positioned back-to-back to enable the data transfer via the optical couplers. This technique can be used to couple light between waveguides, i.e., light from a VCSEL into an input waveguide, or light from an output waveguide into a PD. We investigate the optical transmission quality in setups using two mirrors and four mirrors in the optical path. Losses as a function of different board-to-board separations are also measured. In order to investigate the effects of ink-jet printed micro-lens, insertion losses with and without the micro-lenses are compared.

3.2 Fabrication of Polymer Based Waveguide Structure

We fabricate polymer waveguides with embedded 45° mirrors using molding method on a flexible substrate and attach it to the silicon chip. The fabrication is composed of four main steps as illustrated in Figure 3-2: (a) SU8 pre-mold fabrication, (b) nickel metal mold by electroplating, (c) molding process, and (d) waveguide fabrication. SEM pictures (for steps a, b and c) and microscopic pictures (for step d) are also shown.

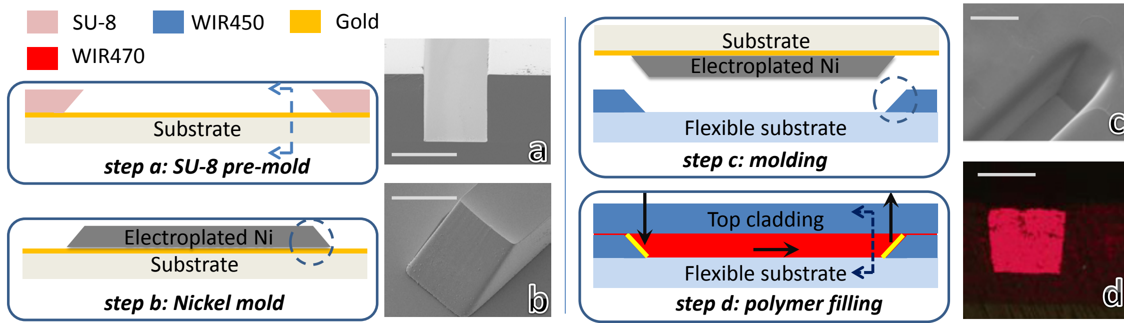

Figure 3-2 fabrication process for molded channel waveguide with 45° embedded mirror coupler. The scale bar represents 50µm length.

(1) SU8 pre-mold fabrication

The 1st step (step a) is making SU8 pre-mold with 45° mirrors on both sides. The pre-mold is used as a template for the nickel hard mold, and its fabrication quality is of great importance for all the following steps. First, a thin layer of 5 nm/50 nm Ti/Au layer is coated by evaporation and serves as a seed layer for electroplating nickel performed in step b, as shown in Figure 3-2. Following this, a 50 µm thick SU-8 layer is deposited on the seed layer and patterned by immersed tilted exposure to form the 45° slants. The detailed description can be found in [93].

(2) Nickel hard mold electroplating

In this step, Nickel is electroplated on the SU8 template. Compared to the evaporation/lift-off methods, electroplating is featured by its high deposition rate and makes it possible to deposit 50µm with controlled deposition rate. We use a Ni electroplating kit that is commercially available from Caswell Inc. The pre-buried Ti/Au layer serves as the seed layer for electroplating. In order to achieve the required adhesion between the seed layer and the nickel layer, the electro-plating current density is initially kept low at 1 mA/cm^2 for 5 minutes. Then, the current density is raised to 10 mA/cm^2 to achieve a deposition rate of 120 nm/min. At the end, a low current density 1 mA/cm^2 is

applied for 5 minutes to improve film quality. Next, the SU-8 resist is removed by Remover PG to release the nickel mold. The cross linked SU-8 resist is hard to be removed by any solvent therefore, it is important to have a release layer underneath the SU-8 layer, for example Omnicoat, to help peel off the cross linked SU-8 completely.

(3) Imprinting the channel on the bottom cladding

A 200µm thick flexible TEONEX thin film (from DuPont Teijin Films Inc.) serves as the substrate. The bottom cladding material WIR30-450 (n=1.45@850 nm) is spin-coated on the substrate together with an adhesion promoter in-between, followed by Ultraviolet (UV) light curing. To ensure the mold can be effectively detached from the substrate during the molding process, AZ5209 photo resist is spin-coated on nickel hard mold as the release layer. After molding, the polymer is UV cured. Next, the de-molding process is completed in acetone, which dissolves the photo resist in-between the mold and device.

(4) Waveguide layer and embedded mirror formation

The molded bottom cladding layer is mounted on the evaporation chamber and 200nm of gold is coated onto the slope region using a shadow mask. Gold coating helps to enhance the reflectivity of the mirror, which in turn increases the coupling efficiency. The imprinted trenches are filled with the core material WIR30-470 (n=1.47@850 nm). Next, the core material is UV cured for 12 min followed by coating of the top cladding WIR30-450 (n=1.45@850 nm).

3.3 Fabrication of ink-jet printed micro-lenses

Micro-lenses are used to reduce the divergence angle of the output light from the 45° mirrors. The micro-lenses have been fabricated based on photoresist melt-and-reflow technique [94]. In this work, the micro-lenses are directly ink-jet printed over the 45°

mirrors, similar to the method reported in [95]. In our experiment, we use diluted glycerol (glycerol:BPS=3:7 by volume) to form the micro-lens with index of 1.46556 at 850 nm wavelength. The ink-jet printer is Dimatix Materials Printer (DMP-2800) from Fujifilm. It utilizes a piezoelectric printing cartridge (DMC-11610), which dispenses a nominal volume of 10pL each cycle for one nozzle. By specifying the desired printing position, the micro-lens can be placed above the targeted 45 mirror coupler with good accuracy. Figure 3-3 (a) and Figure 3-3 (b) show the top view of the mirror before and after ink-jet printing the micro-lens. A contact angle goniometer is used to take the profile of the droplet, as shown in Figure 3-3 (c).

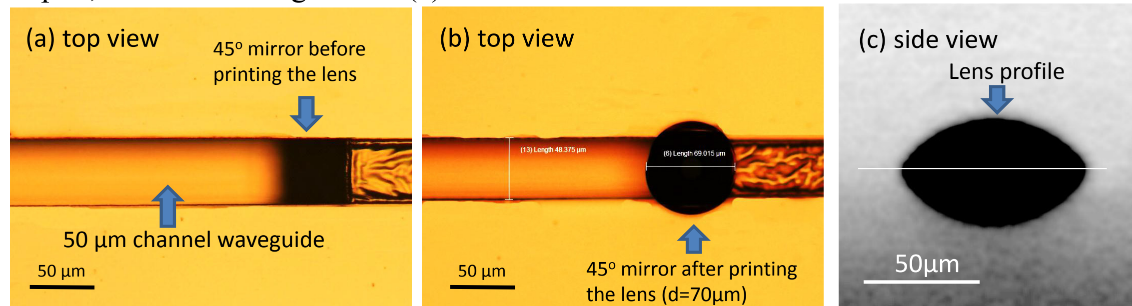

Figure 3-3 (a) top view of embedded mirror before printing micro-lens (b) top view of embedded mirror after printing micro-lens with d=70µm. (c) the lens profile taken by contact angle goniometer.

The lens profile, which determines the focal length, can be adjusted by varying the viscosity of the printed material or surface properties of the substrate. Also, UV curable material can be adopted and cured to permanently fix the shape of the micro-lens [95]. Different focal lengths have been reported, for example, 48 µm [96], 55-153 µm [97], a few hundred microns [79, 98-100], or in millimeter range [67], with different materials and lens profiles. Currently, the printed droplets in this work are 70µm in diameter with 100-150 µm focal lengths estimated using the relations in [101]. The focal length can be controlled by the combination of surface properties, material viscosity and

ink volumes. By fine tuning the lens profile, optimized focal length can be achieved to make sure that light gathered in the receiving end is maximized.

3.4 Optical evaluation of board to board interconnects

(1) Testing setup

Schematics of the board-to-board interconnect using the 45° mirrors are shown in Figure 3-4. In the first experimental setup, shown in Figure 3-4 (a), a VCSEL (850nm) is coupled to a 4.5 cm polymer intra-board channel waveguide through a 45° mirror. Another 45° mirror is used to couple light out of the waveguide. A PD placed on a separate board converts the optical signal into an electrical signal. In the second experiment setup, shown in Figure 3-4 (b), two identical waveguides (each 4.5 cm long) on separate boards with adjustable separation d are used to couple light from a VCSEL on one board to a PD on the other board through using four 45° mirrors. We also compare cases with and without micro-lenses. Figure 3-4 also shows the 632nm visible light spots at the output end of 1st board and 2nd board in the second experimental setup, which helps in pre-aligning two boards.

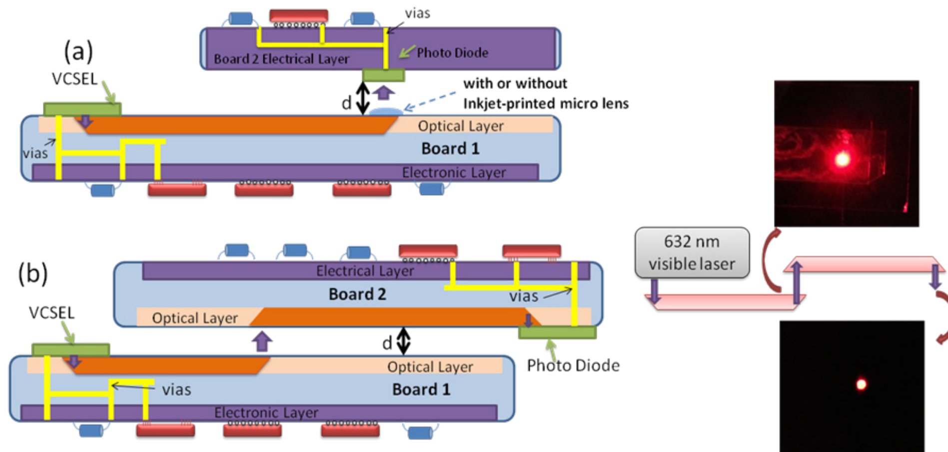

Figure 3-4 board-to-board experimental setup showing (a) one waveguide with two 45° mirrors (b) two waveguides with four 45° mirrors. Visible spots show the output after 2 mirrors and 4 mirrors. Optical loss evaluation

Figure 3-5 shows the variation of the measured 850nm optical power from the PD as a function of the separation between the boards. The total optical loss is composed of the free space propagation loss and the insertion loss, which is determined by the coupling method and the propagation loss of the polymer waveguide. It can be seen from Figure 3-5 (a), for d=0 (where the free space propagation loss is zero), that the measured insertion loss (without a micro-lens) is 4.586 dB. We have measured the propagation loss and scattering loss for the WIR polymer waveguides fabricated using molding method, and the loss was found to be 0.18dB/cm[93]. Therefore, each 45 mirror coupler contributes 1.888 dB loss to the optical path total loss, which corresponds to 64.86% coupling efficiency. Due to the divergence of the light coupled out of the waveguide by the 45° mirror, the total optical loss increases with increasing d. The divergence angle of the out-coupled beam can be reduced when a micro-lens is inserted in the optical path. Figure 3-5 shows 1.5 dB improvement at shorter separation (1-2 mm) and 3.7 dB improvement at larger separation (4 mm).

Furthermore, the free space coupling loss due to the beam divergence can also be extracted from the total insertion loss, as shown in Figure 3-5 (b). For comparison, the loss versus distance result from a previous report that utilized relatively larger lenses (240μm in diameter) mounted on both the output and input ends [67] is also plotted. The minimum loss on the results from [67] occurs at a free space propagation distance corresponding to the confocal length of the two lens system.

For the second experiment, the total insertion loss in 12 dB at d=1 mm. The difference between the total insertion loss values from the two experiments remains about 4.4~4.8 dB (average=4.528 dB) regardless of d as long as it is within 3mm. By subtracting the propagation loss (0.18 dB/cm) from all the waveguides in the second experiment, we estimate the coupling efficiency of each of the extra 45° mirrors in the

second experiment to be 65.22%, which is very similar to the mirror coupling efficiency of the 1st board. Since the two channels are molded with the same nickel hard mold, it further confirms the process stability for such molding fabrication process.

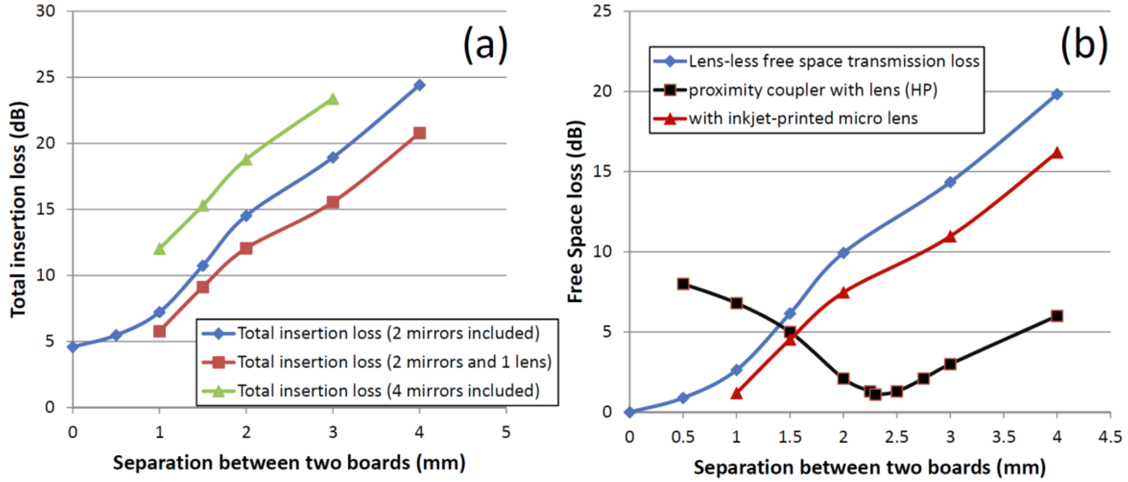

Figure 3-5 (a) total insertion loss with the separation between two boards, when 2 mirrors, 2 mirrors w/lens and 4 mirrors are included; (b) transmission loss in free space when using 45° coupler with/without lens and proximity coupler with lens from [67]

(2) High speed communication:

Beside loss evaluation, we also conducted high-speed test on the samples using the setup shown in Figure 3-6 (a). Light from VCSEL is directly modulated at RF frequencies ranging from 1GHz to 10GHz with random signal level of ±0.3V using Agilent ParBERT 81250 system. The separation between the input and the output boards is varied as before. The Q factors measured at d=0, d=1 mm and d=2 mm, with and without the ink-jet printed micro-lens, as shown in Figure 3-6 (a). The corresponding Bit Error Rate (BER) data is shown in Figure 3-6 (b). The Q factor decreased quickly for d=2 mm, indicating a high loss and large divergence of the beam in free space. In modern optical networks, data communication with a BER<10^{-9} is considered “error-free” [102,

103]. Without a micro-lens, at d=2 mm separation case, only data rate below 3 Gbps can be transmitted error-free. On the other hand, micro-lenses increase the error-free data transmission to 7 Gbps. The eye diagrams at selected points are shown in Figure 3-7, which indicates the improvement of the signal quality by the micro-lenses.

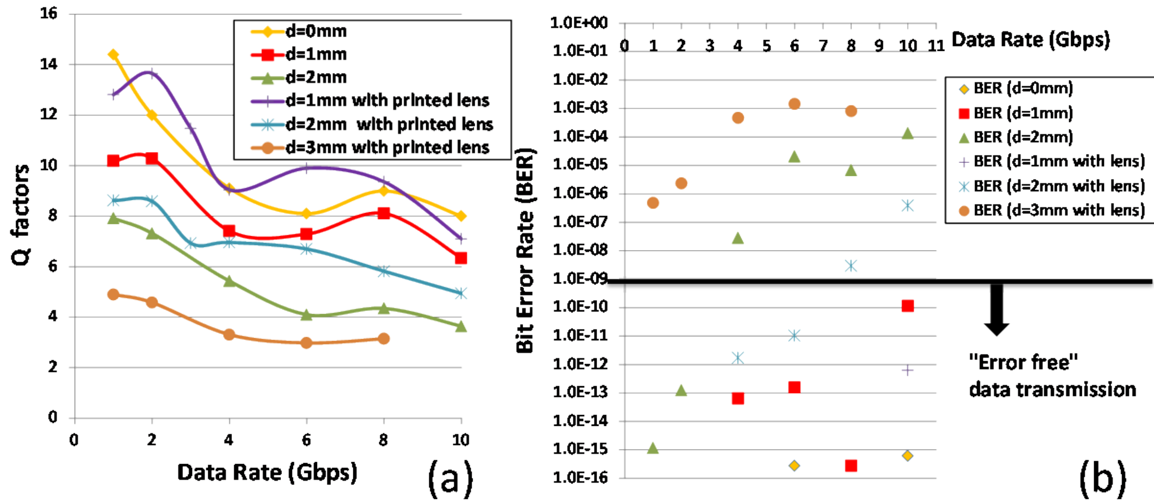

Figure 3-6 (a) Q factors with different data rate, at different separations. Two mirror couplers are included in optical path. (b) Bit Error Rate (BER) distribution with data rate at different separations with/without ink-jet printed lens.

3.5 CHAPTER CONCLUSION

We presented intra- and inter-board optical interconnects using 45° mirror couplers and ink-jet printed micro-lens. The molding method using a low-cost electroplating technique was described and applied for optical layer fabrication. Micro-lenses (70 µm in diameter) were fabricated using an ink-jet printer. Each 45° mirror was shown to contribute about 1.88 dB loss (65% in coupling efficiency) to the total optical loss. The molded intra-board polymer waveguides gave 0.18 dB/cm loss. When propagating in free space without a lens, 2 mm separation gave result of 9.9 dB loss, which was reduced to 7.5 dB when a micro-lens was inserted in the path using ink-jet printing. At this separation, the maximum error free data rate (BER<10^{-9}) was measured

to be 3.5Gbps and 7.5Gbps, with and without the micro-lens, respectively. At 10Gbps with micro-lens presented, 1mm and 2mm separation yielded BERs of 6.2×10^{-13} and 3.9×10^{-7}, respectively. We expect that reducing the surface roughness and angle variation of the 45° mirror will further improve the coupling efficiency. Also printing micro-lenses on both the input 45° mirror and the PD or the receiving 45° mirror in a confocal setup will significantly reduce the free-space propagation loss. To the best of our knowledge, this is the first report of free-space coupling between waveguides on separate boards.

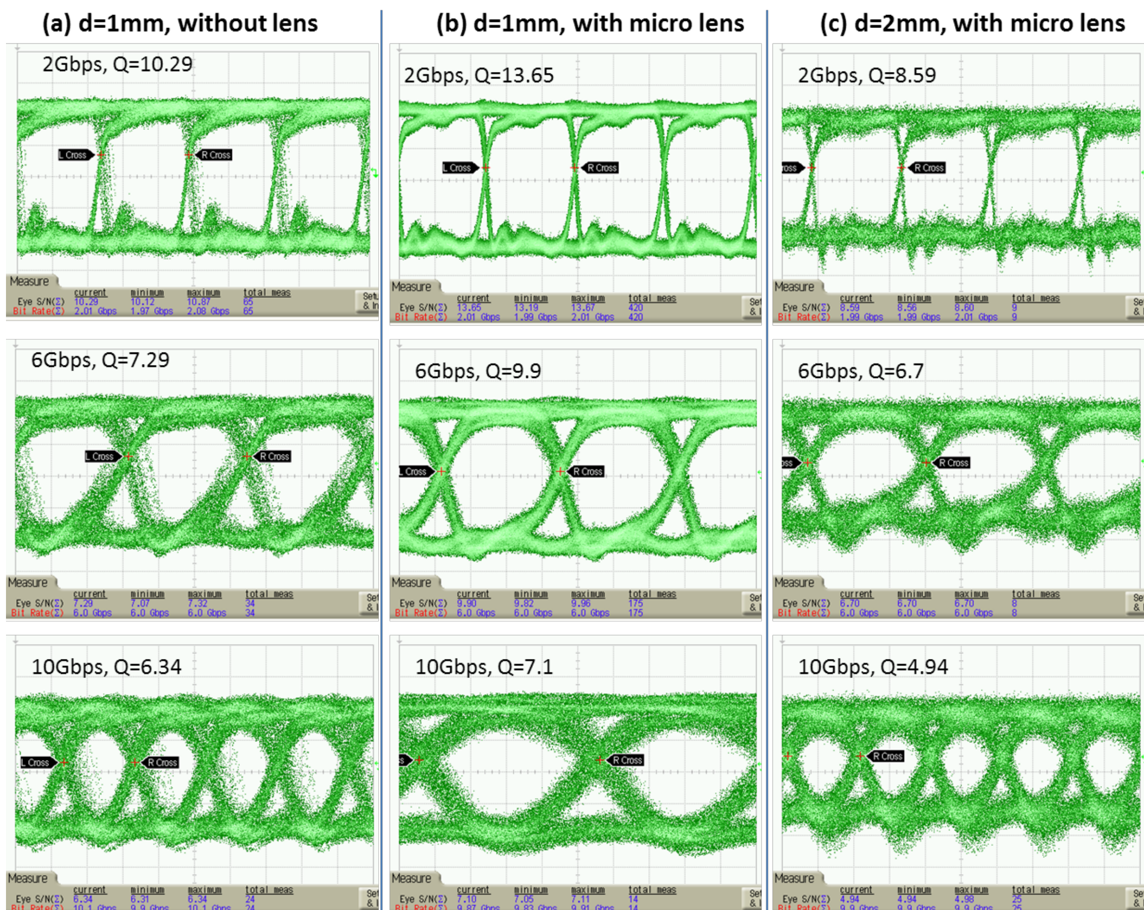

Figure 3-7 eye diagrams at selected data rate (2Gbps, 6Gbps and 10Gbps): (a) 1 mm separation with 2 mirrors; (b) 1 mm separation with 2 mirrors and 1 lens; (c) 2 mm separation with 2 mirrors and 1 lens.

Chapter 4: Printable Total Internal Reflection (TIR) Based Thermo-Optic (TO) Switch

In this chapter, we will demonstrate a printable 2×2 switch Thermo-Optic (TO) switch utilizing imprinting and ink-jet printing techniques. The material system, optical and thermal designs are discussed. Imprinting technique is used to transfer a 2×2 switch pattern from a flexible mold into a UV15LV polymer bottom cladding. Ink-jet printing is further used to deposit a SU-8 polymer core layer on top. Operation of the switch is experimentally demonstrated up to a frequency of 1 kHz, with switching time less than 0.5ms. The printing technique demonstrates great potential for high throughput, roll-to-roll development of low cost photonic devices.

4.1 Concept of optical switch

Material system design: In order to enable device development, the material system choice should meet certain criteria: First, all the materials should satisfy the optical index requirement to form a waveguide. Second, the bottom cladding layer should be imprintable. Third, the core layer should have sufficient thermo-optic coefficient so that a suitable change in the index is achieved within a small temperature gradient. Fourth, the core material should have suitable viscosity to be ink-jet printed. In order to satisfy the physical and optical characteristics, we selected UV15LV (n=1.501@1.55µm) from MasterBond as the bottom cladding layer, SU8-2000.5 (n=1.575@1.55µm) from MicroChem as the core layer and UFC-170A (n=1.496@1.55µm) from URAY Co. Ltd as top cladding layer. Of the three layers, the bottom cladding material UV15LV and the core layer material SU-8 2000.5 are ink-jet printable. Although LFR/ZPU series TO polymer from ChemOptics, Korea, with its high TO coefficient of ~ -2.5×10^{-4}/K @1.55µm, is an ideal choice for TO polymer switch development [11, 104, 105], its

lower refractive index ($n < 1.48$) compared to UV15LV, rules out its use as a core material. Moreover, the wide availability, low cost, and higher refractive index of SU-8 polymer is beneficial for low cost polymer device development in spite of its lower TO coefficient of -1.1×10^{-4}/K @1.55μm.

Optical and thermal design: A schematic of the 2x2 thermo-optic polymer TIR switch is shown in Figure 4-1 (a). The design of the switch includes two major issues: the optical design and the thermal design. The optical path and waveguide cross section are designed and simulated, as shown in Figure 4-1 (a)-(c), with a horn structure. A rib waveguide structure is used and the core layer consists of a 1.8 μm thick slab and a 5 μm (width) x 0.5μm (thick) strip. The separation of two input and two output waveguides is set at 250μm, which is compatible with a standard fiber array. A curved waveguide with 10mm bending radius is used to guide light from the input port to the X junction. A horn structure [106] is used at the junction, with a maximum width of 40 μm at the center. The half branch angle for the X junction is optimized at 4° based on the consideration of cross-talk minimization and switching power trade-off. Larger junction angle requires more power to switch the light while smaller junction angle will increase the cross-talk between two ports. Besides, the horn structure is also compatible with the temperature gradient generated by the heating element. The heating element is designed to have a width of 8μm at the center. Due to its thinness compared to other connecting parts, most of heat is generated at the center region only. Due to the relatively thin electrode, when heated up, the temperature difference between the electrode and the SU-8 layer is less than 5°C, according to simulation. If it is assumed that only the polymer layers beneath the heating electrode undergo a change in refractive index, a -0.02 index change in the SU-8 layer is needed for reflecting all of the input light from one arm to the other at the X junction. Since SU-8 has a thermo-optic coefficient of -1.1×10^{-4}/K, the temperature

change required is over 180°C. However, in reality, the heat distribution beneath the electrode takes a Gaussian profile. Therefore, the adjacent polymer will also get heated up, thus lower the temperature change required, and thus, the electrical power needed to total internally reflect the light. The simulated fundamental mode in the waveguide are shown in Figure 4-1 (b), where the mode is well confined within the waveguide region and does not extend more than 3μm into the cladding, which helps in reducing the absorption loss from the gold heating electrode. The simulated powers in the bar (blue) and the cross (green) ports for the switching condition are also shown in Figure 4-1 (c).

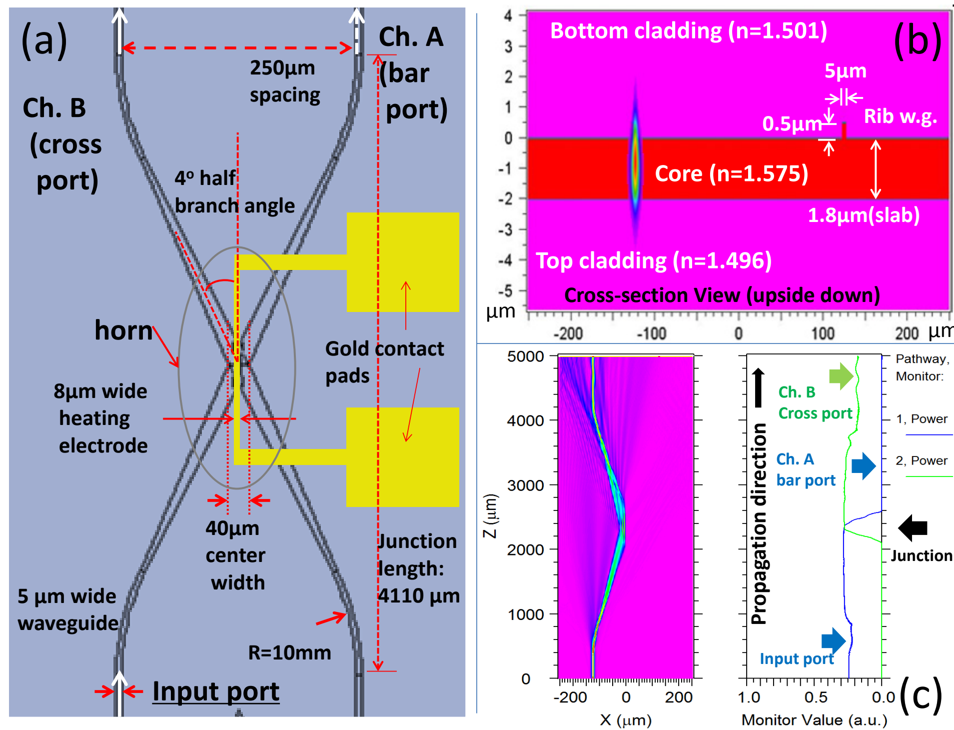

Figure 4-1 (a) schematic showing the top view of the 2×2 thermo-optic switch layout. A horn structure, with a half branch angle of 4o is used. Gold heating electrode is 8 μm wide over the center region of the horn. (b) The cross-section view and the simulated mode profile at the input side of the 2×2 TO switch. The mode is well confined in the waveguide. Core layer is composed of 1.8 μm thick slab and 0.5 μm (height) × 5 μm (width) strip. (c) Simulation results of the power outputs from the bar (blue) and the cross (green) ports when the junction is in switching condition

4.2 FABRICATION PROCESS

As mentioned in Chapter one, similar to other polymer devices, thermo-optic polymer TIR switch are typically fabricated utilizing reactive ion etching method to remove polymer materials. The disadvantages of this method include long fabrication time, low throughput and high cost. In the present research, a UV based imprinting method is employed to define the waveguide channel. Also, this method is compatible with roll-to-roll processing, and has the potential for high speed, low cost device fabrication. The soft mold fabrication and imprinting process are performed using imprinting tools from Dr. L. Jay Guo's group at University of Michigan. The equipment used for imprinting is NX-2000 Full-Wafer Universal Imprintor from Nanonex. For the presented thermo-optic switch, besides imprinting, we also integrate an ink-jet printing method to deposit the core layer. The fabrication process flow is shown in Figure 4-2. First, a flexible mold is fabricated using a silicon hard mold. The flexible mold is then used to define the core region in a UV15LV bottom cladding layer, which is coated on a silicon substrate [Figure 4-2 (b)]. Following this step, an ink-jet printer is used to print a layer of SU8 2000.5, which not only fills the core trench, but also forms a planar top surface for further processing [Figure 4-2 (c)]. SU8 has a dynamic viscosity of SU-8 varies from 14.7 mPa·s at 60°C to 8 mPa·s at 85°C and surface tension of 47±1 $mN \cdot m^{-1}$ at room temperature[97]. Thus, while printing, the nozzle temperature is increased to 40°C to increase the jetting quality. Upon curing, another layer of UV15LV is ink-jet printed on top to form the top cladding layer. Please note that we have found the gold heater electrode fabrication process (lift-off method) incompatible with the printed UV15LV layer. Therefore, for demonstrations, we have chosen UFC-170A as a top cladding layer. In future, by switching to another R2R process for electrode transfer

[107], UV15LV can replace UFC-170A. The detailed fabrication steps are provided in the following sub-sections.

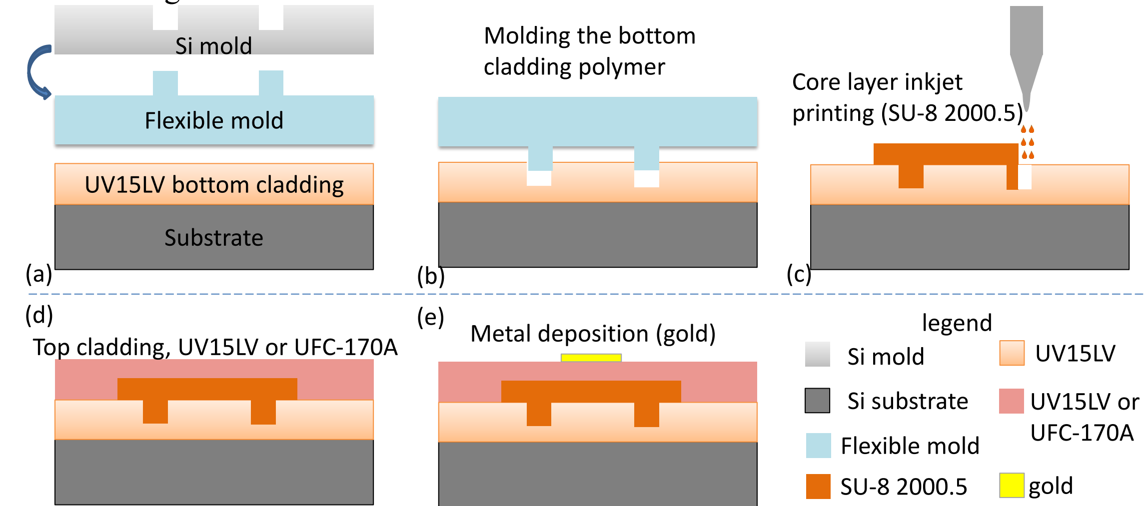

Figure 4-2 process flow for fabricating a 2x2 thermo-optic polymer switch using imprinting and ink-jet printing method

(1) Mold fabrication

Imprint mold fabrication is a critical step for determining device performance. The hard and soft mold fabrication processes are shown in Figure 4-3 (a) and (b), respectively. We start with a 4” silicon wafer for master mold fabrication. A 50nm layer of silicon dioxide is deposited onto the silicon wafer using PECVD. A 900nm thick photoresist is then spin coated on top and patterned to form an etching mask for the oxide layer. The waveguide pattern on the photoresist is then transferred to the oxide layer via dry etching using RIE. Then, silicon is etched by RIE using oxide as hard mask. Due to the high selectivity of silicon oxide and silicon, vertical sidewall is achieved. The etching depth is chosen to be 0.5 μm. After silicon etching, the oxide hard mask is removed by buffered oxide etch (BOE), which completes the master mold fabrication. Then, the fabricated silicon master mold is used to fabricate a transparent flexible mold on

polyethylene terephthalate (PET) substrate. The transparent flexible mold fabrication starts from spin-coating a photo-curable silsesquioxane (SSQ) resist on the PET substrate at 2000rpm for 60s, which results in a thickness of around 2 μm for the film. After that, the sample is pre-baked on a hot-plate at 100°C for 5mins. At the same time, the master silicon mold is cleaned in piranha solution for 30mins to grow a thin layer of fresh silicon oxide layer. Then, the master mold is vapor-coated with anti-sticking layer. After anti-sticking layer coating, the SSQ coated PET substrate is placed on the top of the silicon mold. Then, the sample is placed inside NX-2000 pressure chamber to perform a UV imprinting process at 250psi. After the SSQ resist is fully cured, the master mold and the PET substrate are separated by de-molding process. Thus, the SSQ mold is successfully fabricated on the transparent flexible PET substrate. The advantage of using two types of molds is that, even if the soft mold degrades after several imprinting processes, it can readily be duplicated from the original silicon master mold. Besides, the reason that we choose silicon as hard mold, rather than electroplating metal or evaporated oxide, is that silicon mold is more suitable to provide high uniformity over a large area and it is more reliable to be rendered hydrophobic to ensure successful de-molding.

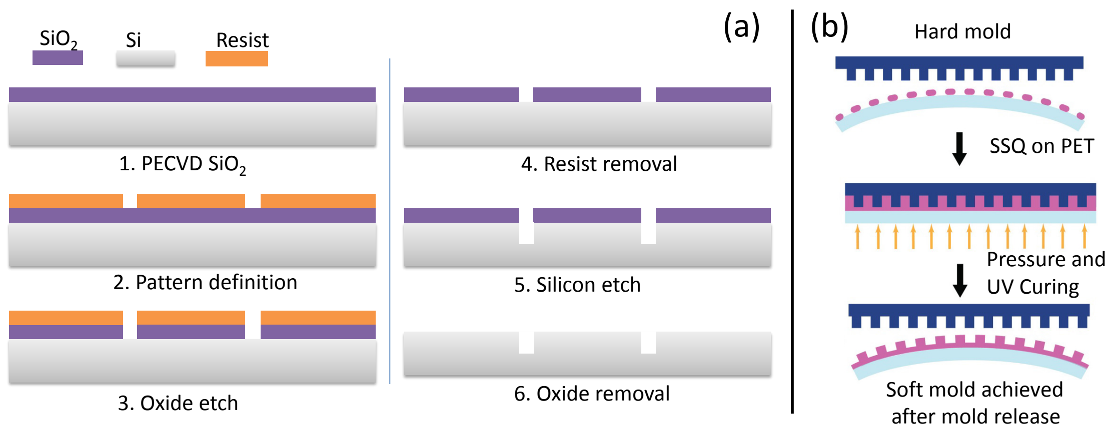

Figure 4-3 (a) silicon master mold fabrication process (b) soft mold replication from master mold

(2) UV-imprinting

The UV imprinting process is used for transferring the pattern from the soft mold to the bottom cladding polymer (UV15LV). This work is performed by Dr. L. Jay Guo's group at University of Michigan using NX-2000 Full-Wafer Universal Imprintor. First, the fabricated transparent flexible SSQ mold is vapor-coated with anti-sticking layer at 100°C for 1 hour. Then, the SSQ mold is brought into conformal contact with a silicon wafer coated with UV15LV resist. After that, UV-imprinting is performed in a pressure chamber with a pressure at 250 psi. Then, the imprinted UV15LV resist is fully cured by exposure to UV light. Figure 4-4 (a), (b) and (c) show the SEM images at the junction area of the silicon master mold, SSQ soft mold and the molded trench on UV15LV, respectively.

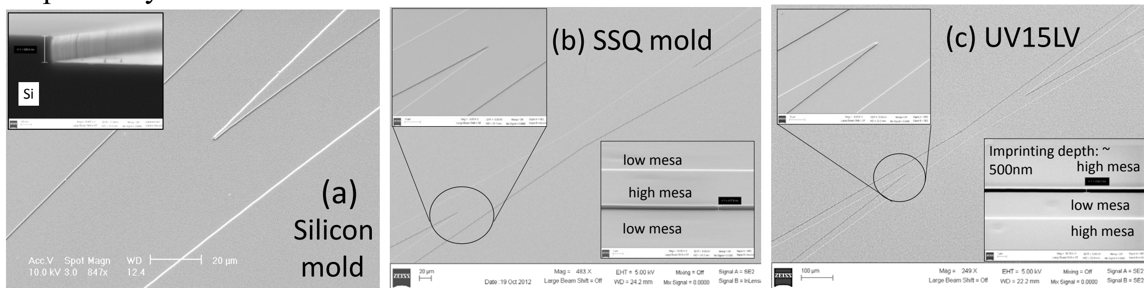

Figure 4-4 SEM images of (a) silicon mold (b) SSQ soft mold (c) imprinted UV 15LV at the junction area of the TO switch. The inset in (a) shows the cross-section views of the silicon mold, with 500nm step height. The upper left insets in (b) and (c) show the zoom-in views of the merging points of two waveguides. The lower right insets in (b) and (c) shows the tilted view of mold and imprinted trench in the 5 μm wide input/output regions

(3) Ink-jet printing

The same printer DMP-2800 is used for this device. As mentioned above, SU-8 2000.5 resist is used as the core layer. The jetting profile in the printer is optimized to ensure a uniform printed layer. The parameters can be controlled to tune the layer thickness between 1 and 2 μm. The printed SU-8 also fills the patterned waveguide

region in the UV15LV bottom cladding layer to form a rib waveguide structure. After printing, the substrate is pre-baked at 90°C to remove the solvent and then exposed to UV for 30s, followed by post-baking to fully cross-link the SU-8 layer. Following this step, another layer of UV15LV is ink-jet printed on top and cured to form the top cladding layer. SEM cross section image of the fully printed device is shown in Figure 4-5 (a). However, as mentioned above, due to incompatibility of UV15LV with the following electrode formation process, a 3 μm thick UFC-170A polymer is used as the top cladding layer for device demonstration, as shown in Figure 4-5 (b). Note that a roll-to-roll compatible electrode transfer method [107] can also be used to overcome this problem.

Compared to spin-coating method, comparable film quality can be achieved using ink-jet printing, with an added advantage that the printing method is more flexible because one can easily define the region of material placement, without going through an additional photolithography step. It will also reduce the potential risk of material incompatibility issue that may occur during photolithography.

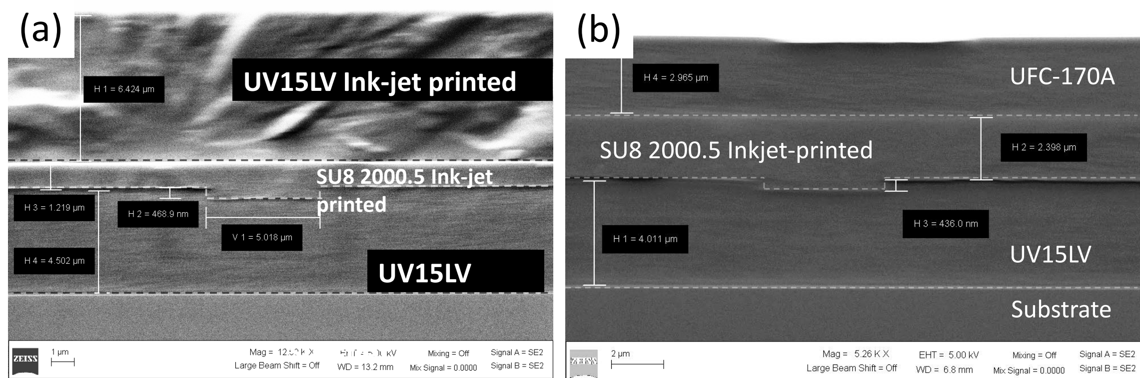

Figure 4-5 SEM cross-section view of printed layers in the device, (a) with ink-jet printed UV15LV as top cladding (b) with coated UFC-170A as top cladding

(4) Electrode deposition

After curing the top cladding layer, standard image reversal and lift-off processes are performed to deposit a gold heating electrode on the top. The heating element covering the junction area at the center is 8 μm wide and 500 μm long. An optical microscopic image of the fabricated device is shown in Figure 4-6(b).

4.3 DEVICE CHARACTERIZATION

The testing is performed with the aid of auto aligner system shown in Figure 4-6 (a). The input light at a wavelength of 1550nm wavelength is launched into one port of the device using a lensed fiber. A DC voltage from a power supply is applied across the heating elements using probes. An ammeter is used to monitor the real-time current, which is required in order to calculate the overall power consumption. To examine the performance of switching behavior at different applied voltages, output light power from two output channels of the device, as well as the current reading on the ammeter are recorded. Figure 4-6 (c) shows the normalized optical output power versus the electrical power consumption. It takes around 100mW power for the cross port to reach its maximum output.

Response speed is another important parameter for a switch. A function generator is used to generate a square wave signal at different frequencies and applied across the heating electrode. The optical response at each frequency is measured using an oscilloscope is shown in Figure 4-7. It can clearly be seen from the figure that device operates up to a frequency of 1 kHz. We also measured the rising/falling time of the device to be 0.46ms/0.40ms. The rising time for bar port and falling time for cross port are relatively longer because they correspond to the OFF state of the applied signal, wherein the junction needs more time to dissipate the heat, compared to the time needed to heat up the polymer.

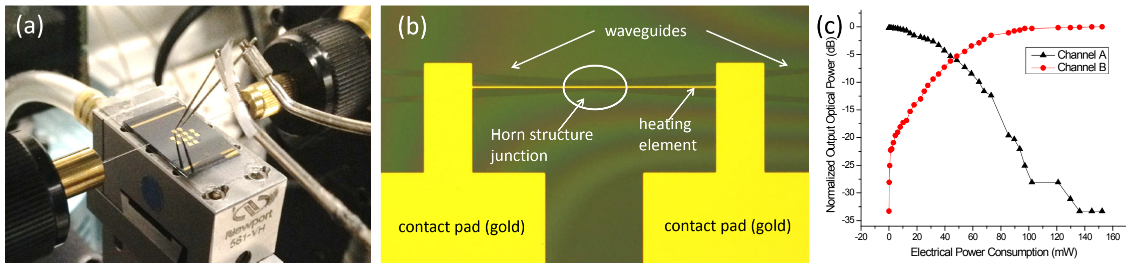

Figure 4-6 (a) testing setup: auto-aligner and probe station with TO switch sample mounted (b) microscopic picture showing the top view of a fabricated 2x2 thermo-optic polymer switch. (c) normalized optical output power versus electrical power consumption from both bar port and cross port.

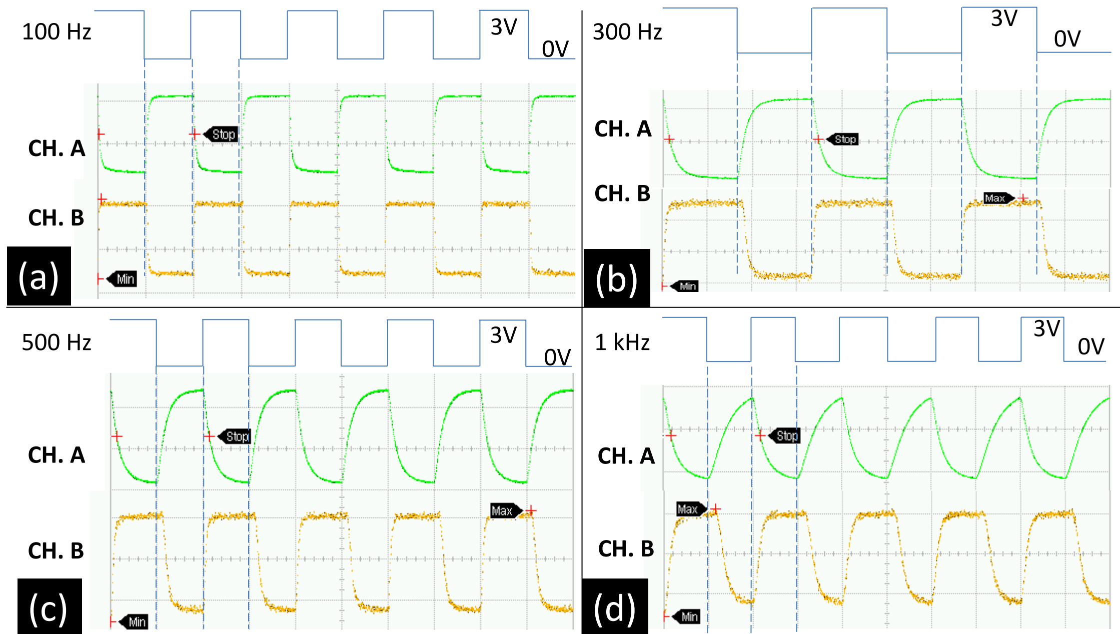

Figure 4-7 optical response with square wave function applied across the heating electrode, at selected frequencies of (a) 100Hz, (b) 300Hz, (c) 500Hz, and (d) 1 kHz. The device can operate at 1 kHz with decent performance.

4.4 Chapter conclusion

Utilizing the precise structural patterning capabilities of imprinting method, and integrating precise material placement advantages offered by ink-jet printing technique in

the process flow, we demonstrated the fabrication of a 2x2 thermo-optic (TO) switch, and experimentally demonstrated its operation up to 1 kHz, with less than 0.5ms switching time. To our knowledge, this is the first demonstration of a printable photonic device. The R2R compatible ink-jet printing process, together with R2R imprinting method, provides great potential solution for the development of flexible and low cost integrated photonic devices with high yield.

Chapter 5: Printable Electro-Optic (EO) Polymer Modulator

With the success in demonstrating Thermo-optic switch, in this chapter, we continue to demonstrate another device -- Electro-Optic (EO) Polymer Modulator. Traditionally, the fabrication process of the EO polymer modulator is complicated, involving several steps [108]. The multilayer patterning requires several lithography, deposition and lift-off processes, which increases the risk of device failure and lowers the overall yield. Our target is to design and fabricate an EO polymer based Mach-Zehnder (MZ) modulator utilizing advanced ultraviolet (UV) imprinting and aligned ink-jet printing technologies for patterning and layer deposition. Different from previously described TO switch, EO modulator requires registration of electrodes to waveguides, thus aligned printing should be utilized. To be specific, the bottom electrode layer is designed and directly ink-jet printed on the substrate to form the patterned layer. The waveguide structure is formed into a bottom cladding polymer using a transparent flexible mold based UV imprinting method. All other layers can be ink-jet printed. The top electrode is carefully aligned and printed over the Mach-Zehnder arm. The modulator demonstrates a V_π of 8V at 3 kHz. This technology shows great potential in minimizing the fabrication complexity and roll-to-roll compatibility for manufacturing low cost, light-weight, and conformal modulators at high throughput.

5.1 Designing printable electro-optic polymer based M-Z modulator

An EO modulator is capable of encoding electronic signal on an optical carrier. The simplest kind of EO modulator uses a crystal such as Lithium Niobate [109], whose refractive index changes with an applied electric field. High performance modulator with 2.5ns switching time based on CMOS-compatible technology of hydrogenated amorphous silicon (a-Si:H) has been demonstrated[110]. Compared to above mentioned

EO modulators, EO polymer based modulators are capable of even faster EO response[111] and negligible velocity mismatch between the optical and RF waves due to non-dispersive dielectric constant [112].

A schematic drawing of the Mach-Zehnder modulator is shown in Figure 5-1. In our structure, we use an inverted rib waveguide structure to form the core. In the MZ modulator configuration, when a voltage is applied on one of modulating arms, the refractive index change in the EO polymer in that arm is governed by the equation:

$$\Delta n=(-1/2)\cdot\gamma_{33}\cdot n^3\cdot(V/d)$$

and the phase difference between two arms is given by

$$\phi=(2\pi/\lambda)\cdot\Delta n\cdot L,$$

where

γ_{33}: the EO coefficient of the EO polymer,

n: the refractive index of the EO polymer,

V: the voltage applied across the driving electrode and ground electrode,

D: the separation between ground and top electrodes

L: the modulation length.

For our structure, the EO polymer (AJ-CKL1) has $\gamma_{33}=80pm/V$ and $n=1.63$. The electrode separation and arm length are designed to be $d=8.3\mu m$ and $L=7.1mm$, respectively. The theoretical value of the half-wave switching voltage is calculated to be

$$V_\pi= (\lambda\cdot d)/(L\cdot \gamma_{33}\cdot n^3)=5.23V.$$

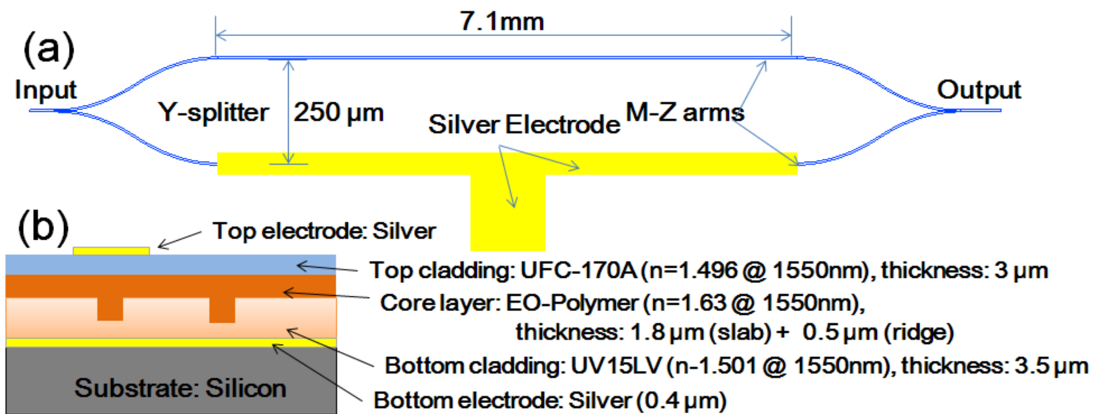

Figure 5-1 (a) schematic top view showing the modulator structure, (b) schematic cross section showing the different materials comprising the EO polymer modulator

Similar to TO switch, in order to enable device development, the material system choice should meet certain criteria: 1) all the materials should satisfy the optical index requirements to form a waveguide, 2) the bottom cladding layer should be imprintable, 3) the core layer should have sufficient EO coefficient so that a suitable change in the index is achieved within a small applied E-field, and 4) the core material should have suitable viscosity to be ink-jet printed. In order to satisfy the physical and optical characteristics, we selected UV15LV (n=1.501@1.55µm) from MasterBond as the bottom cladding layer, EO polymer (AJ-CKL1, n=1.63@1.55µm) as the core layer and UFC-170A (n=1.496@1.55µm) from URAY Co. Ltd as top cladding layer. The choice of cladding materials is mainly based on the compatibility considerations of the EO polymer. UV15LV is UV curable, solvent-free and also ink-jet printable. Thus, it is a good candidate for roll-to-roll system. For the electrode layers, commercially available silver nanoparticle ink from Cabot Corp. was chosen. It is optimized in viscosity and surface tension, to meet the requirement of Dimatix material printer.

5.2 Fabrication Process

(1) Mold fabrication

The fabrication starts with silicon mold and SSQ mold fabrication. The quality of molds is one of the determining issues for device performance. For EO modulator, the fabrication processes for hard mold and SSQ soft mold are exactly same as those described in Figure 4-3 for TO switch. The imprinting process is performed by Dr. L. Jay Guo's group at University of Michigan. The SEM pictures for the molds are shown in Figure 5-2 (a). The feature step height for the Silsesquioxane (SSQ) mold duplicated from silicon hard mold is 0.5μm which equals the ridge height of the waveguide.

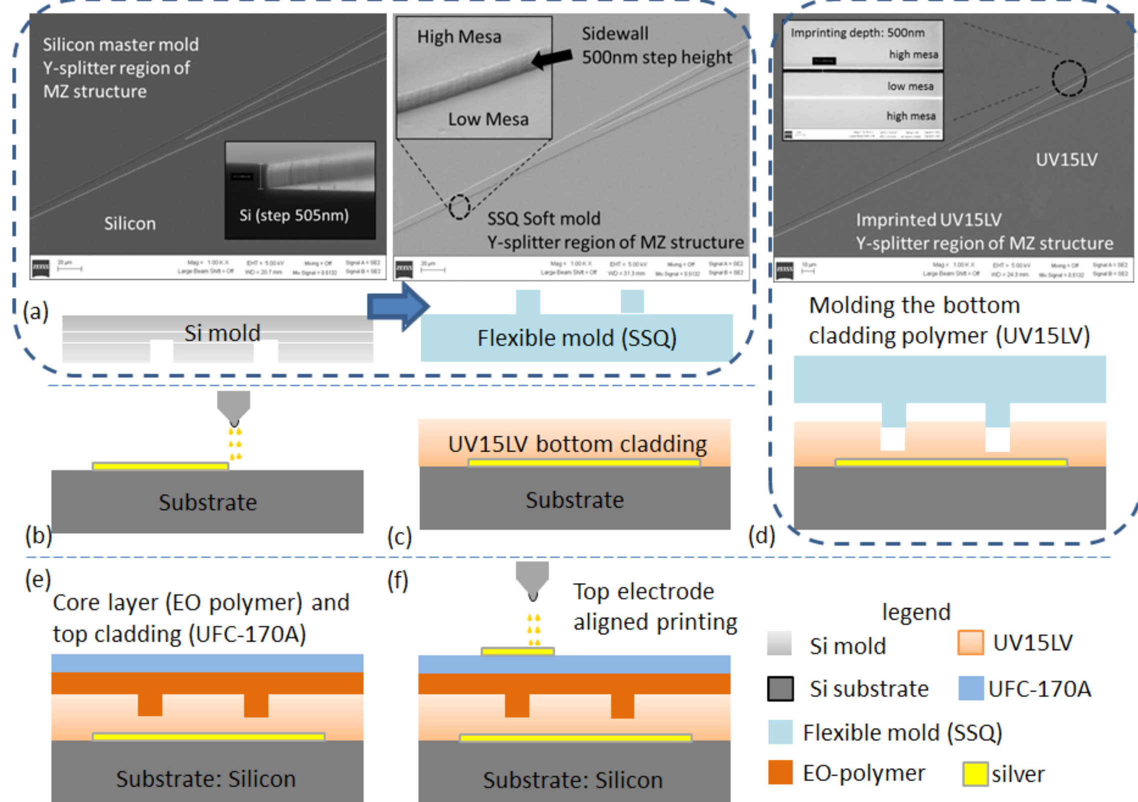

Figure 5-2 main process flow for fabricating an EO polymer modulator using imprinting and ink-jet printing method. (a) silicon and SSQ mold, (b) bottom electrode deposition, (c) bottom cladding layer deposition, (d) imprinting, (e) core layer and top cladding layer deposition, (f) top electrode deposition

(2) Bottom electrode ink-jet printing

A 350~400nm bottom silver electrode layer along with alignment marks is ink-jet printed onto the silicon substrate, as shown in Figure 5-2 (b) and Figure 5-3 (a). If making flexible devices, the silver can also be printed on flexible substrate such as Kapton film, as shown in Figure 5-3(b). Since this is the bottom electrode pattern, it does not need to be precisely aligned. But in order to align all the following layers, several alignment mark are printed together with electrode patterns.

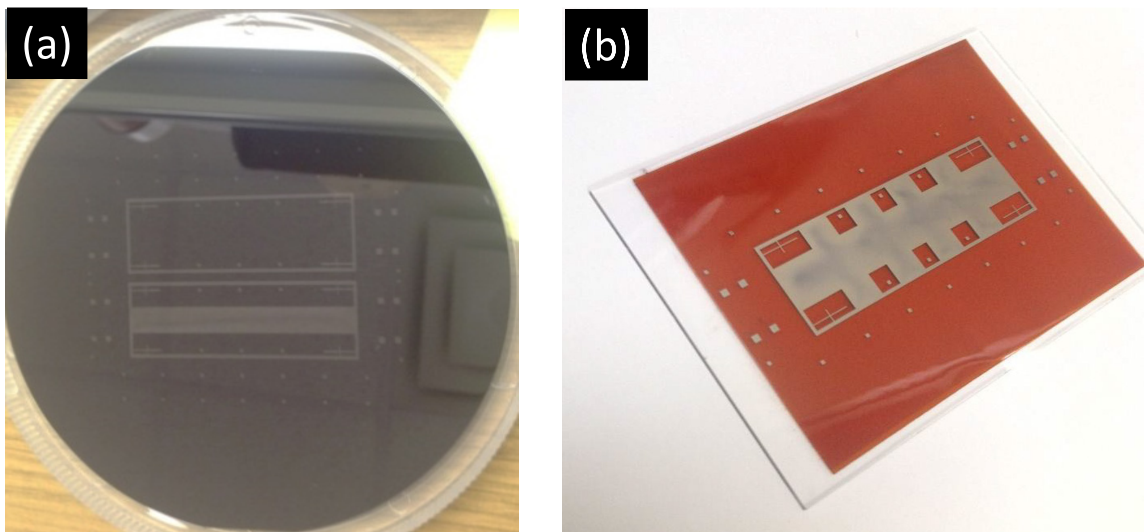

Figure 5-3 (a) ink-jet printed silver layer as bottom electrode, on silicon substrate (b) ink-jet printed silver layer as bottom electrode, on Kapton film

(3) Waveguide forming using imprinting

UV15LV is deposited to form bottom cladding layer, as shown in Figure 5-2 (c). Next, the SSQ mold containing the MZ structure is brought into conformal contact with the bottom cladding layer, followed by UV imprinting and de-molding process, as shown in Figure 5-2 (d). The EO polymer is then coated, followed by top cladding UFC-170A deposition, to form a rib waveguide structure, as shown in Figure 5-2 (e).

(4) Top electrode ink-jet printing

After finishing the waveguide, a top silver electrode is ink-jet printed on top of the top cladding layer. Noted that ink-jet printing is a key step to ensure device operation since it needs to be aligned to one MZ arm but not spreading to the other. Therefore, from the bottom electrode design point of view, the separation between two arms is set large enough to compensate for ink reflow. From the fabrication point of view, the top cladding is treated with oxygen plasma before ink-jet printing to ensure good contact. This is beneficial for both poling and driving processes. The ink-jet printed results are shown in Figure 5-4 where we can see silver layer covers one of the MZ arms with smooth edge. Compared to metal with rough edge deposited using lift-off process, the ink-jet printed electrode can reduce the change of poling breakdown due to "rounded" edge. The thickness of the electrode is around 400nm and it will serve as both poling and driving electrodes.

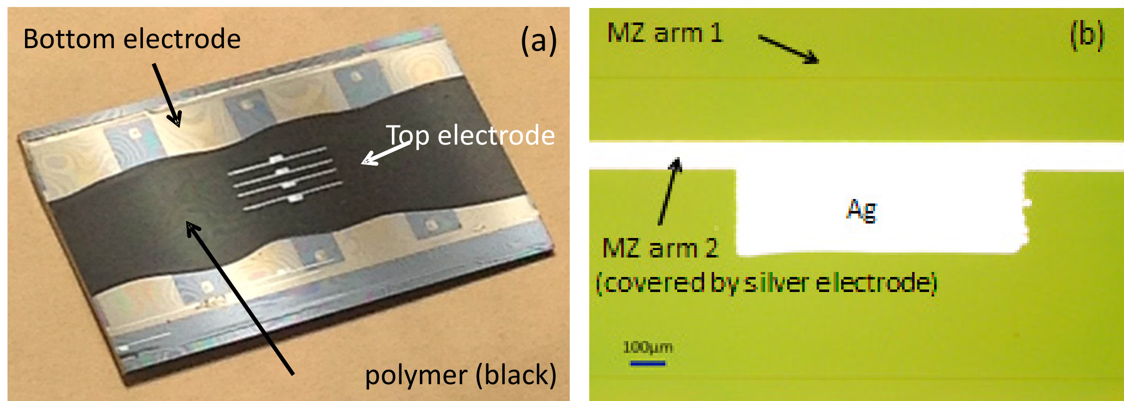

Figure 5-4 (a) EO polymer modulator with ink-jet printed electrode. (b) zoom-in view of the silver electrode showing smooth surface

(5) Device poling

In an as-prepared thin film of EO polymer, the chromophores are randomly oriented and hence the EO polymers are naturally centrosymmetric after the preparation

of thin films. In order to induce a macroscopic second-order nonlinearity, thin films must be rendered noncentrosymmetric. This is usually done by a process called thermally assisted electric field poling. The process is illustrated in Figure 5-5. At elevated temperature slightly above the glass transition temperature, the polymer chains become weak and the chromophores will have some freedom to move. Since the chromophores have a permanent dipole moment, they will be aligned to externally applied electric field. Once cooled down quickly, the positions of the aligned chromohores can be locked.

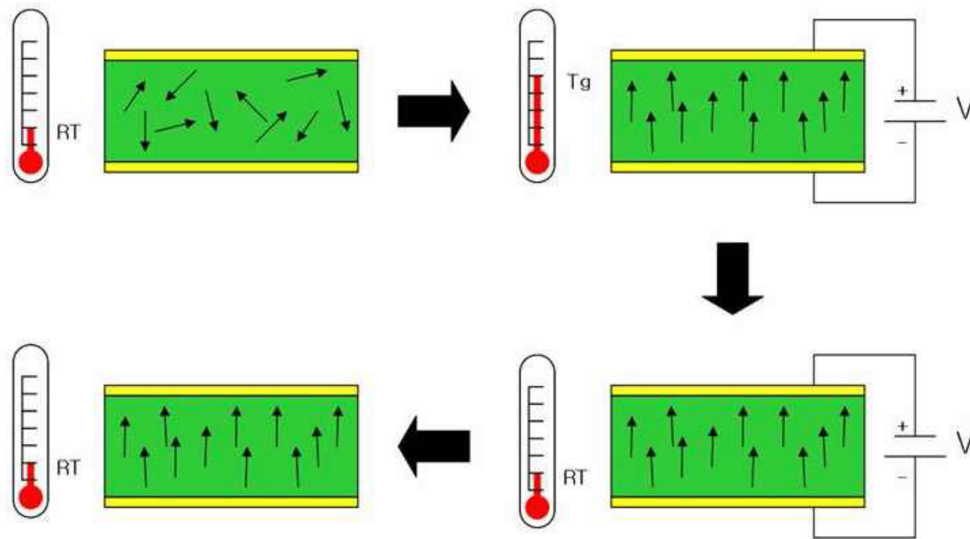

Figure 5-5 schematic illustration of thermally assisted electric field poling process

The poling setup is shown in Figure 5-6 (a). The value of γ_{33} of an EO polymer film is determined by the poling efficiency. Poling electric field of about 80V/μm (650V over 8μm separation between top and bottom electrodes) is applied vertically across the polymer waveguide. During the poling process, the temperature is controlled to increase from room temperature to peak poling temperature of 140°C, which is 5°C above the T_g of AJ-CKL1, and then quickly decrease back to room temperature. Throughout the entire poling process, the leakage current is monitored by a picoammeter. A current-limiting

resistor and two back-to-back diodes are used in the circuit connection to protect the picoammeter from being damaged by any unexpected breakdown-induced high current. Figure 5-6 (b) shows a leakage current curve depending on the controlled temperature during the poling time. The poling electrode area is Electro area is ~600,000μm^2, the Current density is 0.4~0.5μA/m^2 when the peak current is 0.25μA.

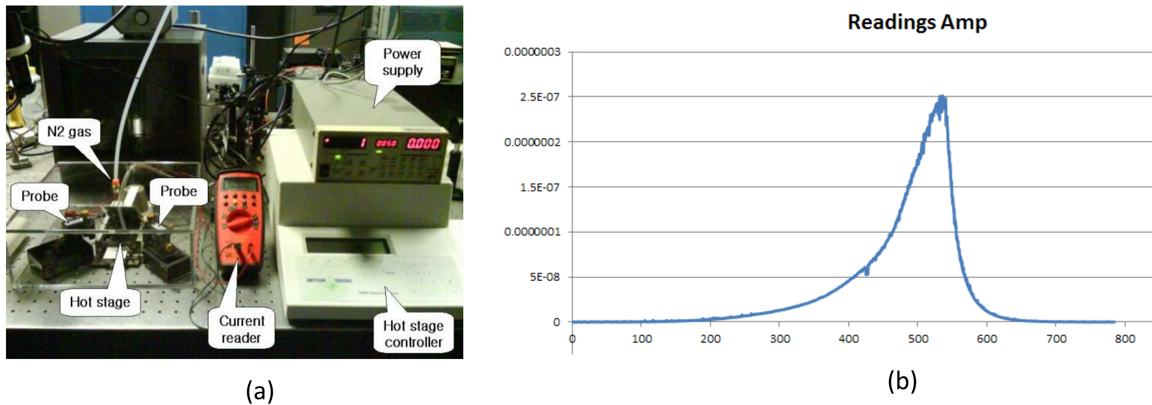

Figure 5-6 (a) poling setup (b) poling profile showing leakage current with poling time. The peak is reached when the temperature reaches 140 ^{o}C

5.3 Device characterization

(1) SEM cross-section picture

Before actual testing, we have carefully examined the cross-section of the EO modulator, to make sure that all layers are stacked properly. The SEM cross-section image is shown in Figure 5-7. As can be seem, the top silver electrode covers the rib waveguide region perfectly and EO polymer.

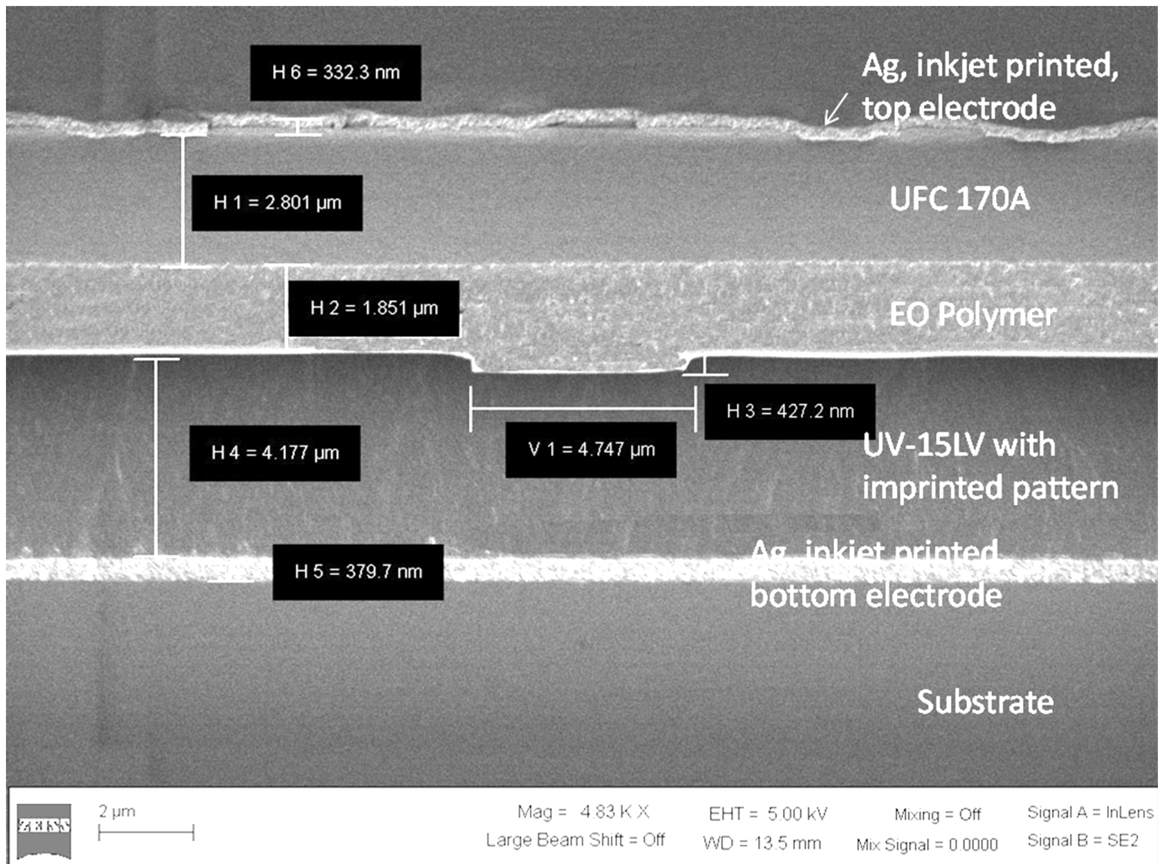

Figure 5-7 cross-section view of printed EO modulator

(2) Modulation test – signal response

Testing environment: the sample is mounted on an auto aligner for precise light coupling. TM-polarized light with 1.55μm wavelength from a tunable laser is launched into the input waveguide via a polarization maintaining lensed fiber, and the output light is collected by a single mode lensed fiber, as shown in Figure 5-8 (a). The measured total insertion loss is around 26dB due to the high propagation loss of EO-polymer and the roughness of the cleaved input and output facets. Driving signal is applied across the driving and ground electrodes of the device, and the modulated optical signal is then collected by a photo detector connected to an oscilloscope, as shown in Figure 5-8 (b).

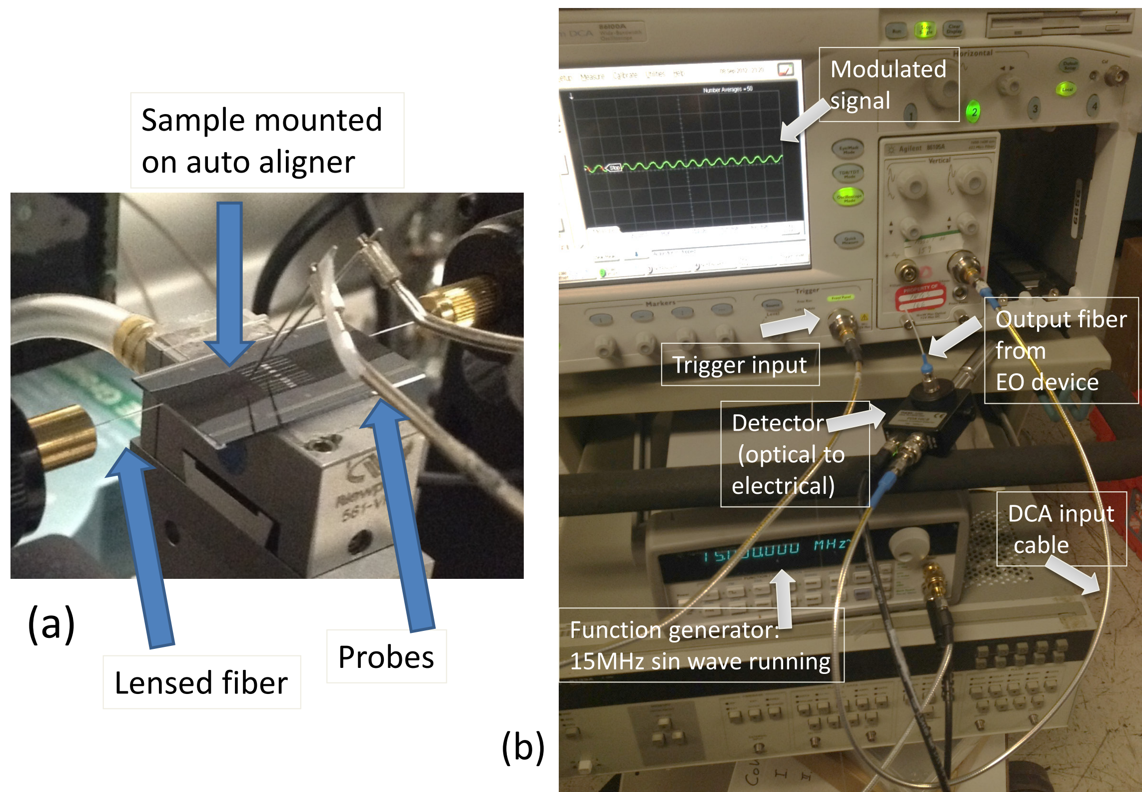

Figure 5-8 (a) EO modulator sample testing on auto-aligner (b) other equipment for signal generation and collection

Figure 5-9 (a) and (b) show the input and output when a 100 kHz triangle wave signal is applied. Figure 5-9 (c) and (d) show the input and the modulator response, respectively, to a 15MHz sinusoidal signal. Due to the utilization of lumped electrode structure which is not specially designed for high speed purpose, the signal quality at higher speed was poor. By utilizing traveling wave electrodes, the operating speed of the device can be further increased [113].

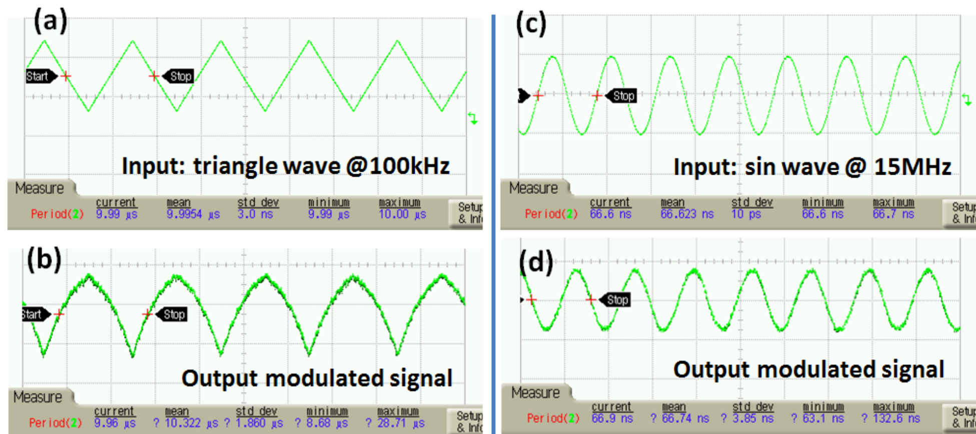

Figure 5-9 (a-b) 100 kHz triangle wave input and corresponding modulator output signal; (c-d) 15 MHz sinusoidal wave input and corresponding modulator output

(3) Modulation test – modulation depth vs. frequency

The modulation depth is defined as $M\%=(I_{max}-I_{min})/(I_{max})$, where I is the light intensity. In our experiment, it is translated into voltage signal at the photo detector. We measured the response at different frequencies and calculated the M% at 5V DC, as shown in Table 5-1. Utilization of travelling wave electrode instead of lumped electrode will help increasing device bandwidth and improving the high speed performance.

Table 5-1 modulation depth at different frequencies

Frequency (Hz)	100 K	1M	10M	15M	1G
M% (5V DC)	16.7%	16.0%	12.5%	8.0%	1.54%

(4) Modulation test – modulation depth vs. bias voltage

We have measured the modulation depth by varying the bias voltage at 10MHz, and the results are shown in Figure 5-10. Since the V_π is expected to be over 10 volts at 10MHz, no over-modulation is observed.

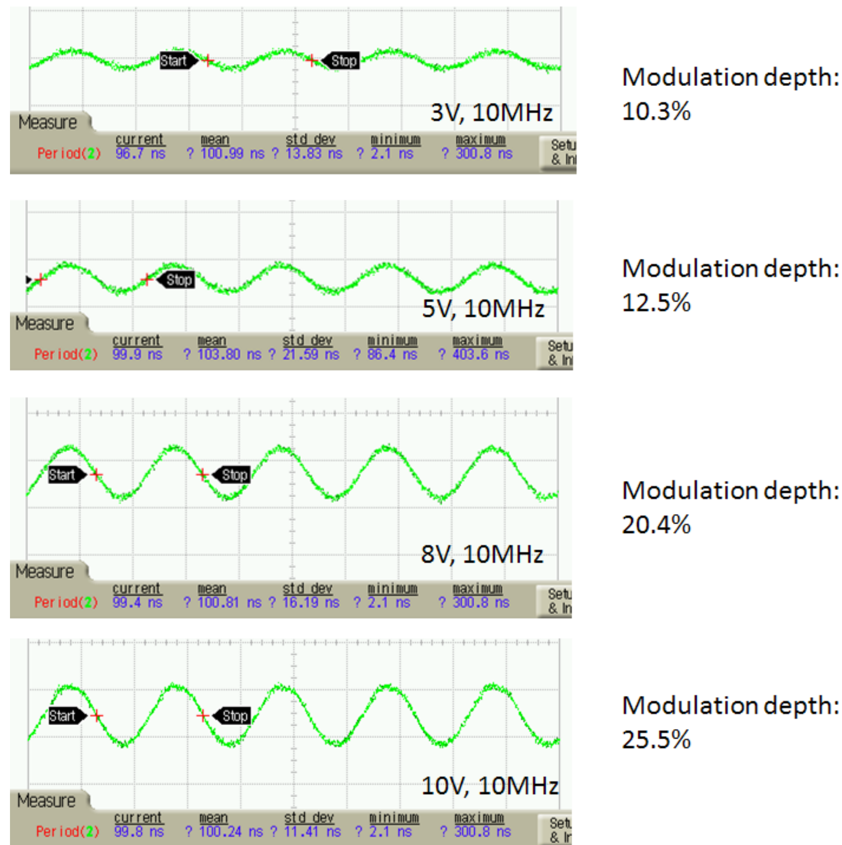

Figure 5-10 modulation depth at different bias voltages at 10MHz

(5) Modulation test – half wave switching voltage

By fine tuning the voltage applied to the point of over modulation, the half-wave switching voltage V_π is measured to be around 8.0V at 3 kHz, which yields the V_π•L=5.68V•cm. It is higher than the calculated value probably due to the low poling efficiency of the EO polymer, which reduces the in-device γ_{33} value to *52.3pm/V*. Applying higher poling voltage may increase the risk of device break down. Other reported V_π•L values from similar structures are around 3.6V•cm[114], 1.995V•cm[114], 1.8V•cm[111] and 16.8V•cm[115]. In [114]& [111], the EO polymer they utilized intrinsically has a larger γ_{33} (*>130pm/V*) than ours (80*pm/V*). Therefore, we are confident that our presented device has reasonable testing results and competitive performance

compared to other research group's work, while additionally we are employing a low cost, roll-to-roll compatible process. Furthermore, to the best of our knowledge, this is the first demonstration of a printed modulator.

5.4 Chapter conclusion

In this chapter, we explicitly demonstrated a novel fabrication technology for polymer based EO modulators, taking advantage of UV imprinting to define waveguide patterns and ink-jet printing to deposit electrodes. Note that, we have also tested the ink-jet printability of other layers, although standard spin coating process is used in this demonstration to simplify feasibility study. Therefore, our roll-to-roll compatible printing processes will simplify the fabrication process and enable high speed, low cost device fabrication. Especially from material consumption point of view, ink-jet printing only deposits material at the desired region, thus minimizing both material consumption and wastage, compared with spin coating method. Also, it is featured by aligned printing, which reduces the complicated steps of lithography and lift-off. Furthermore, from system integration point of view, this method gives the flexibility of integrating several materials or printed components on a single platform, without increasing process complexities. Modulation at 3 kHz triangle signal is demonstrated, with V_{π} of 8V. Since both the imprinting and ink-jet printing method are roll-to-roll compatible, our technology provides a practical way for fabricating low cost flexible optical devices with high throughput.

Chapter 6: Roll-To-Roll (R2R) Printing System Integration

6.1 Introduction, opportunity and innovation for R2R printing

As mentioned in Chapter 1, printed electronics industry has been undergoing a significant growth in the market since early 21st century. The main applications include RFID[38, 39], solar cell[43, 44], display[41, 42] where device structures are mainly formed by stacking patterned layers and the critical dimension is on the order of tens of microns to millimeter range. Similar to other layer stacking devices, registration between layers is of great importance to determine the quality of the device. For a tabletop printer, such as Dimatix 2800 series printer, the layer to layer registration is achieved by a microscopic system. That system determines the printing origin and both the X and the Y direction offset values with respect to the underlying layers. Therefore, one can precisely alignment two patterns with the maximum offset of the mechanical moving part accuracy, or to be more specific, the step motor accuracy.

However, the alignment strategy for a table-top printer is not applicable for a roll-to-roll system where the registration needs to be performed while the substrate is moving at high-rate. There are several technologies that are used to realize roll-to-roll registration. For example, Krebs etc.[116] punched a series of registry holes along the edge of the web so that the position of the web is kept the same with respect to the printhead. Jung etc. [38] utilize no external setup for registry but use an advanced mechanical system capable of providing overlay printing registration accuracy limit of ±20 μm. Although it is a practical solution to make use of precise tracking mechanism and edge sensor to ensure minimum sideways wander of the web, using such "passive" alignment strategies may still encounter some off-registration problems if the original web has poor edge condition (e.g. edge flatness) that affects the width of the substrate. Therefore, in this research, we implement an "active" alignment strategy using machine

vision and demonstrate the entire system setup, including the software and hardware that realize the multi-layer alignment. The main features of the presented technologies are that the active alignment can be tolerant to the imperfect substrate conditions and does not post demanding requirement on the web tracking system.

Chapter organization: First, we will introduce the basic idea for realizing roll-to-roll registration. Based on this idea, the main system modules are determined. Next, based on the detailed system requirement, we specify each component in every module. The detailed alignment strategies are also given since it is the key factor that affects the hardware selection and software algorithm. A customized software implementation is described and it enables synchronization among all the components. Finally, multi-layer printing test is performed and the results are analyzed.

6.2 SYSTEM COMPONENTS FOR SINGLE-LAYER AND MULTI-LAYER PRINTING

(1) Basic idea

The Roll-to-Roll ink-jet printing system with alignment capability is a complex electrical-mechanical system. In order to realize high-speed, multi-layer printing system with good registration, an active alignment method should be considered. Alignment marks are utilized as the reference position and all layer patterns should be placed according to this reference position. Therefore, as long as we align the alignment marks, all other patterns should be aligned. Different from Dimatix printer described in the previous chapters for making TO switch and EO modulator, the printhead in the roll-to-roll system is stationary which means that the alignment marks printed on 1st layer will not always be continuously exposed to the same range of nozzles for the 2nd layer printing from copy to copy because web sideways wander exists. So, the solution is to utilize a high speed imaging system to get the real-time alignment mark position and

adjust the printer nozzle actuation accordingly for each copy of the pattern. Besides, the system should also be configured to provide correct timing to start the 2nd layer printing by using a Print/Go device.

(2) Main system modules

Based on these basic ideas, we determined the main modules for a single stage: pattern detection module, material ink-jet printing module and fast curing module. To complete web transfer and printing function, some other modules including substrate moving module (web tracker, encoder), controlling module (desktop with controlling software) are needed. A cartoon briefly depicting all the components in the single stage is shown in Figure 6-1.

Figure 6-1 schematic drawing of the main components in the roll-to-roll printing system with active alignment function. The main modules are 1) substrate moving module; 2) pattern detection module; 3) material ink-jet printing module; 4) fast curing module and 5) system controlling module. Modules (2) (3) and (4) form a standalone single stage for aligned-printing and can be configured in series to realized multi-stage printing.

The main functions of these modules are described below:

- The substrate moving module: delivers the web at controlled speed.
- The pattern detection module: captures the alignment marks and the Print/Go marks' positions.
- The material ink-jet printing module: retrieves and prints patterns with the desired material.
- The curing system: provides in-line fast curing of the ink.
- The system controlling module: processes images from the image acquisition module and controls the ink-jet printing module.

Each individual component that builds up this system will be discussed in detail in the following section.

(3) Web tracking module

The tracking system is an Arpeco Tracker with edge detection sensor, as shown in Figure 6-2 (a). The sensor detects the substrate edge and controls the tilting angle of a suspending shaft so that the web edge can be aligned in real time to minimize the lateral direction (Y) offset and minimize web sideways wander. The rewinding shaft runs slightly faster than the unwinding shaft to apply tensile stress on the web so that the web tightens. The web speed is adjustable and in this particular research work, it is set to about 5 meters/minute. It should be noted that, similar to most tracking system in the market, the system can only run in one direction from the un-winding shaft to re-winding shaft. Although the edge detection sensor and the actuator system can ensure rough alignment of the web edge, the sideways wander is still inevitable. Besides, due to the fact that the width variation of the web is large, which is common for Kapton tape roll, the edge detection itself will not be sufficient to give satisfying registration results. In the

current situation, the sideway wander is estimated to be around 2mm in each direction (4mm total). The maximum sideway wander will determine the minimum required camera field of view (FOV). Generally speaking, using smaller FOV will increase the physical resolution of the captured images. But it requires the tracker to have less sideways wander so that all the alignment marks can be captured.

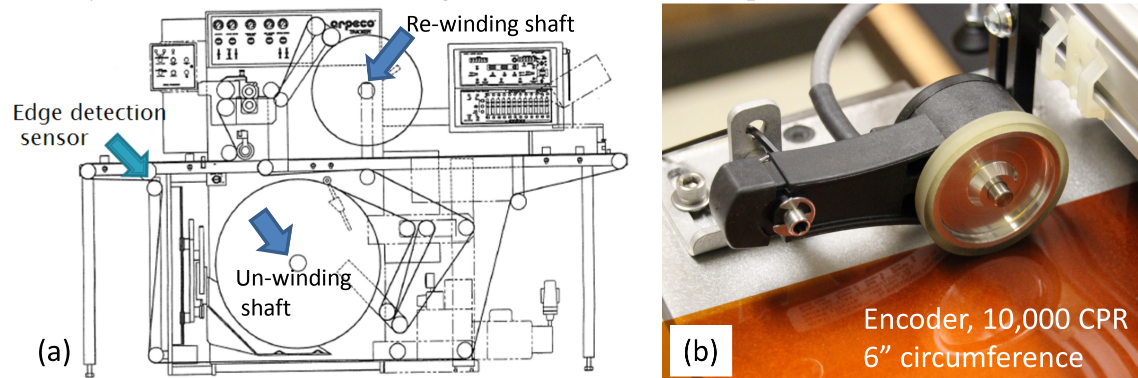

Figure 6-2 (a) schematic of Arpeco web tracker tool (from product's manual); (b) TR1 wheel encoder

The other components in the web tracking module is the encoder wheel (model #: TR1-U1 R4 - 10000 N V1Q OD- K00) as shown in Figure 6-2(b). The length of circumference is 6-inches and it outputs 10,000 counts per revolution (CPR), which gives the resolution of 15µm per pulse. The spring-loaded torsion arm makes sure that the wheel is in good contact with the substrate. The purpose of this encoder is to feedback the real time web running speed for the ink-jet printing module to make sure the printed pattern has the right aspect ratio.

(4) Pattern detection module

The purpose of the pattern detection module is to capture the alignment marks and the Print/Go marks on the running web. Choosing an appropriate camera and optical lens will ensure good image acquisition results.

There are basically two types of cameras, area-scan camera and line-scan camera. For area array sensors, two-dimensional arrays of pixels in varying resolutions are available (e.g. 640 horizontal × 480 vertical, 1024×1024 and 1600×1200). Consumer digital cameras use these types of sensors. They excel in imaging still or slow-moving objects. But using area arrays to image high-speed motion of objects or continuous webs is problematic, because in order to "stop the action", area arrays need short exposure times as well as shuttering, synchronization equipment, or powerful, strobe illumination, all of which add to system complexity and usually make it harder and more expensive to get good images. Additionally, the area scan camera has relatively longer "readout" (time between two exposures) during which it is "blind" and cannot take images. This will be a severe problem for high-rate printing of active and passive components because the object may pass the FOV without being captured.

In contrast, line-scan sensors lend themselves well to imaging high-speed objects or webs. With a single line of pixels, line-scan sensors build continuous images not limited in their vertical resolution. Vertical resolution comes from the object's own motion. Instead of 1024×1024, they can produce 1024×N, where N keeps growing as long as the camera is running, like the scanning process of a facsimile machine. The principle of capturing images from a line-scan camera is that it requires a moving subject instead of a still object. It would be more suitable to utilize a line-scan camera in our web registration application.

There are other parameters that need to be set before we can determine the line-scan camera resolution. First, the target resolution is set to around 3-4μm/pixel in lateral direction (Y direction). This value is sufficient for most of the printed device requirements, and will not become the bottleneck even for future upgrade. The FOV can be adjusted by the zoom-in ratio of optical lens. In the following description, FOV is set

to be 6mm as shown in Figure 6-3, according to the alignment mark size of 2mm and web tracking module's sideways wander of 3-4mm. Then, the number of pixels needed (n) to cover 6mm FOV should be at least 6mm/(3μm/pixel)=2000.

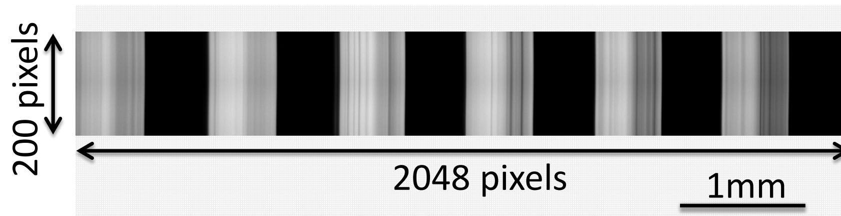

Figure 6-3 field of view (FOV) of the line-scan camera showing 2048 by 200 pixels; calibration pattern of 6mm is used.

After careful consideration, we choose a line-scan camera P2-2x-02K40 from Dalsa, a Navitar Zoom 6000 optical system with coaxial illumination to build our image acquisition setup. Navitar Zoom 6000 optical system is featured by an adjustable zoom that helps in better tuning the FOV. Coaxial illumination provides higher sensitivity when shining on reflective surfaces, thus it is a suitable choice for detecting patterns formed by a uniform thick film, e.g. silver film. Halogen bulb is used as light source since it provides high intensity light which guarantees image quality even with reduced exposure time. The line-scan camera has n=2048 pixels and the optical zoom-in lens is adjusted to set the FOV to be 6mm, which yields the camera system resolution to be 3μm/pixel. There is still room for increasing the image resolution by reducing the FOV and/or increasing the line-scan camera pixels. However, the sideways wander of the mechanical conveying system needs to be minimized to 1-2mm before one can safely reduce the FOV. Besides, the trade-off of increasing the number of camera pixels is the increasing data volume for image processing.

The Print/Go signal is generated by a photoelectric sensor. The signal is used to trigger the actuation of the printhead. The sensor we use is commercially available from

Banner (QS12VN6CV10, NPN, sinking) and it is connected to the "Product Detect" pin in the Print Manage Board (PMB-C2) which will be described in the material ink-jet printing module. When a Print/Go mark is detected, the sensor output will be drawn down to ground creating a falling edge of a TTL signal, which triggers the printing. As shown in Figure 6-4, the alignment mark will first enter the FOV for determining the Y offset. Then after a certain time, the photoelectric sensor will see the Print/Go mark to start the printing.

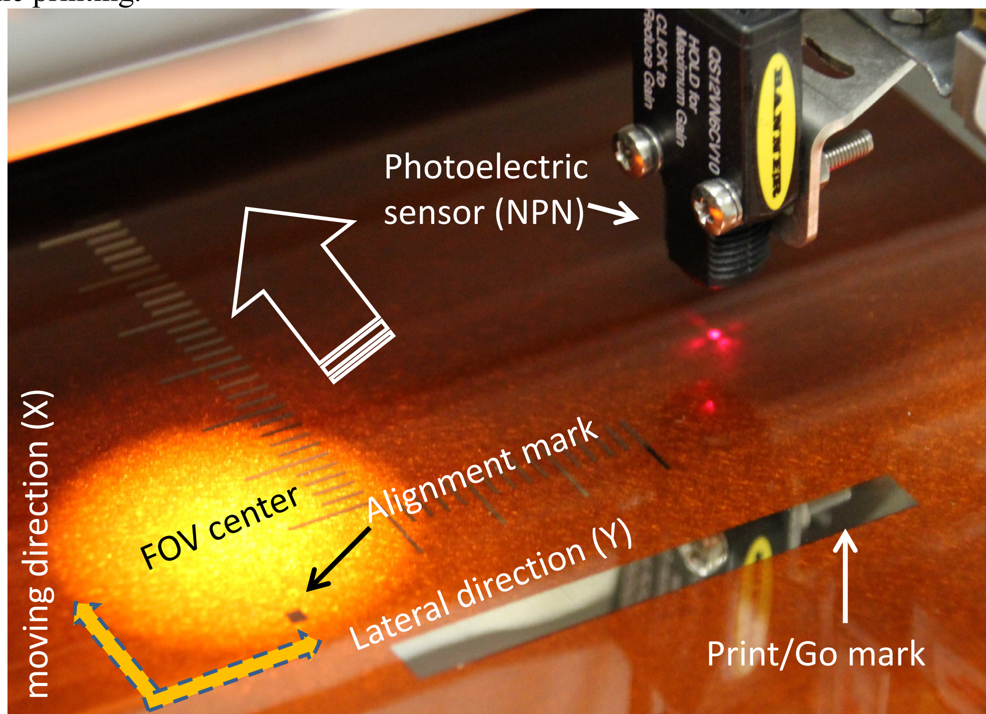

Figure 6-4 alignment mark detection using line-scan camera and Print/Go mark detection using photoelectric sensor.

(5) Material ink-jet printing module

The ink-jet printing cartridge (KM1024MH) used in the current program is commercially available from Konica Minolta Technologies, Inc. The specifications are given in Table 6-1. The piezo actuator walls with electrodes can move by applying an

electric field across them. The applied waveform is called DRR which stands for DRAW, RELEASE and REINFORCEMENT cycles.

Table 6-1 specifications for KM1024MH printhead from Konica Minolta (source: http://www.industrialij.com/pages/KM1024.html)

Technology	3 cycle on demand piezo electric drive
Nozzles	1024 (512 x 2 lines)
Channel Resolution	70.5µm pitch (360 dpi: 141µm pitch x 2 lines)
Native resolution	360 dpi
Drop size	M (14pL)
Max Frequency	13.2 kHz
Printing Width	72 mm
Drop Velocity	6.0 +/- 0.5m / sec
Binary print	available
Grey-scale	between 1 and 7 drops per pixel (3 bit data)
Heater	integral electrical heater and thermistor
Dimensions	85 x 67 x 20mm (including mount wing 40mm)
Weight	<150gm

The actuation of the cartridge is controlled by “Print Manager Board” (PMB) which acts as interface of PC and cartridge. The software that controls the PMB is called “Print Server”. It accepts external synchronizing signals from encoder and route the TCP/IP commands to the nozzle head. Also, it provides the option for waveform settings so that the jetting speed, jetting volume and the transfer mechanism can be specified. In our system, the jetting speed is 6m/s and the jetting volume is 14pL for each drop.

Besides, the Print Server also has a rendering module which converts the CAD files to .bmp image files (ripped files) that are recognizable by the printhead.

(6) Xenon fast curing system

For the current roll-to-roll printing system, it is crucial to cure the printed ink quickly before it enters the next module or touches the rods. For inks and coatings containing nanoparticles, this process is called sintering. A conventional sintering process requires heat above 150°C. However, it limits the applicable substrate, especially when the metal has a higher melting point than the flexible substrate, making it impossible to achieve sintering without subsequent damage to the substrate. Besides that, the curing speed of conventional systems is also relatively low to heat the ink above its melting points. To overcome these problems, novel way of curing/sintering using high energy light pulse has been implemented. The basic theory of how light curing helps sintering down the nanoparticles and detailed lamp information is attached in Appendix A.

In the current research, we utilize Sinteron 2000-S system from XENON Corp. as the photonic sintering tool. The lamp housing model is LH-910 as shown in Figure 6-5 (a) and the electronics rack is shown in Figure 6-5 (b.) The LH-910 housing dimensions are 9.51" × 7.9" × 5.9" (L × W × H). It contains a 4.2" diameter spiral lamp. The spiral lamp system is an area light source without a focus. The maximum energy occurs between 0.5" and 1" from the bottom of the window, and at the center of the lamp. Air cooling is used for cooling the lamp while operating. The light curing system is integrated with single stage ink-jet printer, and the relationship among the pulse needed, pulse forming network (PFN) structure, energy delivered are calibrated to make sure that the printed silver ink can be successfully cured, as shown in Table 6-2. When the web speed is 5meters/min, it will be exposed under the lamp for 1.5s receiving 3 pulses.

Figure 6-5 Sinteron 2000-S flash lamp sintering system (a) LH-910 lamp house with spiral lamp; (b) electronics rack (source: http://www.xenoncorp.com)

Table 6-2 curing results under various conditions

	PFN1	**PFN1**	**PFN1&2**	**PFN1&2**
Pulse duration (μs)	580	580	1000	1000
Voltage (kV)	3.8	3.8	3.6	3.6
Energy/pulse (Joules)	830	830	1500	1500
# of pulses needed	10	5	3 (at 1 inch)	3 (at 0.5 inch)

(7) System controlling module

The system control module is mainly referred to a PC with required hardware and software to perform the printing task including acquiring images from the camera, processing the images and outputting the commands to the printhead. Besides, it is also a station for designing the patterns and configuring the Printer Server settings. For image

acquisition, the image acquisition board from National Instruments (NI PCIe-1427) is used to connect to the camera output through Camera Link cable.

The printer control is realized by TCP/IP commands. The client application initializes a command which will be received by the server. The server processes that client command and start the print engine operation. Once finished, the engine components will response to the server and the server will feedback the client with related information. For the client TCP/IP application to send out the command and reach the printer, it takes about 2ms. Additional time is needed to load the image from the hard drive (varies based on image size) to complete the cycle.

A typical printing sequence will be:

R,D, image.vpi *#load CAD layout pattern for render*

R,R,Rip_image.bmp, 0 *#render pattern to the format that can be recognized*

P,P,1,Rip_image.bmp,1 *#print the image one copy, one time*

However, when printing multiple images, the printer will initialize each time a new image is loaded, causing significant delay in the print. Therefore, in order to avoid this problem, we activate a more effective "queue print" mode when the printing begins. In the "queue print" mode, the print server will not try to initialize the printer configuration each time when receiving commands but just add new images to the queue continuously and prints them out. Thus, it greatly increases the responding speed of the print server. A sample code is shown below.

P,Q,P *#enter queue print mode*

P,Q,A,Rip_image1.bmp,1 *#print the 1st image*

P,Q,A, Rip_image2.bmp,1 *#print the 2nd image*

P,Q,A, Rip_image3.bmp,1 *#print the 3rd image*

P,Q,E *#exit queue print mode*

6.3 SYSTEM INTEGRATION

With the basic functions realized by each individual module, system integration is realized by applying certain algorithm for aligning multi-layers. The detailed alignment strategy will be discussed in the following sub-sections along with software implementation using NI LabVIEW.

(1) Alignment strategy in Y direction (lateral direction)

The Y direction alignment is realized by the camera image processing. There are two steps involved: (a) determine the alignment mark offset (b) choose the corresponding pre-offset 2nd layer pattern to print.

By setting the correct FOV, one can make sure that whenever an alignment mark starts to pass under the camera, it will appear in the FOV. The next step is to recognize that alignment mark and output its position. There are two methods to detect the alignment mark. The first one is utilizing pattern matching, which compares the captured image with standard alignment mark template on the hard drive, and outputs the position if they match to a certain degree. The second one is utilizing edge detection method as described below, which is more preferable due to its effectiveness.

Edge detection is a set of mathematical methods which aims at identifying points in a digital image at which the image brightness changes sharply or, more formally, has discontinuities. It provides a highly efficient way of detecting the alignment mark. The cartoon shown in Figure 6-6 presents the basic idea of detecting an alignment mark.

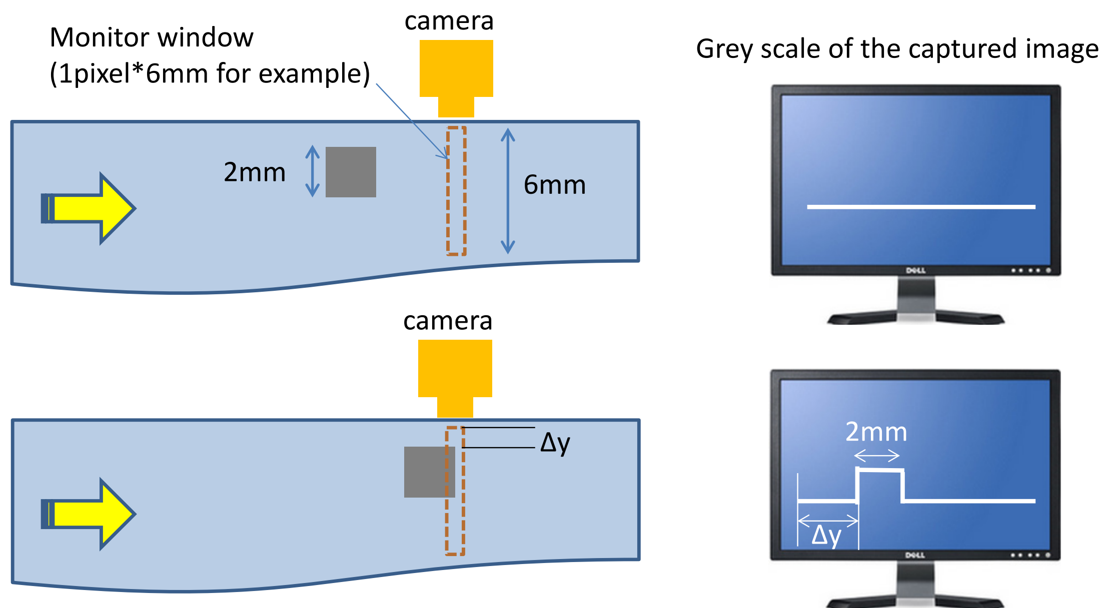

Figure 6-6 edge detection for Y direction alignment

As can be seen, when an alignment mark passes under the camera, the abrupt greyscale change will be captured by the camera and the first and last edge positions will be recorded. It should be noted, as mentioned above, that the line-scan camera has 2048 pixels, thus the direct output from the edge detection program is a value in pixel (0-2047). Here, in our application, we make use of the first edge to represent the position of the alignment mark. The last edge value is also recorded and used for checking the validity of the alignment mark.

The image processing speed should be able to match the image acquisition speed. All image processing applications are based on individual acquired images. When it comes to the case of line-scan camera, each image is formed by combining several line readout results together. For example, an image size of 2048×500 is formed by combining the results of 500 line readouts, with each line readout containing 2048 points. The line rate (number of line readouts per second) should be large enough so that it will

be able to capture the alignment mark without missing any of them. Therefore, the number of images that the system can acquire is determined by “line rate” divided by “image height”. A typical line rate is 20,000, and if we set the image height to be 200, it will generate 100 images per second for processing.

To match the image processing with the image acquisition speed, the image processing step should be efficient. According to our performance comparison, a single line edge detection step takes around 0.2ms, while the pattern matching method takes around 2.5ms, 10 times longer. During this processing time, the web is still being transferred, causing an un-controllable registration error in the X direction. Thus, the image process time should be as short as possible.

After getting the offset value, there are three ways to print the offset images. The first one is physically moving the printhead which requires fast and precise moving mechanism. The second one is offsetting the nozzles using a program. The third one is loading the images with pre-offset patterns. It turns out that the third method is the most practical one. In this method, we build a bundle of .bmp images with different pre-offset values and name them in a sequence when storing in the hard disk. The images are formed by moving all “black pixels” down by 1 pixel (70.5μm in physical offset) while maintaining the entire image size. We develop a Matlab code that offsets the input image by 1 pixel each time and then outputs a bunch of images stored in the hard drive. By mapping the offset value from edge detection to the image id, the image with correct offset value can be selected out and sent to print server. The mapping algorithm is described below and implemented in Figure 6-7.

The cartridge is 360dpi, which is 70.5μm in spacing, so it needs 6000μm/70.5μm =85 images to cover the entire 6mm FOV range. Pixel output is 0-2047, so the conversion is 2048/85=24 pixels per image. So the image id is the pixel offset divided by

24. It also indicates that the resolution of the camera system is 24 times the printhead resolution. Besides, in the actual situation, we validate an alignment mark only when the entire 2mm square falls into the FOV. Thus, the offset value range is only from 0-1365 (2048×2/3), otherwise part of the alignment mark is outside the FOV. Under such conditions, the acceptable sideways wander of the web is 4mm. The corresponding image ids to offset 0mm (case 1) and 4mm (case 2) are image0 and image57, respectively, as shown also in Figure 6-7.

To realize the mapping function, the relative position of the camera FOV and the printhead should be kept the same. In other words, the image acquisition setup and material ink-jet printing module should be connected. This is realized by a fixing the camera to the printhead holder using a customized connection part, as shown in Figure 6-8. The camera, thus, will slide on the frame together with the printhead. Another advantage is that, as long as the alignment mark falls inside the FOV, the system will always choose the right corresponding pattern file to print, without setting a virtual "reference point" for the alignment mark.

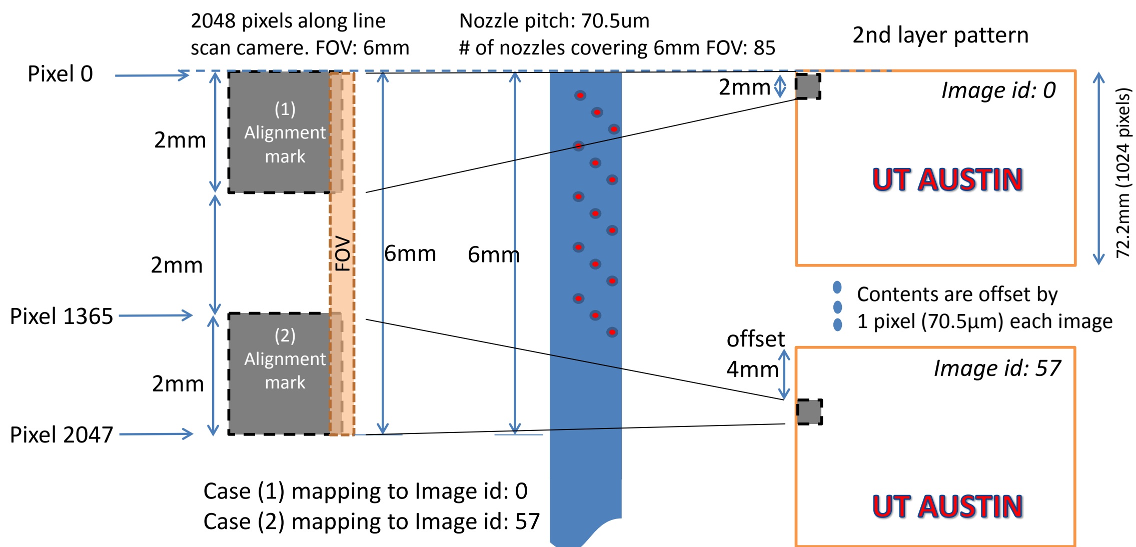

Figure 6-7 mapping offset value in pixel to corresponding image id

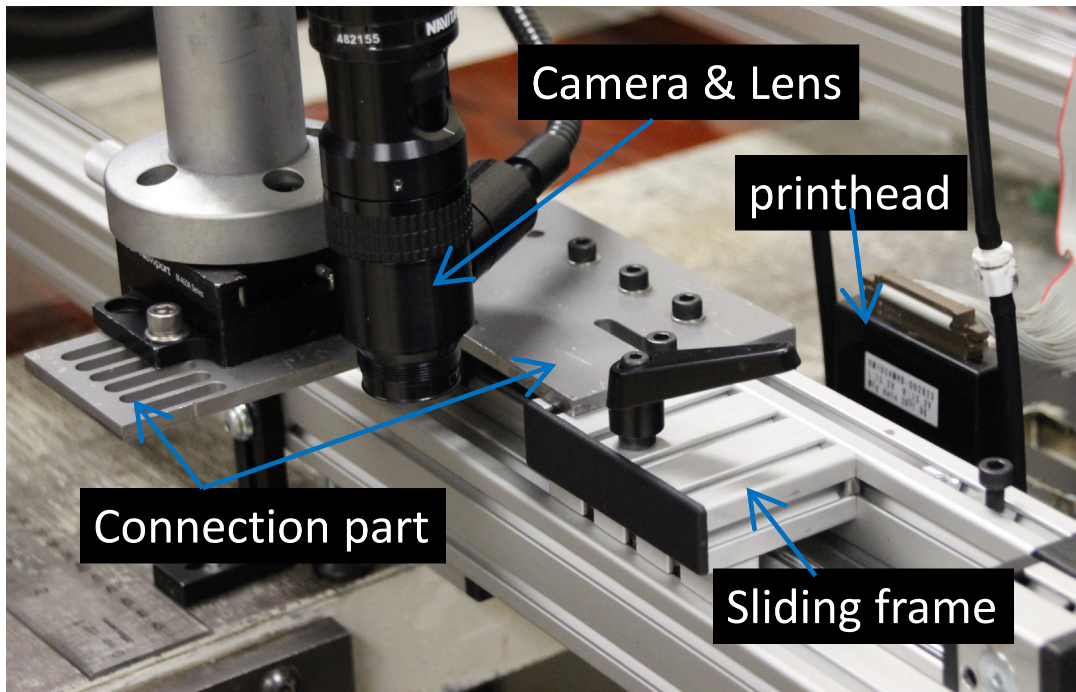

Figure 6-8 the connection part fixes the relative position of camera and printhead

(2) Alignment strategy in X direction (web moving direction)

After choosing the proper pre-offset image to print, we also need to determine what the correct time to start the printing is. That is why we also need the X direction alignment, which is aimed at setting the right timing for the printhead to start printing the patterns. We use a photoelectric sensor with Print/Go mark to determine the printhead actuation moment. For example, as illustrated in Figure 6-9, we need to print 2nd layer pattern (UT AUSTIN with RED color.) on top of the 1st layer image. The following strategies are used:

- The alignment marks and Print/Go marks are put at the ending positions of each copy of the 1st layer pattern. D represents the separation between the front edge of the alignment mark and the Print/Go mark, which, in our test, is set to be 10mm.

- **L_1>S** where L_1 is the 1st layer image length, which is also the separation between adjacent alignment marks and S is the distance between the camera FOV center and the printhead. The condition L_1>S makes sure that the separation between adjacent alignment marks is large enough for previous patterns to finish printing. It avoids the situation that wherein the camera detects the next alignment mark and the printhead has not finished the current copy's 2nd layer printing. In Figure 6-9, it can be seen that when the camera detects alignment mark 2, the entire pattern in the previous copy has passed the printhead meaning the printing should have finished.
- **L_2=S+D+W-B** where L_2 is the 2nd layer image length; W is the width of the Print/Go mark; and B is the distance between the Print/Go mark and the photoelectric sensor, when the alignment mark is detected by the camera. This is also called the buffering distance indicating that after the alignment mark is detected and the print command is sent, the system will have some buffering time (buffering distance B divided by web moving speed) to finish the image loading and transferring before the printhead's actual actuation.

L_2 is the maximum range that multi-layers can be overlapped and it is determined by the separation S and the buffering length B. The separation S, however, is still adjustable by moving the camera close to or away from the printhead. Keep the S value small is to make sure the sideway wander during the S distance transfer is minimized. The B value can be adjusted by the xyz stage holding the photoelectric sensor. Due to our hardware installation, its value is adjustable and close to D. Besides, it should not be too large, otherwise L_2 will be reduced. It should not be too small either otherwise the file loading and transferring process may not be finished before the Print/Go mark is sensed.

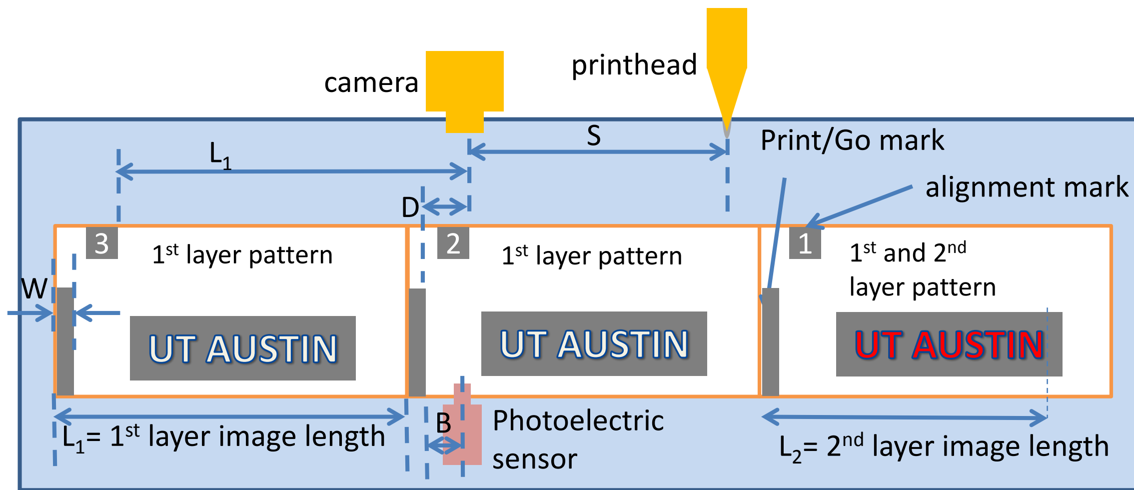

Figure 6-9 alignment strategy in X direction indicating the positioning requirement of the printhead, camera and Print/Go sensor

(3) Multi-layer printing strategy with single stage

Since the roll-to-roll tracker is a one-direction tracker which cannot run the substrate in the opposite direction, it will need 3 running cycles to complete printing two layers, as shown in Figure 6-10. Before the first printing step, shaft A has the material, and shaft B is empty. After printing the first layer, shaft A will have no material, and shaft B would have all the material. Now, the positions of shafts A and B will be interchanged, and the web will run in the forward motion in order to bring back all the material back to shaft A. The positions of shaft A and B will be interchanged again to restore the correct orientation (polarity). Figure 6-10 (a) shows the printing of 1st layer. After rewinding, the polarity of the pattern will be changed as shown in Figure 6-10 (b). Therefore, NO actions will be taken in the 2nd rewinding process. The next layer is printed when the web is running on the 3rd rewinding process with the same polarity as the 1st rewinding process, as shown in Figure 6-10 (c). Although an extra rewinding process is involved, it ensures the alignment using the same edge with less lateral movement. It is the same for the following layers in the sense that an empty run should be

performed to "initialize" the polarity of the pattern. Besides, the pattern is located at the outside surface of the substrate at all times. Note that in the case of continuous R2R printing utilizing multiple printing stages, more layers can be printed within one pass, thus the dummy run times can be reduced.

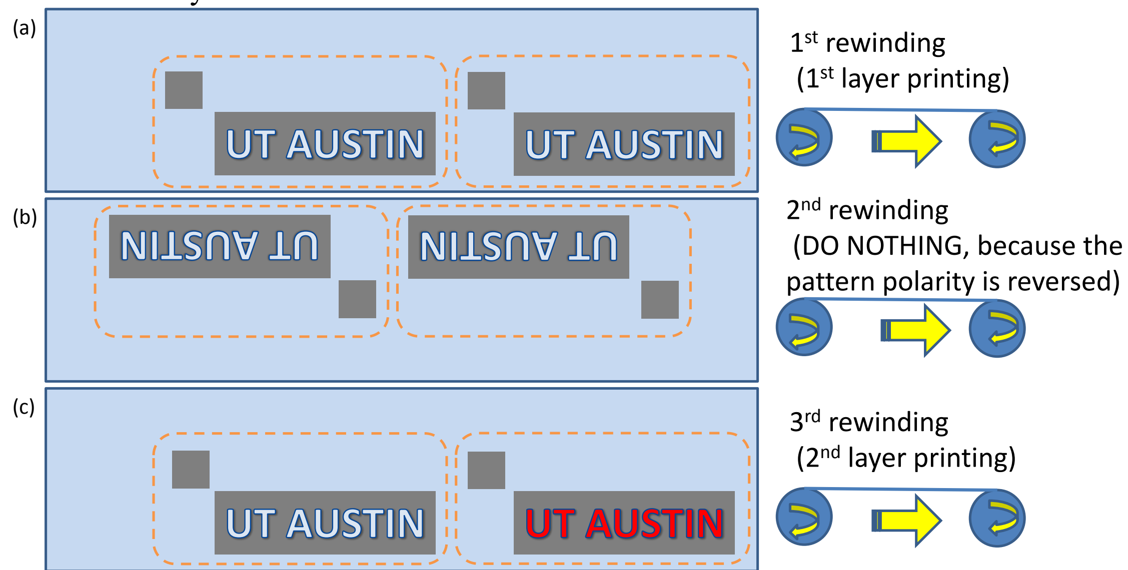

Figure 6-10 multi-layer printing using a single stage. A dummy run is needed to ensure the pattern's polarity.

(4) Software development using NI LabVIEW

We use LabVIEW from NI instrument to integrate all the functional modules needed, from image acquisition to printer control. The LabVIEW code is attached in Appendix B.

The program VI starts by opening up a TCP connection to our print server at 'localhost' (port 2000). It then writes the TCP command *P,Q,P*, which sets up the printer server and puts it in queue mode. At this point, the outer while (main) loop begins and continues to run until we stop the image acquisition process. The algorithm can be described by three sequential modules- image (vision) acquisition, image processing, and printhead control modules. When the data flow enters the main loop, the vision

acquisition module begins executing and continuously captures video in real-time using the Dalsa line-scan camera, and it is set to continuous acquisition with inline processing mode. This module is represented by the *acquireImages()* method in the pseudocode below. After an image is captured, control follows to the image processing module. In this module, the image goes under an edge detection algorithm. Our algorithm is set to detect the first and the last edge only. This module returns the number of edges found and the coordinate point of each edge, and is represented by the *processImages()* method below. The last module is the printhead control module. This module consists of an If-Else-If control structure where we check for certain conditions before sending print commands. The first condition checks to see if we've acquired more than one edge. Two edges represent a signal that an alignment marker has been found. The second condition makes sure that the alignment mark has a width between 500 and 800 pixels. The width is calculated by using the coordinate points located in the image processing module. The last condition checks if our flag variable is 'TRUE' or 'FALSE. False represents that a new alignment marker has not been found. This avoids sending print commands if the edge detected is still the same alignment marker. If these three conditions are met, then we set the flag to 'TRUE', calculate the corresponding image id to the detected offset, and then concatenate all necessary strings to send a TCP/IP command to the printer. If the number of edges is equal to zero, then we reset the flag to 'FALSE'. When there are no more images to process or user presses STOP, control exits the main loop and sends a final TCP/IP command *P,Q,E*, to properly close the connection. Figure 6-11 shows the pseudo code and flow chart of the software developed.

Pseudocode:

```
flag = 0;
initializeTCP();
while (roll-to-roll printer is running)
{
    acquireImages();
    processImages();
    if  (edgesDetected > 1 &&
    detectedWidth > 500 &&
    detectedWidth < 800 &&
    flag==0)
    {  flag = 1;
       calculate  y value;
       calculate x midpoint;
       send TCP/IP command;
    }
     else if (edgesDetected == 0)
    {
     flag = 0;
    }
}
closeTCP();
```

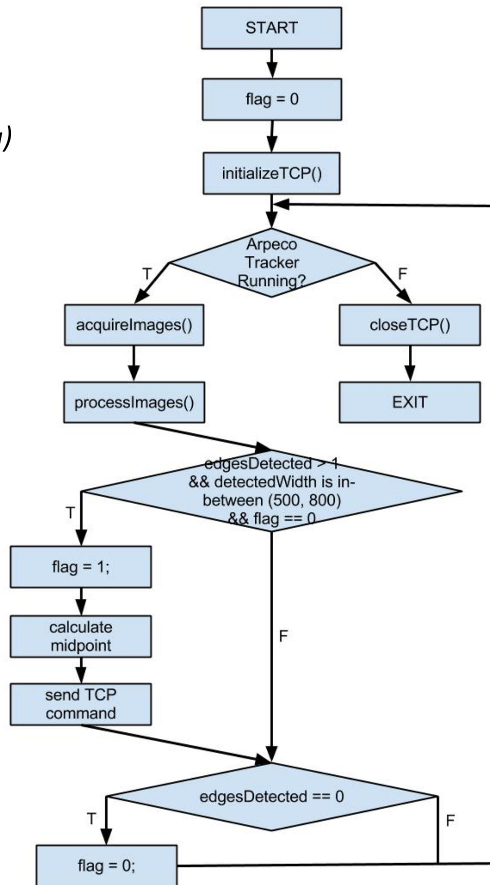

Figure 6-11 pseudo code and flow chart for the controlling software

6.4 Module testing and comprehensive testing

(1) Alignment mark detection

From the algorithm we discussed above, we develop the software using NI LabVIEW. Whenever an alignment mark enters the field of view, it will be captured and the process result is used to select the corresponding pre-offset image and send out the print command immediately. The screenshot of the software while running is shown in Figure 6-12 (a). Figure 6-12 (b) shows an offset testing result with 20 consecutive alignment marks captured by the camera.

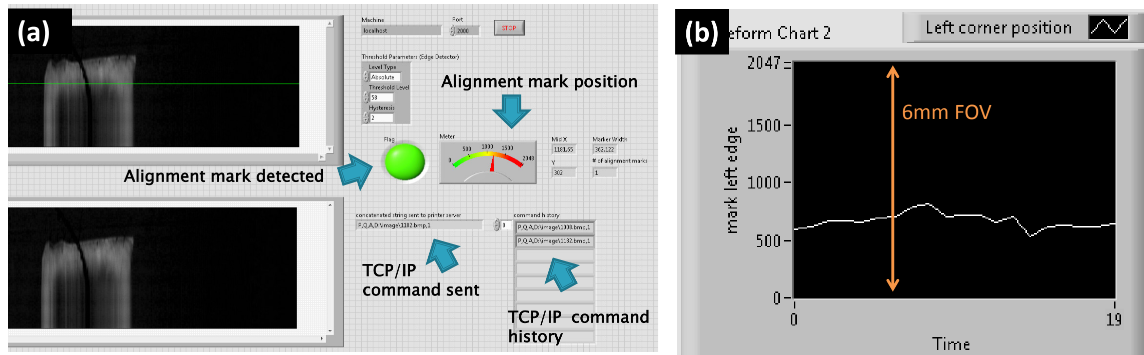

Figure 6-12 (a) screenshot of the software showing position of alignment mark; (2) a sample of 20 consecutive alignment marks position indicating the web sideway wander of around 1.5-2mm for this pass

(2) 1st layer printing and fast curing

A 1st layer testing pattern is printed on Kapton film. Silver ink is used. The Xenon curing module is set to work on continuous exposing mode with a frequency of ~2Hz. Substrate running speed is set at around 5 meters/min so that each pattern will be exposed to 3 pulses when being delivered under the lamp to ensure silver nanoparticles are fully sintered. Figure 6-14 shows the continuous cured patterns on the web.

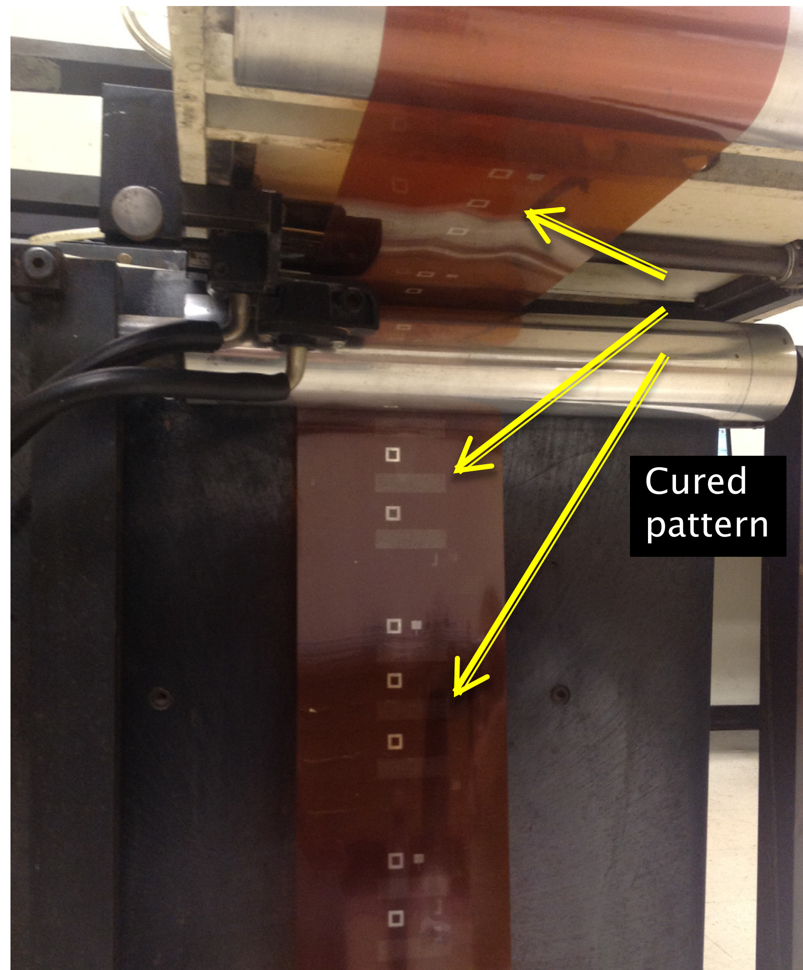

Figure 6-13 continuous pattern are printed and cured in-line.

(3) Registration for multi-layer printing

We performed real-time aligned printing using a testing pattern as shown in Figure 6-14 (a). The 1st layer contains a 2mm×2mm square alignment mark, Print/Go mark and scales in X and Y directions. The 2nd layer is a cross that is centered at X=40mm, Y=10mm location. The result is shown in Figure 6-14 (b) where the cross is printed exactly at the desired location with no obvious off-alignment (< 100μm).

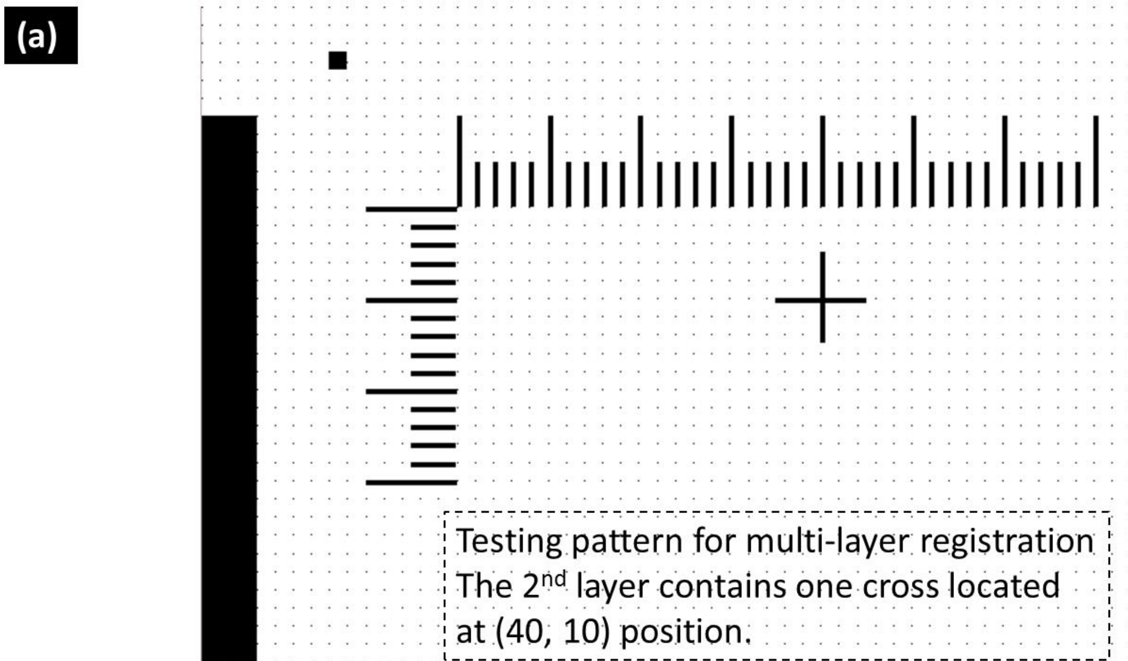

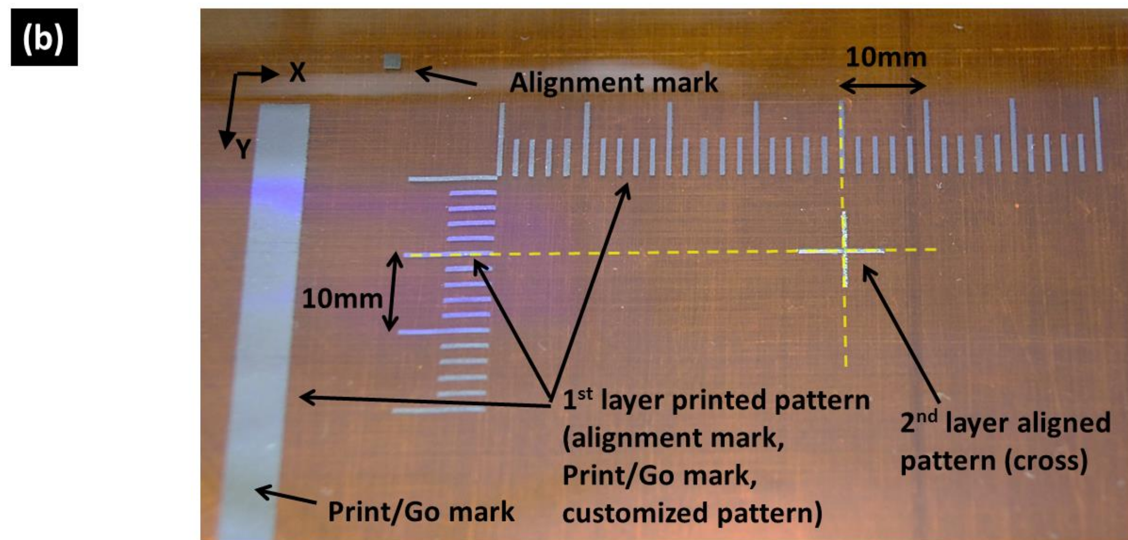

Figure 6-14 (a) test pattern for aligned printing; (b) printed results showing registration of two layers with off-alignment less than 100μm in both X and Y directions.

We also performed continuous printing of 2nd layer to test its repeatability. The results are shown in Figure 6-15. Dashed lines are drawn to help identify the cross

location. As can be seen, for all copies, the off-registration errors are <100μm in X and <200μm in Y directions which indicates the feasibility of our alignment strategies.

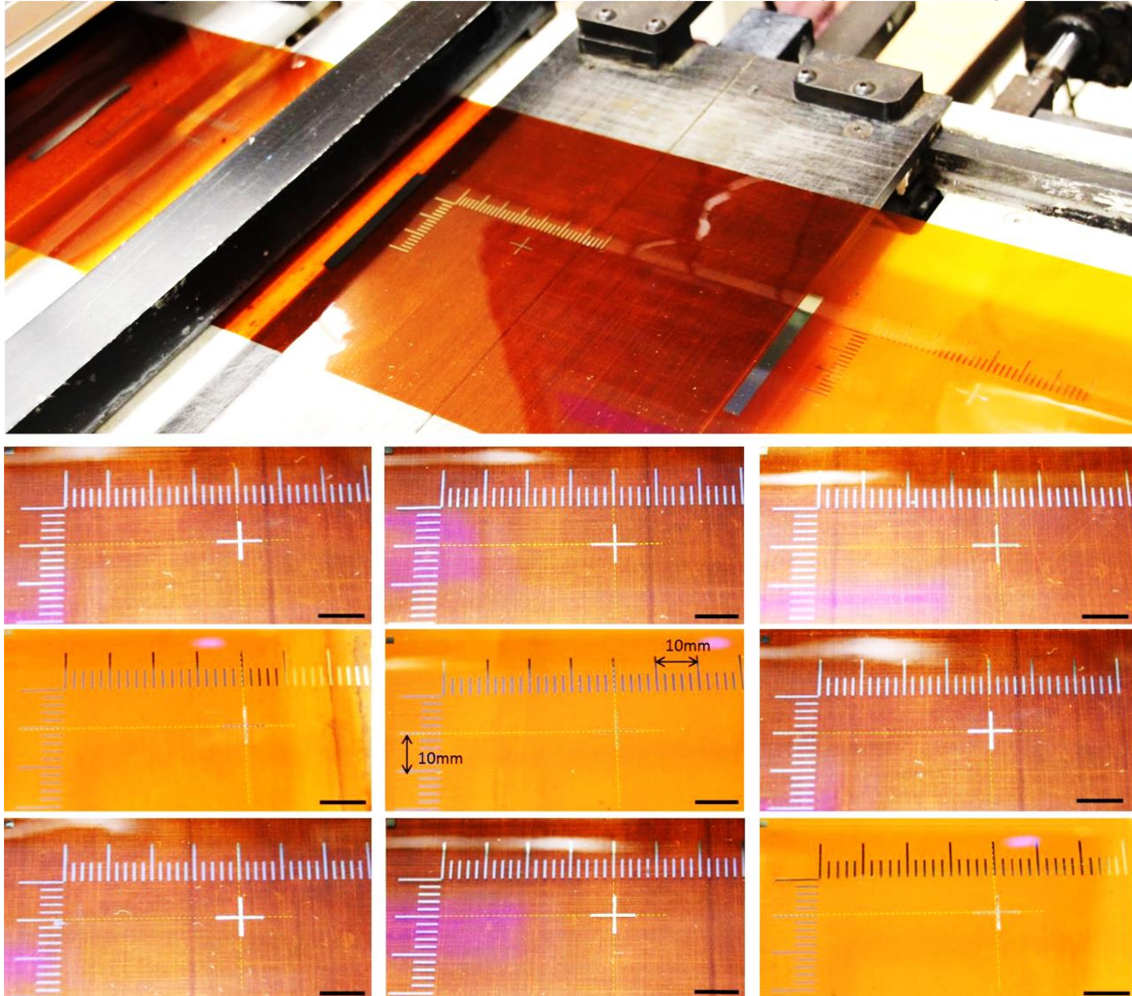

Figure 6-15 continuous printing showing satisfying online registration of 2nd layer patterns with ΔX<100μm and ΔY<200μm for all copies. The scale bar is 10mm (also shown in the central picture).

(4) Performance overview

Although precise and effective algorithms are applied to ensure best registration accuracy, there are still many factors, predictable or un-predictable, that need to be

considered so that their effects to the system performance and auto registration accuracy can be minimized. Below is a list that needs attention:

- The resolution of printhead
- The time required to start the Print Server
- The time between the print command being sent and the Print Server being ready to start printing
- Image acquisition and processing delay
- The number of PMBs or printheads which can be connected to a single PC

It is extremely difficult to precisely predict or guarantee the performance of the software, as there are a number of different factors which contribute to it. These factors include:

- The operating system setup
- The PC hardware
- The other software or operations running on the PC
- The Print Server configuration

To be specific for our system, some limiting factors affecting system overall registration resolution are shown in Table 6-3. In the X direction, the introduction of Print/Go marks gives the system extra buffering time for file loading/transferring and provides the exact timing to start printing. In the testing pattern, the buffering length (B) is set at around 10mm (adjustable) which gives about 120ms buffering time when the web is running at 5m/min. Thus, many issues related to PC performance are eliminated and the alignment errors are controlled well within 100μm. This error is mainly due to the slip of the encoder. In the Y direction, the main limiting factors come from the printer nozzle offset and the web sideways wander. The printer nozzles have a pitch of 70.5μm, which is larger than the camera resolution. Thus offset values will be rounded and

mapped to the nearest integer when choosing the pre-offset images, as shown in Figure 6-7. Besides, once the image is selected, during L_2 length (2nd layer width) printing, the web is still moving with a certain amount of sideways wander and this is the portion that we do not have any control. Thus, from the design point of view, by reducing camera/printhead separation and 2nd layer pattern width would be helpful to minimize the effect of this uncertainty. To ensure high yield, enough tolerance should be given for off-registration when designing the device pattern.

Table 6-3 limiting factors for registration error

X Direction (absolute value)		**Y Direction (absolute vale)**	
Limiting factors	Offset introduced (µm)	Limiting factors	Offset introduced(µm)
Encoder error due to slip when start/stop	100-200	Printer nozzle offset	70.5µm
Printer delay (4ms delay, web running is 5m/min)	333 during 4ms	Sideway wander offset while transferring from FOV to printhead	Up to 2000
Image file transfer delay (uncertain)	Estimated ~500µm (500KB file size) (*)	Camera resolution	3
LabVIEW program image processing time (1ms)	80	Substrate shrinkage/curved	Not studied
Actual tested offset	< 100µm	Actual tested offset	<200µm

(*)Including PMB-PC via USB (250MB/s), thus 500KB needs 2ms Hard disk readout time: for 5400rpm hard drive, 100MB/s thus 500KB needs 5ms Total 7ms delay (~ 500µm)

6.5 TOWARDS BUILDING DUAL-STAGE INK-JET PRINTING SYSTEM

(1) A complete building block for multi-stage configuration

Until now, the components needed for printing one layer, printing a second layer with good alignment accuracy and high-rate curing of material inks, have been integrated. The combination of these three modules will be treated as a complete building block. The complete stage is shown in Figure 6-16, which is a basic building block for extending the system from single stage to multi-stage workstation. It contains a pattern detection module for alignment purpose, a printing module for forming pattern and a fast curing module to curing the printed pattern. It should be noted that the camera is attached to the print head moving frame so that it can be moved together with the print head. This is to ensure that the camera field of view (FOV) maps correctly to certain nozzles of the printhead. When expanding the system to multiple stages, one can simply put such complete modules in series and each module can be fully functional to stack one layer onto a previous layer with good registration accuracy.

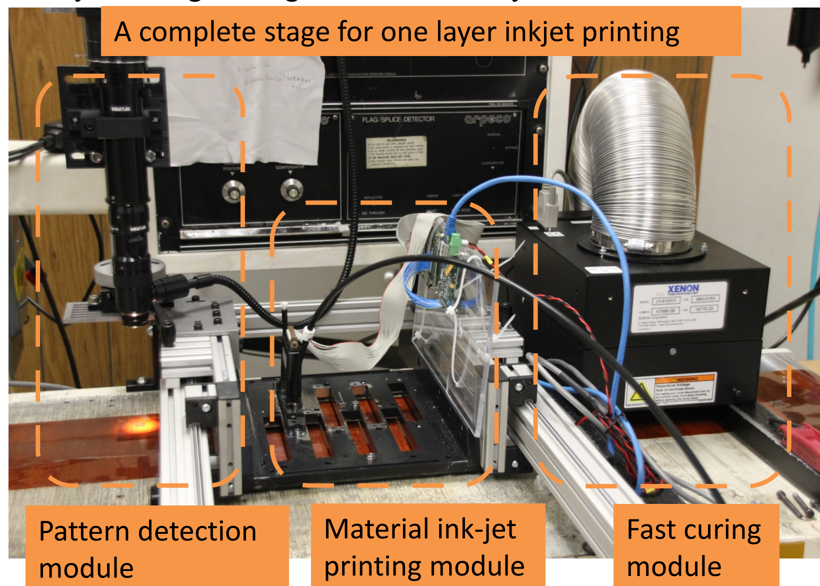

Figure 6-16 a complete stage for one layer ink-jet printing makes a building block for multi-stage system

(2) Dual-stage system working principle

As shown in Figure 6-17, the dual-stage system will include 2 sets of optical systems for alignment purpose and two sets of ink-jet printing components. The two printers share the same encoder signal to control the printing aspect ratio. Besides, the image acquisition card should be able to receive the images from 2 cameras thus it poses higher demand on the acquisition bandwidth. High profile image acquisition board with dual Camera Link inputs should be integrated.

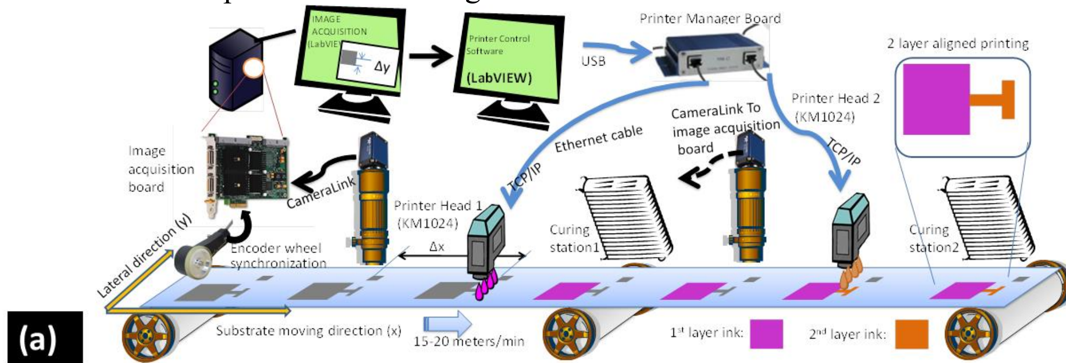

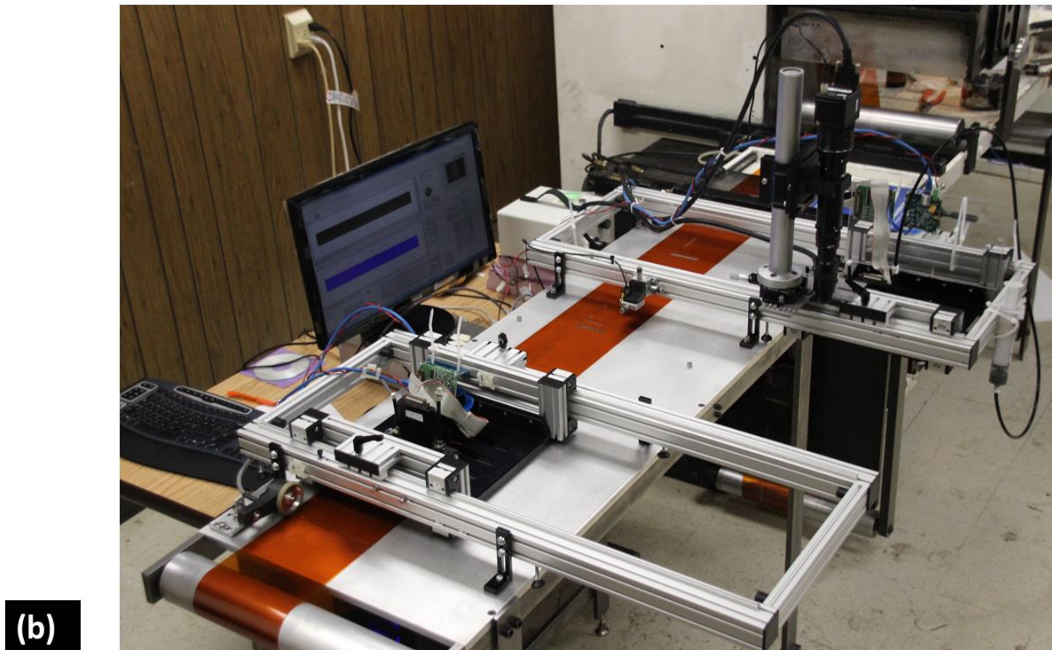

Figure 6-17 (a) schematic of two-stage ink-jet printing process; (b) actual setup showing dual printing stages (without curing station)

6.6 CHAPTER CONCLUSION

In this chapter, we demonstrated a customized, machine vision aided roll-to-roll ink-jet printing system for high rate, high yield device fabrication. Based on the idea of active alignment, we built up all the necessary modules and developed the software to realize auto-registration of multi-layer stacking. The X direction registration is realized by in-line capturing the alignment mark and determining the onset moment of the printing. The Y direction registration is achieved by real time image processing to get the alignment mark offset, and selecting the pre-offset images to compensate for the deviation. Besides, we also discussed in detail the limiting factors that will affect system performance. Finally, a multi-stage system concept is proposed.

Chapter 7: Summary

This dissertation summarizes the research work that has been performed to apply low cost imprinting and ink-jet printing methods in fabricating various optical components.

Waveguide is the most essential part for optical components and imprinting method is utilized to define patterns of the waveguide. We develop an electroplating process to fabricate Ni mold and apply it to transfer pattern of various critical dimensions to polymer cladding layer. Compared to traditional ion-etching method, imprinting method can great reduce the surface damage and provide high optical performance to the final device.

Most functional devices are featured with stacked layer based structure. Therefore, by integrating ink-jet printing method for layer depositing purpose is practical, especially when the layer can be deposited with pre-defined patterns and alignment. Based on this idea, we demonstrated three different optical devices. First one is proximity coupler for board-to-board optical interconnects. Electroplated metal mold is utilized to fabricate multi-mode waveguide with embedded 45° mirrors. The ink-jet printed micro-lenses are put at the output to reduce the divergent angle of the beam. Experiential results show 4dB improvement on insertion loss, when one micro-lens is presented. High speed data transfer up to 10Gbps is performed to prove the signal quality enhancement at various board-to-board separations. The second device demonstrated is a 2×2 channels thermo-optic switch based on total internal reflection. When designing the switch, considerations are taken to make sure its printability. The waveguide is designed to be a rib waveguide and the core layer material SU-8 is evaluated to be ink-jet printable with desired thickness. The fabricated device turns out to have decent performance with less

than 0.5ms switching time when operating at 1 kHz. The third device implemented is Mach-Zehnder based electro-optic polymer modulator. Rib-waveguide is imprinted and the grounding/driving electrode layers are ink-jet printed. When printing the top electrode, precise alignment to underneath M-Z arm is realized and it serves as both poling and driving electrodes. By employing this novel print-on-demand technology, the risk of device failure is reduced since no complicated lift-off process is taken and the core EO polymer is not exposed to any rinsing/etching chemicals. The fabricated device shows satisfying performance with V_π•L=5.68V•cm.

Another important advantage for both imprinting and ink-jet printing techniques is their compatibility with roll-to-roll process, which is a high rate manufacturing concept for flexible devices. In order to extend our current ink-jet printing technology to roll-to-roll process, we demonstrate a complete machine vision aided ink-jet printing machine, from hardware integration to software development, realizing active real time multi-layer auto registration. The key design considerations and each building module are discussed in detail, guided by the alignment algorithm applied. The modules test and comprehensive test are performed and system overall performance are evaluated.

Appendix A: Xenon Fast Curing System

Source: http://www.xenoncorp.com/

One of the key hurdles of using the standard printing process for printed electronics is the deposition of conductive traces on a flexible substrate like paper or plastic. The main reason is that these traces need to have a low resistance value to be efficient. In the case of PCBs these are solid sheets of metal and so typically have very low resistance. In the case of Printed Electronics they need to start in the form of a liquid ink that can be easily deposited on the substrate by the printing process and then converted to a solid uniform layer of conductive material. This requires the ink be sintered to go from its powdered form in the ink to a solid conductive trace. Additionally the liquid carrier medium has to be removed. A conventional sintering process requires heat above 150°C and therefore does not lend itself to printed electronics because of resulting damage to the substrate the ink is deposited on. Metals have a higher melting point than the flexible substrate and so it would seem that it would be impossible to achieve sintering without subsequent damage to the substrate.

From the material point of view, reducing the melting point will be an important change. This is termed melting point depression and is a phenomenon that occurs when the surface area to volume ratio is increased as the particles becomes smaller, as shown in Figure A-1. In metals, the attractive forces of the core of the clusters are too weak to keep the surface atoms from being mobile and so the melting point starts to drop significantly as the particle size is made smaller. However, typically for these conductive inks the time required for sintering down the nanoparticle into a homogenous conductive layer can be in the order of tens of minutes and therefore further improvements are needed before it can be employed in high speed roll-to-roll applications.

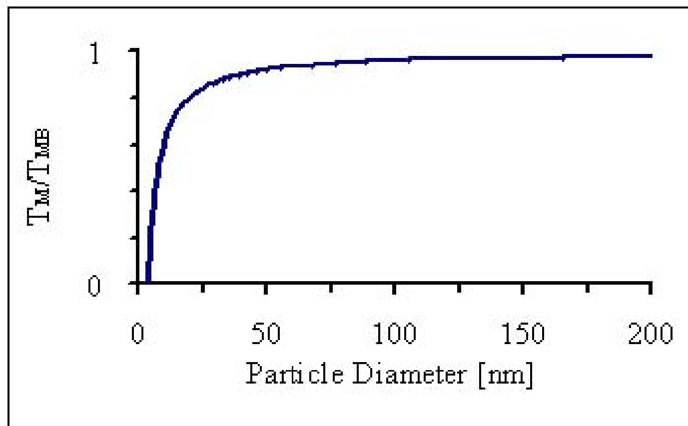

$$T_M(d) = T_{MB}\left(1 - \frac{4\sigma_{sl}}{H_f \rho_s d}\right)$$

T_{MB} = Bulk Melting temperature
σ_{sl} = solid–liquid interface energy
H_f = Bulk heat of fusion
ρ_s = density of solid
d = particle diameter

Figure A-1 a normalized melting curve for gold as a function of nanoparticle diameter. The bulk melting temperature and melting temperature of the particle are denoted TMB and TM respectively. Experimental melting curves for near spherical metal nanoparticles exhibit a similarly shaped curve.

Another important change is the way that these nanoparticles interact with light. For visible light, the wavelength is in the range of 400 to 650 nm. When particle sizes become smaller than the wavelength of light, the electromagnetic field of light can modulate the electrons of the atom. This changes the absorption characteristics of the material. This absorption characteristic is related to particle size. The energy absorbed from light is sufficient to cause increased mobility of the atoms, thus causing sintering.

The combination of melting point depression and absorption characteristics changes mean that ink composed of these nanoparticles can be sintered at a low temperature with light. Once the material has been sintered with light, the nanoparticles form large metallic structures and lose their nanoparticle properties. Using nanotechnology, conductive traces can be deposited and then formed on the substrate in a simple two-step process that is very similar to a standard printing process. One advantage of using high energy pulsed light is that the sintering process can take a fraction of a

second to completely sinter the material, and this process lends itself to practical roll-to-roll application.

Photonic sintering uses light to sinter material. By using high energy flash lamps, high peak power pulses can be generated. They are capable of delivering significantly greater peak energies compared to continuous sources like mercury, fluorescent or halogen lamps by storing energy over time and delivering it as a short duration high intensity pulse.

Xenon arc lamps generate light by using high voltage to breakdown the inert gas within the lamp envelope, creating a conductive discharge path where the flash exists. These lamps are broadband incoherent sources with spectra ranging from the deep UV to the Infrared.

A typical flash lamp use consists of a very short ON time compared to the OFF time, and is very effective at delivering high peak photonic power without significantly increasing the surface temperature of the object being illuminated. Typical ON times can be in the order of a few microseconds to milliseconds with duty cycle ranging from tens of hertz to a few hertz. In these very short durations, peak powers of a few Mega Watts can be generated, as shown in Figure A-2. By adjusting the voltage and the current delivery through the lamp, the pulses can be tailored for specific application delivering repeatable and uniform intensities over a broad spectrum. These are ideal characteristics for sintering applications. High peak power means that there is a greater penetration depth and also sufficient energy for useful work particularly in the case for sintering. By delivering this energy over a short time, the substrate temperature rises minimally in the range of a few degrees.

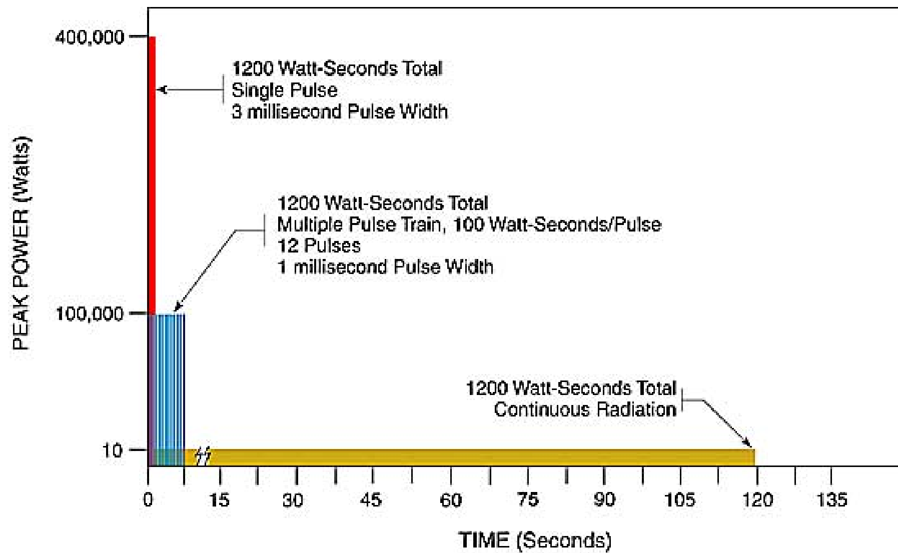

Figure A-2 spectra of Xenon flash lamp and image below shows how high energy can be delivered using short pulses

Xenon Flash Lamps are manufactured with a low pressure xenon gas inside a transparent envelope. There are two electrodes typically made of different materials; the cathode is typically barium doped and designed to have a low work function for the generation of electrons whereas the anode is usually made of tungsten to sustain the bombardment of electrons during a flash. These lamps do have a polarity and improper connection of the lamp can cause lamp damage and early lamp failure. During normal use the electrodes are damaged, metal particles get deposited on the glass and other aging effects take place with the result the intensity falls off. This gradual fall off in intensity defines the lamp life time and is usually reported in millions of pulses at typical use and is approximately the number of pulses for the lamp to remain within 20% of the initial intensity. This value would change based on the energy of the pulse and cooling. If the lamps are driven with lower energy, the lifetime of the lamp can be significantly increased. Lamp cooling is also a very significant component of the optical system and

sets the operational limits of the lamp and affects lamp life. Air cooled lamps use forced air for cooling offers the simplest solution for most applications.

Electronics to drive flash lamps having pulsed output comprises of a high voltage supply, a storage capacitor, a pulse forming inductor and a trigger circuit. Due to the high power requirements of the system, special design requirements need to be met in terms of safety, noise immunity and power management.

Appendix B: LabVIEW Code for Printer Control

The screenshot of LabVIEW VI including block diagram and front panel is provided in Figure B-1 (a) and (b), respectively. The VI can be divided into 3 sections: image acquisition, image processing and printer actuation.

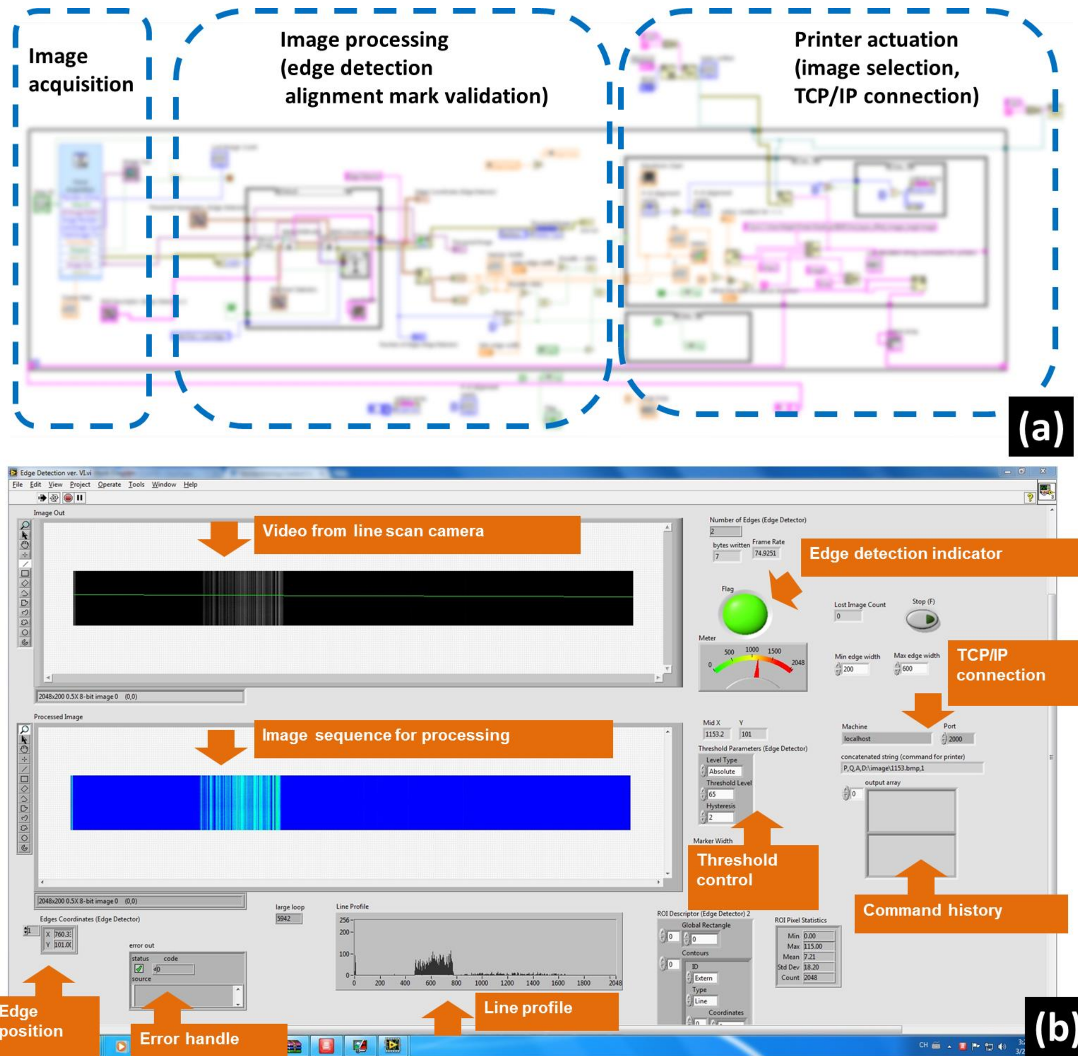

Figure B-1 block diagram (a) and front panel (b) of the LabVIEW VI developed for controlling the ink-jet printing system

Appendix C: Publication List

Journal Publications

1. X. Zhang, A. Hosseini, **X. Lin**, H. Subbaraman, and R. T. Chen, “Polymer-Based Hybrid-Integrated Photonic Devices for Silicon On-Chip Modulation and Board-Level Optical Interconnects,” Selected Topics in Quantum Electronics, IEEE Journal of 19, 3401115-3401115 (2013).

2. **X. Lin**, T. Ling, H. Subbaraman, X. Zhang, K. Byun, L. J. Guo, and R. T. Chen, “Ultraviolet imprinting and aligned ink-jet printing for multilayer patterning of electro-optic polymer modulators,” Opt Lett 38, 1597-1599 (2013).

3. **X. Lin**, T. Ling, H. Subbaraman, L. J. Guo, and R. T. Chen, “Printable thermo-optic polymer switches utilizing imprinting and ink-jet printing,” Opt Express 21, 2110-2117 (2013).

4. **X. Lin**, A. Hosseini, X. Dou, H. Subbaraman, and R. T. Chen, “Low-cost board-to-board optical interconnects using molded polymer waveguide with 45 degree mirrors and inkjet-printed micro-lenses as proximity vertical coupler,” Opt Express 21, 60-69 (2013).

5. **X. H. Lin**, X. Y. Dou, X. L. Wang, and R. T. Chen, “Nickel Electroplating for Nanostructure Mold Fabrication,” J Nanosci Nanotechno 11, 7006-7010 (2011).

6. X. Y. Dou, A. X. Wang, **X. H. Lin**, and R. T. Chen, “Photolithography-free polymer optical waveguide arrays for optical backplane bus,” Opt Express 19, 14403-14410 (2011).

7. X. Y. Dou, X. L. Wang, **X. H. Lin**, D. Ding, D. Z. Pan, and R. T. Chen, “Highly flexible polymeric optical waveguide for out-of-plane optical interconnects,” Opt Express 18, 16227-16233 (2010).

8. X. Y. Dou, X. L. Wang, H. Y. Huang, **X. H. Lin**, D. Ding, D. Z. Pan, and R. T. Chen, “Polymeric waveguides with embedded micromirrors formed by Metallic Hard Mold,” Opt Express 18, 378-385 (2010).

Conference Proceeding Publications

1. H. Subbaraman, **X. Lin**, T. Ling, X. Zhang, L. J. Guo, and R. T. Chen, "Printable EO Polymer Modulators," in CLEO: Science and Innovations, (Optical Society of America, 2013),

2. **X. Lin**, T. Ling, H. Subbaraman, L. J. Guo, and R. T. Chen, "Polymeric Thermo-Optic Switch with Imprinting and Print-on-Demand Technology," in CLEO: Science and Innovations, (Optical Society of America, 2013),

3. **X. Lin**, T. Ling, H. Subbaraman, L. J. Guo, and R. T. Chen, "Towards high-rate fabrication of photonic devices utilizing a combination of roll-to-roll compatible imprint lithography and ink jet printing methods," in SPIE MOEMS-MEMS, (International Society for Optics and Photonics, 2013), 86131H-86131H-86137.

4. **X. Lin**, A. Hosseini, X. Dou, H. Subbaraman, and R. T. Chen, "Polymeric Micro-Lenses Aided Free Space Optical Interconnects," in CLEO: Applications and Technology, (Optical Society of America, 2013),

5. **X. Lin**, A. Hosseini, X. Dou, H. Subbaraman, and R. T. Chen, "Board-to-board optical interconnects utilizing molded embedded 45 degree mirrors and print-on-demand micro-lenses as proximity vertical coupler," in SPIE OPTO, (International Society for Optics and Photonics, 2013), 86300A-86300A-86307.

6. K. Byun, H. Subbaraman, **X. Lin**, X. Xu, and R. T. Chen, "A 3μm channel, ink-jet printed CNT-TFT for phased array antenna applications," in Wireless and Microwave Circuits and Systems (WMCS), 2013 Texas Symposium on, 2013), 1-3.

7. X. Y. Zhang, B. Lee, C. Y. Lin, A. X. Wang, A. Hosseini, **X. H. Lin**, and R. T. Chen, "Improved performance of traveling wave directional coupler modulator based on electro-optic polymer," Optoelectronic Interconnects Xii 8267(2012).

8. H. Subbaraman, **X. H. Lin**, X. C. Xu, A. Dodabalapur, L. J. Guo, and R. T. Chen, "Metrology and instrumentation challenges with high-rate, roll-to-roll manufacturing of flexible electronic systems," Instrumentation, Metrology, and Standards for Nanomanufacturing, Optics, and Semiconductors Vi 8466(2012).

9. **X. H. Lin**, X. Y. Dou, A. X. Wang, and R. T. Chen, “Polymer optical waveguide based bi-directional optical bus architecture for high speed optical backplane,” Optoelectronic Interconnects Xii 8267(2012).

10. **X. Lin**, A. Hosseini, A. X. Wang, and R. T. Chen, “Reduced surface roughness with improved imprinting technique for polymer optical components,” in Photonics Conference (IPC), 2012 IEEE, 2012), 280-281.

11. **X. Lin**, X. Dou, A. Hosseini, A. X. Wang, and R. T. Chen, “Manufacturing of board level waveguide bus using hard mold,” in Optical Interconnects Conference, 2012 IEEE, (IEEE, 2012), 139-140.

12. X. Dou, X. Wang, **X. Lin**, and R. T. Chen, “Manufacturable Polymeric Optical Waveguide based Bus Structures for Board Level Optical Interconnects,” MRS Online Proceedings Library 1438, (2012).

13. **X. H. Lin**, X. Y. Dou, A. X. Wang, and R. T. Chen, “Polymeric Waveguide Array with 45 Degree Slopes Fabricated by Bottom Side Tilted Exposure,” Optoelectronic Interconnects and Component Integration Xi 7944(2011).

14. X. L. Wang, X. Y. Dou, **X. H. Lin**, and R. T. Chen, “Flexible Polymer Optical Layer for Board-Level Optical Interconnects by Highly Durable Metal Imprinting Method,” Optoelectronic Interconnects and Component Integration Ix 7607(2010).

15. X. Y. Dou, X. L. Wang, H. Y. Huang, **X. H. Lin**, and R. T. Chen, “Fabrication of metallic hard mold for polymeric waveguides with embedded micro-mirrors,” 2010 IEEE Photonics Society Winter Topicals Meeting Series, 101-102 (2010).

16. X. Y. Dou, A. X. Wang, **X. H. Lin**, H. Y. Huang, and R. T. Chen, “Optical bus waveguide metallic hard mold fabrication with opposite 45 degrees micro-mirrors,” Optoelectronic Interconnects and Component Integration Ix 7607(2010).

Bibliography

[1] A. K. Kodi, and A. Louri, "Energy-Efficient and Bandwidth-Reconfigurable Photonic Networks for High-Performance Computing (HPC) Systems," IEEE Journal of Selected Topics in Quantum Electronics, 17(2), 384-395 (2011).

[2] D. W. Huang, T. Sze, A. Landin *et al.*, "Optical interconnects: Out of the box forever," IEEE Journal of Selected Topics in Quantum Electronics, 9(2), 614-623 (2003).

[3] G. Q. Chen, H. Chen, M. Haurylau *et al.*, "On-chip copper-based vs. optical interconnects: Delay uncertainty, latency, power, and bandwidth density comparative predictions," Proceedings of the IEEE 2006 International Interconnect Technology Conference, 39-41, 232 (2006).

[4] "www.imec.be/ScientificReport/SR2010/2010/1159106.html."

[5] Y. Enami, C. T. Derose, D. Mathine *et al.*, "Hybrid polymer/sol-gel waveguide modulators with exceptionally large electro-optic coefficients," Nature Photonics, 1(3), 180-185 (2007).

[6] D. T. Chen, H. R. Fetterman, A. T. Chen *et al.*, "Demonstration of 110 GHz electro-optic polymer modulators," Applied Physics Letters, 70(25), 3335-3337 (1997).

[7] T. Baehr-Jones, B. Penkov, J. Q. Huang *et al.*, "Nonlinear polymer-clad silicon slot waveguide modulator with a half wave voltage of 0.25 V," Applied Physics Letters, 92(16), - (2008).

[8] M. B. Christiansen, M. Scholer, and A. Kristensen, "Integration of active and passive polymer optics," Optics Express, 15(7), 3931-3939 (2007).

[9] X. H. Lin, X. Y. Dou, A. X. Wang *et al.*, "Polymer optical waveguide based bi-directional optical bus architecture for high speed optical backplane," Optoelectronic Interconnects Xii, 8267, (2012).

[10] H. Yu, X. Q. Jiang, J. Y. Yang *et al.*, "The design of 2x2 polymer TIR switch based on thermal field analysis employing thermo-optic effect," Passive Components and Fiber-Based Devices, Pts 1 and 2, 5623, 174-183 (2005).

[11] X. L. Wang, B. Howley, M. Y. Chen *et al.*, "4 x 4 nonblocking polymeric thermo-optic switch matrix using the total internal reflection effect," IEEE Journal of Selected Topics in Quantum Electronics, 12(5), 997-1000 (2006).

[12] B. S. Lee, C. Y. Lin, A. X. Wang *et al.*, "Demonstration of a Linearized Traveling Wave Y-Fed Directional Coupler Modulator Based on Electro-Optic Polymer," Journal of Lightwave Technology, 29(13), 1931-1936 (2011).

[13] D. H. Park, Y. Z. Leng, J. D. Luo *et al.*, "High speed electro-optic polymer phase modulator using an in-plane slotline RF waveguide," Rf and Millimeter-Wave Photonics, 7936, (2011).

[14] W. H. Steier, A. Szep, Y. H. Kuo *et al.*, "High speed polymer electro-optic modulators," Leos 2001: 14th Annual Meeting of the IEEE Lasers & Electro-Optics Society, Vols 1 and 2, Proceedings, 188-189 (2001).

[15] W. H. Wong, K. K. Liu, K. S. Chan *et al.*, "Polymer devices for photonic applications," Journal of Crystal Growth, 288(1), 100-104 (2006).

[16] J. Y. Yang, Q. J. Zhou, and R. T. Chen, "Polyimide-waveguide-based thermal optical switch using total-internal-reflection effect," Applied Physics Letters, 81(16), 2947-2949 (2002).

[17] L. J. Guo, "Nanoimprint lithography: Methods and material requirements," Advanced Materials, 19(4), 495-513 (2007).

[18] X. M. Zhao, Y. N. Xia, and G. M. Whitesides, "Soft lithographic methods for nano-fabrication," Journal of Materials Chemistry, 7(7), 1069-1074 (1997).

[19] S. Y. Chou, P. R. Krauss, and P. J. Renstrom, "Imprint lithography with 25-nanometer resolution," Science, 272(5258), 85-87 (1996).

[20] A. K. Das, "Laser direct writing polymeric single-mode waveguide devices with a rib structure," Applied Optics, 42(7), 1236-1243 (2003).

[21] S. C. Minne, P. Flueckiger, H. T. Soh *et al.*, "Atomic-Force Microscope Lithography Using Amorphous-Silicon as a Resist and Advances in Parallel Operation," Journal of Vacuum Science & Technology B, 13(3), 1380-1385 (1995).

[22] R. D. Piner, J. Zhu, F. Xu *et al.*, ""Dip-pen" nanolithography," Science, 283(5402), 661-663 (1999).

[23] S. H. Ahn, and L. J. Guo, "High-speed roll-to-roll nanoimprint lithography on flexible plastic substrates," Advanced Materials, 20(11), 2044-+ (2008).

[24] J. H. Min, H. Kim, B. Kim *et al.*, "Design of Microlens Array on Aperture Stop Array to Generate Multi Optical Probes with Spatial Light Modulation," Japanese Journal of Applied Physics, 47(8), 6800-6803 (2008).

[25] K. L. Lai, S. F. Hsiao, M. H. Hon *et al.*, "Patterning of polystyrene thin films by solvent-assisted imprint lithography and controlled dewetting," Microelectronic Engineering, 94, 33-37 (2012).

[26] Y. L. Gao, J. Lin, P. Jin *et al.*, "Stop grating for perfect replication of micro Fresnel lens by thermal imprinting," Journal of Micromechanics and Microengineering, 22(6), (2012).

[27] S. W. Ahn, K. D. Lee, D. H. Kim *et al.*, "Polymeric wavelength filter based on a Bragg grating using nanoimprint technique," IEEE Photonics Technology Letters, 17(10), 2122-2124 (2005).

[28] Y. J. Weng, Y. C. Weng, Y. C. Wong *et al.*, "Fabrication of Optical Waveguide Devices Using Electromagnetic Assisted Nanoimprinting," Proceedings of the 2009 International Conference on Signal Processing Systems, 910-912 (2009).

[29] X. L. Wang, X. Y. Dou, X. H. Lin *et al.*, "Flexible Polymer Optical Layer for Board-Level Optical Interconnects by Highly Durable Metal Imprinting Method," Optoelectronic Interconnects and Component Integration Ix, 7607, (2010).

[30] M. Wang, J. Hiltunen, S. Uusitalo *et al.*, "Fabrication of optical inverted-rib waveguides using UV-imprinting," Microelectronic Engineering, 88(2), 175-178 (2011).

[31] X. Lin, X. Dou, X. Wang *et al.*, "Nickel electroplating for nanostructure mold fabrication," J Nanosci Nanotechnol, 11(8), 7006-10 (2011).

[32] X. Y. Dou, X. L. Wang, H. Y. Huang *et al.*, "Fabrication of metallic hard mold for polymeric waveguides with embedded micro-mirrors," 2010 IEEE Photonics Society Winter Topicals Meeting Series, 101-102 (2010).

[33] T. Ling, S. L. Chen, and L. J. Guo, "Fabrication and characterization of high Q polymer micro-ring resonator and its application as a sensitive ultrasonic detector," Optics Express, 19(2), 861-869 (2011).

[34] C. Y. Chao, and L. J. Guo, "Polymer microring resonators fabricated by nanoimprint technique," Journal of Vacuum Science & Technology B, 20(6), 2862-2866 (2002).

[35] D. Pisignano, L. Persano, E. Mele *et al.*, "First-order imprinted organic distributed feedback lasers," Synthetic Metals, 153(1-3), 237-240 (2005).

[36] P. C. Kao, S. Y. Chu, T. Y. Chen *et al.*, "Fabrication of large-scaled organic light emitting devices on the flexible substrates using low-pressure imprinting lithography," IEEE Transactions on Electron Devices, 52(8), 1722-1726 (2005).

[37] Y. Ekinci, H. H. Solak, C. David *et al.*, "Bilayer Al wire-grids as broadband and high-performance polarizers," Optics Express, 14(6), 2323-2334 (2006).

[38] M. Jung, J. Kim, J. Noh *et al.*, "All-Printed and Roll-to-Roll-Printable 13.56-MHz-Operated 1-bit RF Tag on Plastic Foils," IEEE Transactions on Electron Devices, 57(3), 571-580 (2010).

[39] J. Noh, D. Yeom, C. Lim *et al.*, "Scalability of Roll-to-Roll Gravure-Printed Electrodes on Plastic Foils," IEEE Transactions on Electronics Packaging Manufacturing, 33(4), 275-283 (2010).

[40] Y. Noguchi, T. Sekitani, and T. Someya, "Organic-transistor-based flexible pressure sensors using ink-jet-printed electrodes and gate dielectric layers," Applied Physics Letters, 89(25), (2006).

[41] J. Jacobson, B. Comiskey, and J. Albert, [Microencapsulated electrophoretic display] Google Patents, (1999).

[42] C. A. Kim, H. J. Myoung, S. Y. Kang *et al.*, "Towards a Colored Electronic Paper through a Fabrication of Color Microencapsulated Electrophoretic Display Panel," Imid/Idmc 2006: The 6th International Meeting on Information Display/the 5th International Display Manufacturing Conference, Digest of Technical Papers, 1415-1418 (2006).

[43] E. Bundgaard, and F. C. Krebs, "Low band gap polymers for organic photovoltaics," Solar Energy Materials and Solar Cells, 91(11), 954-985 (2007).

[44] M. Jorgensen, K. Norrman, and F. C. Krebs, "Stability/degradation of polymer solar cells," Solar Energy Materials and Solar Cells, 92(7), 686-714 (2008).

[45] H. Subbaraman, D. T. Pham, X. C. Xu *et al.*, "Inkjet-Printed Two-Dimensional Phased-Array Antenna on a Flexible Substrate," IEEE Antennas and Wireless Propagation Letters, 12, 170-173 (2013).

[46] E. Gracia-Espino, G. Sala, F. Pino *et al.*, "Electrical Transport and Field-Effect Transistors Using Inkjet-Printed SWCNT Films Having Different Functional Side Groups," Acs Nano, 4(6), 3318-3324 (2010).

[47] M. A. Green, K. Emery, Y. Hishikawa *et al.*, "Solar Cell Efficiency Tables (Version 34)," Progress in Photovoltaics, 17(5), 320-326 (2009).

[48] D. W. Laird, S. Vaidya, S. Li *et al.*, "Advances in Plexcore (TM) active layer technology systems for organic photovoltaics: Roof-top and accelerated lifetime analysis of high performance organic photovoltaic cells - art. no. 66560X," Organic Photovoltaics Viii, 6656, X6560-X6560 (2007).

[49] B. J. de Gans, P. C. Duineveld, and U. S. Schubert, "Inkjet printing of polymers: State of the art and future developments," Advanced Materials, 16(3), 203-213 (2004).

[50] Y. Mikami, Y. Nagae, Y. Mori *et al.*, "A New Patterning Process Concept for Large-Area Transistor-Circuit Fabrication without Using an Optical Mask Aligner," IEEE Transactions on Electron Devices, 41(3), 306-314 (1994).

[51] D. T. Pham, H. Subbaraman, M. Y. Chen *et al.*, "Light Weight and Conformal 2-Bit, 1 x 4 Phased-Array Antenna With CNT-TFT-Based Phase Shifter on a Flexible Substrate," IEEE Transactions on Antennas and Propagation, 59(12), 4553-4558 (2011).

[52] S. H. Ahn, and L. J. Guo, "Large-Area Roll-to-Roll and Roll-to-Plate Nanoimprint Lithography: A Step toward High-Throughput Application of Continuous Nanoimprinting," Acs Nano, 3(8), 2304-2310 (2009).

[53] S. L. Peterson, A. McDonald, P. L. Gourley *et al.*, "Poly (dimethylsiloxane) thin films as biocompatible coatings for microfluidic devices: cell culture and flow studies with glial cells," Journal of Biomedical Materials Research Part A, 72(1), 10-18 (2005).

[54] M. N. De Silva, R. Desai, and D. J. Odde, "Micro-patterning of animal cells on PDMS substrates in the presence of serum without use of adhesion inhibitors," Biomedical Microdevices, 6(3), 219-222 (2004).

[55] K. M. Choi, and J. A. Rogers, "A photocurable poly(dimethylsiloxane) chemistry designed for soft lithographic molding and printing in the nanometer regime," Journal of the American Chemical Society, 125(14), 4060-4061 (2003).

[56] D. Qin, Y. N. Xia, and G. M. Whitesides, "Soft lithography for micro- and nanoscale patterning," Nature Protocols, 5(3), 491-502 (2010).

[57] T. W. Odom, J. C. Love, D. B. Wolfe *et al.*, "Improved pattern transfer in soft lithography using composite stamps," Langmuir, 18(13), 5314-5320 (2002).

[58] S. Sasaki, T. Hiraka, J. Mizuochi *et al.*, "UV NIL template making and imprint evaluation," Alternative Lithographic Technologies, 7271, (2009).

[59] C. K. Chung, K. L. Sher, Y. J. Syu *et al.*, "Fabrication of cone-like microstructure using UV LIGA-like for light guide plate application," Microsystem Technologies-Micro-and Nanosystems-Information Storage and Processing Systems, 16(8-9), 1619-1624 (2010).

[60] S. C. Shen, C. J. Lee, M. W. Wang *et al.*, "Fabrication Micro-Nozzle Plates for Inkjet Print Head Using LIGA Process," Advanced Manufacture: Focusing on New and Emerging Technologies, 594, 132-137, 511 (2008).

[61] L. Gu, Z. Z. Wu, F. Wang *et al.*, "UV-LIGA metal MEMS: A promising tool to serve IC industry," 2008 9th International Conference on Solid-State and Integrated-Circuit Technology, Vols 1-4, 2349-2352, 2592 (2008).

[62] J. Jahns, T. Seiler, J. Mohr *et al.*, "Micro-retroreflector array fabricated by the LIGA process," Micro-Optics 2010, 7716, 734 (2010).

[63] L. Brusberg, M. Neitz, and H. Schroder, "Single-mode glass waveguide technology for optical inter-chip communication on board-level," Optoelectronic Interconnects Xii, 8267, (2012).

[64] J. Xue, A. Garg, B. Ciftcioglu *et al.*, "An Intra-Chip Free-Space Optical Interconnect," Isca 2010: The 37th Annual International Symposium on Computer Architecture, 94-105 (2010).

[65] R. T. Chen, L. Lin, C. Choi *et al.*, "Fully embedded board-level guided-wave optoelectronic interconnects," Proceedings of the IEEE, 88(6), 780-793 (2000).

[66] C. C. Choi, L. Lin, Y. J. Liu *et al.*, "Flexible optical waveguide film fabrications and optoelectronic devices integration for fully embedded board-level optical interconnects," Journal of Lightwave Technology, 22(9), 2168-2176 (2004).

[67] H. P. Kuo, P. Rosenberg, R. Walmsley *et al.*, "Free-space optical links for board-to-board interconnects," Applied Physics a-Materials Science & Processing, 95(4), 955-965 (2009).

[68] K. Nakama, Y. Matsuzawa, Y. Tokiwa *et al.*, "Board-to-Board Optical Plug-In Interconnection Using Optical Waveguide Plug and Micro Hole Array," IEEE Photonics Technology Letters, 23(24), 1881-1883 (2011).

[69] J. J. Yang, A. S. Flores, and M. R. Wang, "Array waveguide evanescent ribbon coupler for card-to-backplane optical interconnects," Optics Letters, 32(1), 14-16 (2007).

[70] A. Flores, S. Y. Song, J. J. Yang *et al.*, "High-Speed Optical Interconnect Coupler Based on Soft Lithography Ribbons," Journal of Lightwave Technology, 26(13-16), 1956-1963 (2008).

[71] P. Pepeljugoski, and D. Kuchta, "Jitter Performance of Short Length Optical Interconnects for Rack-to-Rack Applications," Ofc: 2009 Conference on Optical Fiber Communication, Vols 1-5, 1797-1799 (2009).

[72] J. Sakai, A. Noda, M. Yamagishi *et al.*, "20Gbps/ch Optical Interconnection between SERDES Devices over Distances from Chip-to-Chip to Rack-to-Rack," 2008 34th European Conference on Optical Communication (Ecoc), (2008).

[73] J. W. Goodman, F. J. Leonberger, S. Y. Kung *et al.*, "Optical Interconnections for Vlsi Systems," Proceedings of the IEEE, 72(7), 850-866 (1984).

[74] D. A. B. Miller, "Optical interconnects to silicon," IEEE Journal of Selected Topics in Quantum Electronics, 6(6), 1312-1317 (2000).

[75] Y. Li, T. Wang, and R. A. Linke, "VCSEL-array-based angle-multiplexed optoelectronic crossbar interconnects," Applied Optics, 35(8), 1282-1295 (1996).

[76] D. V. Plant, B. Robertson, H. S. Hinton *et al.*, "4x4 vertical-cavity surface-emitting laser (VCSEL) and metal-semiconductor-metal (MSM) optical backplane demonstrator system," Applied Optics, 35(32), 6365-6368 (1996).

[77] E. M. Strzelecka, D. A. Louderback, B. J. Thibeault *et al.*, "Parallel free-space optical interconnect based on arrays of vertical-cavity lasers and detectors with monolithic microlenses," Applied Optics, 37(14), 2811-2821 (1998).

[78] E. M. Strzelecka, G. D. Robinson, L. A. Coldren *et al.*, "Fabrication of refractive microlenses in semiconductors by mask shape transfer in reactive ion etching," Microelectronic Engineering, 35(1-4), 385-388 (1997).

[79] J. Chou, K. Yu, D. Horsley *et al.*, "Characterization of a MEMS Based Optical System for Free-Space Board-to-Board Optical Interconnects," 2010 Conference on Optical Fiber Communication Ofc Collocated National Fiber Optic Engineers Conference Ofc-Nfoec, (2010).

[80] J. Chou, K. Yu, D. Horsley *et al.*, "Robust free space board-to-board optical interconnect with closed loop MEMS tracking," Applied Physics a-Materials Science & Processing, 95(4), 973-982 (2009).

[81] T. Sakano, T. Matsumoto, and K. Noguchi, "3-Dimensional Board-to-Board Free-Space Optical Interconnects and Their Application to the Prototype Multiprocessor System - Cosine-Iii," Applied Optics, 34(11), 1815-1822 (1995).

[82] F. Y. Wu, V. J. Logeeswaran, M. S. Islam *et al.*, "Integrated receiver architectures for board-to-board free-space optical interconnects," Applied Physics a-Materials Science & Processing, 95(4), 1079-1088 (2009).

[83] C. J. Henderson, B. Robertson, D. G. Leyva *et al.*, "Control of a free-space adaptive optical interconnect using a liquid-crystal spatial light modulator for beam steering," Optical Engineering, 44(7), (2005).

[84] J. H. Choi, L. Wang, H. Bi *et al.*, "Effects of thermal-via structures on thin-film VCSELs for fully embedded board-level optical interconnection system," IEEE Journal of Selected Topics in Quantum Electronics, 12(5), 1060-1065 (2006).

[85] Y. J. Liu, L. Lin, C. Choi *et al.*, "Optoelectronic integration of polymer waveguide array and metal-semiconductor-metal photodetector through micromirror couplers," IEEE Photonics Technology Letters, 13(4), 355-357 (2001).

[86] L. Wang, X. L. Wang, W. Jiang *et al.*, "45 degrees polymer-based total internal reflection coupling mirrors for fully embedded intraboard guided wave optical interconnects," Applied Physics Letters, 87(14), (2005).

[87] C. T. Chen, H. L. Hsiao, C. C. Chang *et al.*, "4 channels x 10-Gbps optoelectronic transceiver based on silicon optical bench technology," Optoelectronic Interconnects Xii, 8267, (2012).

[88] B. Van Hoe, E. Bosman, J. Missinne *et al.*, "Novel coupling and packaging approaches for optical interconnects," Optoelectronic Interconnects Xii, 8267, (2012).

[89] G. M. Jiang, S. Baig, and M. R. Wang, "Soft Lithography Fabricated Polymer Waveguides with 45 degrees Inclined Mirrors for Card-to-Backplane Optical Interconnects," Optoelectronic Interconnects Xii, 8267, (2012).

[90] J. Inoue, T. Ogura, K. Kintaka *et al.*, "Fabrication of Embedded 45-Degree Micromirror Using Liquid-Immersion Exposure for Single-Mode Optical Waveguides," Journal of Lightwave Technology, 30(11), 1563-1568 (2012).

[91] A. L. Glebov, M. G. Lee, and K. Yokouchi, "Integration technologies for pluggable backplane optical interconnect systems," Optical Engineering, 46(1), (2007).

[92] X. L. Wang, W. Jiang, L. Wang *et al.*, "Fully embedded board-level optical interconnects from waveguide fabrication to device integration," Journal of Lightwave Technology, 26(1-4), 243-250 (2008).

[93] X. Y. Dou, X. L. Wang, H. Y. Huang *et al.*, "Polymeric waveguides with embedded micromirrors formed by Metallic Hard Mold," Optics Express, 18(1), 378-385 (2010).

[94] B. Ciftcioglu, R. Berman, S. Wang *et al.*, "3-D integrated heterogeneous intra-chip free-space optical interconnect," Optics Express, 20(4), 4331-4345 (2012).

[95] C. H. Tien, C. H. Hung, and T. H. Yu, "Microlens Arrays by Direct-Writing Inkjet Print for LCD Backlighting Applications," Journal of Display Technology, 5(4-6), 147-151 (2009).

[96] J. Y. Kim, N. B. Brauer, V. Fakhfouri *et al.*, "Hybrid polymer microlens arrays with high numerical apertures fabricated using simple ink-jet printing technique," Optical Materials Express, 1(2), 259-269 (2011).

[97] V. Fakhfouri, N. Cantale, G. Mermoud *et al.*, "Inkjet printing of SU-8 for polymer-based MEMS a case study for microlenses," Mems 2008: 21st IEEE International Conference on Micro Electro Mechanical Systems, Technical Digest, 407-410 (2008).

[98] J. P. Lu, W. K. Huang, and F. C. Chen, "Self-positioning microlens arrays prepared using ink-jet printing," Optical Engineering, 48(7), (2009).

[99] I. A. Grimaldi, A. D. Del Mauro, F. Loffredo *et al.*, "Microlens array manufactured by inkjet printing: study of the effects of the solvent and the polymer concentration on the microstructure shape," Optical Measurement Systems for Industrial Inspection Vii, 8082, (2011).

[100] A. Voigt, U. Ostrzinski, K. Pfeiffer *et al.*, "New inks for the direct drop-on-demand fabrication of polymer lenses," Microelectronic Engineering, 88(8), 2174-2179 (2011).

[101] K. H. Jeong, and L. P. Lee, "A new method of increasing numerical aperture of microlens for biophotonic MEMS," 2nd Annual International IEEE-Embs Special

Topic Conference on Microtechnologies in Medicine & Biology, Proceedings, 380-383 (2002).

[102] F. Morichetti, A. Melloni, C. Ferrari *et al.*, "Error-free continuously-tunable delay at 10 Gbit/s in a reconfigurable on-chip delay-line," Optics Express, 16(12), 8395-8405 (2008).

[103] H. C. H. Mulvad, L. K. Oxenlowe, M. Galili *et al.*, "1.28 Tbit/s single-polarisation serial OOK optical data generation and demultiplexing," Electronics Letters, 45(5), 280-U60 (2009).

[104] Y.-T. Han, J.-U. Shin, S.-H. Park *et al.*, "N × N polymer matrix switches using thermo-optic total-internal-reflection switch," Opt. Express, 20(12), 13284-13295 (2012).

[105] Y. O. Noh, H. J. Lee, Y. H. Won *et al.*, "Polymer waveguide thermo-optic switches with - 70 dB optical crosstalk," Optics Communications, 258(1), 18-22 (2006).

[106] X. L. Wang, B. Howley, M. Y. Chen *et al.*, "Polymer based thermo-optic switch for optical true time delay," Integrated Optics: Devices, Materials, and Technologies IX, 5728, 60-67 (2005).

[107] M. G. Kang, and L. J. Guo, "Metal transfer assisted nanolithography on rigid and flexible substrates," Journal of Vacuum Science & Technology B, 26(6), 2421-2425 (2008).

[108] X. Y. Zhang, B. Lee, C. Y. Lin *et al.*, "Improved performance of traveling wave directional coupler modulator based on electro-optic polymer," Optoelectronic Interconnects Xii, 8267, (2012).

[109] E. L. Wooten, K. M. Kissa, A. Yi-Yan *et al.*, "A review of lithium niobate modulators for fiber-optic communications systems," IEEE Journal of Selected Topics in Quantum Electronics, 6(1), 69-82 (2000).

[110] S. Rao, G. Coppola, M. A. Gioffre *et al.*, "A 2.5 ns switching time MachZehnder modulator in as-deposited a-Si:H," Optics Express, 20(9), 9351-9356 (2012).

[111] H. Chen, B. Chen, D. Huang *et al.*, "Broadband electro-optic polymer modulators with high electro-optic activity and low poling induced optical loss," Applied Physics Letters, 93(4), 043507-043507 (2008).

[112] X. L. Wang, C. Y. Lin, S. Chakravarty *et al.*, "Effective in-device r(33) of 735 pm/V on electro-optic polymer infiltrated silicon photonic crystal slot waveguides," Optics Letters, 36(6), 882-884 (2011).

[113] X. Y. Zhang, B. Lee, C. Y. Lin *et al.*, "Highly Linear Broadband Optical Modulator Based on Electro-Optic Polymer," IEEE Photonics Journal, 4(6), 2214-2228 (2012).

[114] D. Y. Huang, D. L. Jin, B. Q. Chen *et al.*, "Highly efficient EO polymers for low V(pi) modulators," Linear and Nonlinear Optics of Organic Materials Viii, 7049, (2008).

[115] G. T. Paloczi, Y. Huang, A. Yariv *et al.*, "Replica-molded electro-optic polymer Mach–Zehnder modulator," Applied Physics Letters, 85(10), 1662-1664 (2004).

[116] F. C. Krebs, T. Tromholt, and M. Jorgensen, "Upscaling of polymer solar cell fabrication using full roll-to-roll processing," Nanoscale, 2(6), 873-886 (2010).

Vita

Xiaohui Lin was born in Fuzhou, Fujian, China and received his B.S. and Ph.D. degrees in mechanical engineering from the Huazhong University of Science and Technology, Wuhan, China, in 2004 and 2008, respectively. After 1.5 year study in Georgia Institute of Technology, Atlanta, Georgia, he started another graduate program in the University of Texas at Austin, Austin, Texas towards a Ph.D. degree in Electrical and computer engineering in 2009. He joined the optical interconnect research group led by Dr. Ray T. Chen in the same year. His research interests include MEMS device development and polymer based nanophotonic devices for optical interconnects.

Permanent email address: lxhoney@gmail.com

This dissertation was typed by Xiaohui Lin.